

Search for Neutral Higgs Bosons Decaying to Pairs of τ Leptons at $\sqrt{s} = 7$ TeV

By

EVAN KLOSE FRIIS

B.S. (University of California at San Diego) 2005

DISSERTATION

Submitted in partial satisfaction of the requirements for the degree of

DOCTOR OF PHILOSOPHY

in

Physics

in the

OFFICE OF GRADUATE STUDIES

of the

UNIVERSITY OF CALIFORNIA

DAVIS

Approved:

Professor John Conway (Chair)

Professor Robin Erbacher

Professor Mani Tripathi

Committee in Charge

2011

³ Abstract

⁴ blah blah blah

5 Acknowledgments

6 Hooray for everybody.

Table of Contents

8	1 The Standard Model and Beyond	1
9	1.1 The Standard Model	1
10	1.1.1 Quantum Electrodynamics and Gauge Invariance	2
11	1.1.2 The Weak Interactions	4
12	1.1.3 Spontaneous Symmetry Breaking	6
13	1.1.4 The Higgs Mechanism	8
14	1.1.5 Electroweak Unification	10
15	1.1.6 Quantum Chromodynamics	14
16	1.2 Beyond the Standard Model	16
17	1.2.1 The Hierarchy Problem	17
18	1.2.2 Supersymmetry	18
19	1.2.3 The Minimal Supersymmetric Model	18
20	1.3 Searches for the Higgs boson	21
21	1.3.1 Standard Model Higgs boson phenomenology	21
22	1.3.2 MSSM Higgs Phenomenology	24
23	1.3.3 Results from LEP and Tevatron	25
24	1.4 The Physics of the Tau Lepton	30
25	2 The Compact Muon Solenoid Experiment	32
26	2.1 The Large Hadron Collider	33
27	2.2 Solenoid Magnet	35
28	2.3 Charged Particle Tracking Systems	36
29	2.4 Electromagnetic Calorimeter	38
30	2.5 Hadronic Calorimeter	40
31	2.6 Muon System	42
32	2.7 Trigger System	44
33	2.8 Particle Flow Reconstruction Algorithm	46
34	2.9 DAQ	46
35	3 Tau Identification: The Tau Neural Classifier	47
36	3.1 Geometric Tau Identification Algorithms	48
37	3.2 Decay Mode Tau Identification: Motivation	48
38	3.3 The Tau Neural Classifier	49
39	3.3.1 Decay mode reconstruction	50
40	3.3.2 Neural network classification	53
41	3.4 Summary	67
42	3.5 HPS+TaNC: A Hybrid Algorithm	71
43	3.5.1 Decay mode reconstruction	71
44	3.5.2 Hadronic tau discrimination	73

45	3.6 Electron and Muon Rejection	74
46	4 Mass Reconstruction: The Secondary Vertex Fit	76
47	4.1 Existing mass reconstruction algorithms	76
48	4.2 The Secondary Vertex fit	78
49	4.3 Parametrization of tau decays	79
50	4.4 Likelihood for tau decay	80
51	4.4.1 Likelihood for reconstructed missing transverse momentum	80
52	4.4.2 Likelihood for tau lepton transverse momentum balance	82
53	4.4.3 Secondary vertex information	83
54	4.5 Performance	84
55	5 Analysis Selections	88
56	5.1 Particle Identification	88
57	5.1.1 Muons	88
58	5.1.2 Hadronic Taus	89
59	5.1.3 Missing Transverse Energy	89
60	5.2 Event Selections	89
61	6 Data-Driven Background Estimation	93
62	6.1 Background Enriched Control Regions	94
63	6.2 The Fake-rate Method	96
64	6.2.1 Parameterization of Fake-rates	99
65	6.2.2 Measurement of Fake-rates	100
66	6.2.3 Application of Fake-rates	101
67	6.2.4 “Simple” weight method	102
68	6.2.5 “CDF-type” weights	104
69	6.2.6 k-Nearest Neighbor Fake-rate Calculation	108
70	6.2.7 Results of Background Estimation	109
71	6.3 Template method	111
72	7 Monte Carlo Corrections	119
73	7.1 Muon Identification Efficiency	119
74	7.2 Hadronic Tau Identification Efficiency	122
75	7.3 Muon and Tau Momentum Scale	124
76	7.4 Missing Transverse Energy Correction	125
77	7.5 Pile-up Event Weighting	126
78	8 Systematics and Limit Extraction	128
79	8.1 Signal normalization uncertainties	130
80	8.2 Background normalization uncertainties	130
81	8.3 Shape uncertainties	131
82	8.4 Theory uncertainties	132
83	8.5 Limit Extraction Method	132
84	9 Results	137
85	10 Conclusions	141

87 List of Figures

88	1.1	Fermi contact interaction diagram	5
89	1.2	Muon decaying through intermediate gauge boson	5
90	1.3	QCD Feynman Diagrams	15
91	1.4	Loop corrections to Higgs mass	17
92	1.5	Higgstrahlung production diagram at e^+e^- colliders	22
93	1.6	Gluon fusion Higgs production diagram	22
94	1.7	Vector boson fusion Higgs production diagram	22
95	1.8	Parton luminosity comparison of the LHC and Tevatron	23
96	1.9	SM Higgs cross sections at the LHC	24
97	1.10	SM Higgs branching fractions	25
98	1.11	Cross sections of interest at hadron colliders	26
99	1.12	MSSM Higgs production with association b -quarks	27
100	1.13	MSSM Higgs cross sections at the LHC	28
101	1.14	LEP Standard Model Higgs limit plot	29
102	1.15	Tevatron low mass Standard Model Higgs limit plot	30
103	2.1	Schematic drawings of the CMS detector	34
104	2.2	Material budget of the CMS tracker	37
105	2.3	Momentum and impact parameter resolutions of CMS tracker	38
106	2.4	Energy resolution of the CMS ECAL	40
107	2.5	Muon system material budget and identification efficiency	42
108	3.1	Visible invariant mass of τ lepton decay products	49
109	3.2	Invariant mass photon pairs in reconstructed π^0 mesons	51
110	3.3	Neutral energy fraction in visible τ decays	52
111	3.4	Tau decay mode reconstruction performance	54
112	3.5	Kinematic dependence of decay mode reconstruction	55
113	3.6	Neural network over-training validation plots	58
114	3.7	Kinematic weighting of training sample	59
115	3.8	Neural network output in each decay mode	63
116	3.9	Performance curves for the neural networks used in the TaNC	64
117	3.10	Tau Neural Classifier performance curves for different p_T ranges	65
118	3.11	Tau Neural Classifier transformation performance	67
119	3.12	Transformed neural network output	68
120	3.13	Tau Neural Classifier performance comparison	69
121	3.14	Tau Neural Classifier kinematic performance	70
122	3.15	Invariant mass distribution of PF photon pairs	72
123	4.1	Coordinate system of the SVfit	81

124	4.2	Effect of p_T -balance term on SVfit performance	84
125	4.3	Effect of the visible p_T requirements on muon and hadronic τ decays	85
126	4.4	Effect of the visible p_T requirements for Z and Higgs events	86
127	4.5	Comparison of SVfit with the Collinear Approximation algorithm	86
128	4.6	Comparison of SVfit with the visible mass observable	87
129	6.1	Visible mass distribution of the backgrounds in the signal and control regions	97
130	6.2	SVfit mass distribution of the backgrounds in the signal and control regions	98
131	6.3	p_T and η dependency of tau ID performance	99
132	6.4	Comparison of fake-rate contribution from genuine taus in the simple and	
133		CDF methods	107
134	6.5	Muon transverse momentum in the Fake-rate method	113
135	6.6	Tau-jet transverse momentum in the Fake-rate method	114
136	6.7	Visible mass in the Fake-rate method	115
137	6.8	k -Nearest Neighbor classifier example	116
138	6.9	Comparison of visible mass and SVfit mass	116
139	6.10	Comparison of background shapes in the signal and control regions	117
140	6.11	Visible mass distribution in the final fit of the Template Method	118
141	7.1	Tag-probe muon isolation method	121
142	7.2	Muon isolation correction factors	123
143	7.3	Measurement of hadronic tau identification efficiency	124
144	7.4	Z -recoil E_T^{miss} resolution correction	126
145	7.5	Distribution of number of reconstructed primary vertices per event	127
146	9.1	Distributions of final selected events	140

List of Tables

148	1.1	Chiral supermultiplets in the MSSM	19
149	1.2	Gauge supermultiplets in the MSSM	19
150	1.3	Higgs search channels at LEP	27
151	1.4	Decay modes of the τ lepton	31
152	3.1	Decay mode performance – naive reconstruction	53
153	3.2	Decay mode performance – TaNC reconstruction	53
154	3.3	Neural network training event statistics	57
155	3.4	Variables used in the different TaNC neural networks	75
156	5.1	Analysis backgrounds that include fake taus	90
157	5.2	Event selection criteria applied in the muon + tau-jet channel.	91
158	5.3	High Level Trigger paths used to select $\mu + \tau_h$ events	92
159	6.1	Criteria used to select background enriched control regions	95
160	6.2	Comparison of background control region yields in data and the prediction from simulation	96
161	6.3	Fake-rate “simple” method closure test results	103
162	6.4	Fake-rate “CDF” method closure test results	106
163	6.5	Fake-rate method results	110
164	6.6	Fake-rate Method predicted yields in like-sign control region	111
165	6.7	Background yields measured using the Template Method	112
166			
167	7.1	Muon trigger, identification, and isolation correction factors	122
168	8.1	Effect of normalization uncertainties on signal efficiency times acceptance .	133
169	8.2	Contributions of different MSSM Higgs boson types at different m_{A^0}	135
170	8.3	Summary of systematic uncertainties represented by nuisance parameters in the likelihood, their representation method and magnitudes.	136
171			
172	9.1	Final analysis yields and background expectations	138
173	9.2	Expected signal yields at $\tan\beta = 30$	139

Chapter 1

The Standard Model and Beyond

?⟨ch:theory⟩?

§1.1 The Standard Model

The Standard Model (SM) is a “theory of almost everything” that describes the interactions of elementary particles. The Standard Model is a *quantum field theory*, first appearing in its modern form in the middle of the 20th century. The model is the synthesis of the independent theories of electromagnetism, and the weak and strong nuclear forces. Each of these theories was used to describe different phenomena, which each have extremely different strengths and act at different scales. The interaction of light and matter is described by Quantum Electrodynamics (QED), a relativistic field extension of the theory of electromagnetism. The physics of radioactivity and nuclear decay was described by the Fermi theory of weak interactions and the forces that strong nuclear force binds the nuclei of atoms was described by Yukawa. An overview of these theories will be presented in this chapter.

The feature that united the disparate theories into the Standard Model was the application of the principle of *local gauge invariance*. The principle of gauge invariance first found success in QED, which predicted electromagnetic phenomenon with astounding accuracy. Local gauge invariance is now believed to a fundamental feature of nature that underpins all theories of elementary particles. Furthermore, the development of the complete Standard Model as it is known today was precipitated by Goldstones’s work on spontaneous symmetry breaking [1, 2], which produces an effective Lagrangian with additional massless “Goldstone” bosons. Higgs (and others) [3, 4, 5] developed these ideas into what is ultimately called the “Higgs Mechanism,” which uses a combination of new fields with broken symmetry to give mass to the Goldstone bosons.

197 In the 1960s, Glashow [6], Weinberg [7], and Salam [8] developed the above ideas into the
 198 electroweak model, which unified QED with the weak force using intermediate weak bosons
 199 in a gauge theory whose symmetry was spontaneously broken using the Higgs mechanism.
 200 This unified theory has been incredibly experimentally successful and is the foundation of
 201 modern particle theory.

202 §1.1.1 Quantum Electrodynamics and Gauge Invariance

QEDandGaugeInvariance)

203 The theory of QED is a modern extension of Maxwell’s theory of electromagnetism, describ-
 204 ing the interaction of matter with light. The development of QED is a result of efforts to
 205 develop a quantum mechanical formulation of electromagnetism compatible with the theory
 206 of Special Relativity. QED is a *gauge* theory, which means that the physical observables
 207 are invariant under local gauge transformations. Requiring local gauge invariance gives rise
 208 to a “gauge” field, which can be interpreted as particles that are exchanged during an
 209 interaction.

210 In the following, we first describe the Dirac equation for a free electron, which is the
 211 relativistic extension of the Schroedinger equation for spin 1/2 particles. We then show that
 212 requiring the corresponding Lagrangian of the free charged particle to be invariant under
 213 local gauge transformations creates an effective gauge boson field. This “gauge field” creates
 214 terms in the Lagrangian that represent interactions between the particles.

The Dirac equation is the equation of motion of a free spin 1/2 particle of mass m and
 is derived from the energy–momentum relationship of relativity

$$p^\mu p_\mu - m^2 c^2 = 0. \quad (1.1) \quad \text{eq:EnergyPRelat}$$

Dirac sought to express this relationship in the framework of quantum mechanics by apply-
 ing the transformation

$$p_\mu \rightarrow i\hbar\partial_\mu \quad (1.2) \quad \text{eq:QuantizeMom}$$

to equation Equation 1.1, but with the requirement that the resulting equation be first
 order in time.¹ To achieve this, Dirac factorized Equation 1.1 into

$$(\gamma^\kappa p_\kappa + mc)(\gamma^\mu p_\mu - mc) = 0, \quad (1.3) \quad \text{eq:DiracEquation}$$

¹A detailed discussion of this topic is available in [9].

where γ^μ is a set of four 4×4 matrices referred to as the Dirac matrices. The equation of motion is obtained by choosing either term (they are equivalent) from the left hand side of Equation 1.3 and making the substitution in Equation 1.2.

$$i\hbar\gamma^\mu\partial_\mu\psi - mc\psi = 0. \quad (1.4) \quad \text{eq:DiracEquation}$$

215 The solutions ψ of the Dirac equation are called “Dirac spinors,” and represent the quantum
216 mechanical state of spin 1/2 particles.

The Lagrangian corresponding to the Dirac equation (1.4) is

$$\mathcal{L} = \bar{\psi}(i\hbar c\gamma^\mu\partial_\mu - mc^2)\psi, \quad (1.5) \quad \text{eq:FreeQEDLagr}$$

where ψ is the spinor field of the particle in question, \hbar is Planck’s constant, c the speed of light, and γ^μ are the Dirac matrices. As $\bar{\psi}$ is the Hermitian conjugate of ψ , the Lagrangian is invariant under the global gauge transformation

$$\psi' \rightarrow e^{i\theta}\psi. \quad (1.6) \quad \text{eq:U1GaugeTran}$$

The Lagrangian is invariant under *local* gauge translations if θ can be defined differently at each point in space, i.e. if $\theta = \theta(x)$ in equation 1.6. However, as the derivative operator ∂_μ in equation 1.5 does not commute with $\theta(x)$, the Lagrangian must be modified to satisfy local gauge invariance. This modification is accomplished with the use of a “gauge covariant derivative.” By making the replacement

$$\partial_\mu \rightarrow D_\mu = \partial_\mu - \frac{ie}{\hbar}A^\mu \quad (1.7) \quad \{?\}$$

in equation 1.5, where $A^\mu = \partial^\mu\theta(x)$ and e is the electric charge, the Lagrangian becomes locally gauge invariant:

$$\mathcal{L} = \bar{\psi}(i\hbar c\gamma^\mu D_\mu - mc^2)\psi. \quad (1.8) \quad \text{eq:LocalQEDLagr}$$

The difference between the locally (1.8) and the globally (1.5) gauge invariant Lagrangians is then

$$\mathcal{L}_{int} = \frac{e}{\hbar}\bar{\psi}\gamma^\mu\psi A_\mu. \quad (1.9) \quad \{?\}$$

This term can be interpreted as the coupling between the particle and the gauge boson (force carrier) fields. The coupling is proportional to the constant e , which is associated with the electric charge. This is consistent with the experimental observation that particles with zero electric charge do not interact electromagnetically with each other. In this interpretation, the electromagnetic force between two charged particles is caused by the exchange of gauge bosons (photons). The existence of this “minimal coupling” is *required* if the Lagrangian

is to satisfy local gauge invariance. The addition of a term with the gauge Field Strength Tensor to represent the kinetic term of the gauge (photon) field yields the QED Lagrangian:

$$\mathcal{L}_{QED} = \bar{\psi}(i\hbar c\gamma^\mu D_\mu - mc^2)\psi - \frac{1}{4\mu_0}F_{\mu\nu}F^{\mu\nu}. \quad (1.10) \{?\}$$

The gauge symmetry group of QED is $U(1)$, the unitary group of degree 1. This symmetry can be visualized as a rotation of a two-dimensional unit vector. (The application of the gauge transformation $e^{i\theta}$ rotates a number in the complex plane.) In a gauge theory the symmetry group of the gauge transformation defines the behavior of the gauge bosons and thus the interactions of the theory.

§1.1.2 The Weak Interactions

`<sec:WeakInteractions>`

The theory of Weak Interactions was created to describe the physics of radioactive decay. The first formulation of the theory was done by Fermi [?] to explain the phenomenon of the β decay of neutrons. The initial theory was a four-fermion “contact” theory. In a contact theory, all four fermions come involved in the β -decay are connected at a single vertex. The Fermi theory Hamiltonian for the β -decay of a proton is then [10]

$$H = \frac{G_\beta}{\sqrt{2}} [\bar{\psi}_p \gamma_\mu (1 - g_A \gamma_5) \psi_n] [\bar{\psi}_e \gamma^\mu (1 - \gamma_5) \psi_\nu] + h.c., \quad (1.11) \text{eq:FermiTheoryF}$$

where G_β is the Fermi constant and g_A is the relative fraction of the interaction with axially Lorentz structure. The value of g_A was determined experimentally to be 1.26. One of the most notable things discovered about the weak force is that weak interactions violate parity; that is, the physics of the interaction change (or become disallowed) under inversion of the spatial coordinates. This is evidenced by the $(1 - \gamma_5)$ term in Equation 1.11. This term is the “helicity operator”; the left and right “handed” helicity states are eigenstates of this term.

$$h = (1 - \gamma_5)/2$$

$$h\psi_R = \frac{1}{2}\psi_R$$

$$h\psi_L = -\frac{1}{2}\psi_L$$

It is observed that only left-handed neutrinos (or right-handed anti-neutrinos) participate in the weak interaction.

FixMe: *check handedness is correct*

The Fermi interaction can describe both nuclear β decay ($p \rightarrow n + e^+ + \bar{\nu}_e$) as well as the decay of a muon into an electron ($\mu \rightarrow \nu_\mu + e + \bar{\nu}_e$, Figure 1.1). Furthermore, the

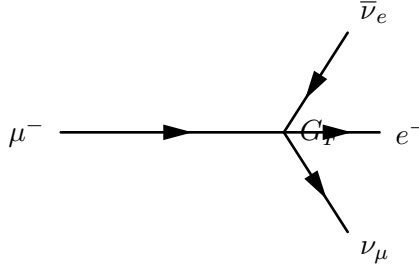


Figure 1.1: Feynman diagram of muon decay in Fermi contact interaction theory.

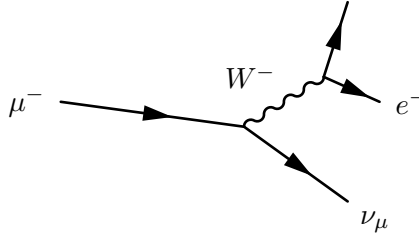


Figure 1.2: Feynman diagram of muon decay proceeding through an intermediate gauge boson W^- .

coupling constant G is found to be a *universal* constant in weak interactions, in that it is the same for interactions regardless of the particle species participating in the interaction. That is, $G_\mu = G_e = G_F$. Using an Hamiltonian analogous to Equation 1.11 for muon decay, the decay amplitude M is found to be

$$M = \frac{G_F}{\sqrt{2}} \left[\bar{u}_{\nu_\mu} \gamma_\rho \frac{1 - \gamma_5}{2} u_\mu \right] \left[\bar{u}_{\nu_e} \gamma_\rho \frac{1 - \gamma_5}{2} u_e \right]. \quad (1.12) \quad \text{eq:ContactAmpli}$$

232 However, the contact interaction form of Fermi's theory is not complete. When applied
 233 to scattering processes, the interaction violates unitarity: the calculated cross section grows
 234 with the center of mass energy, so that for some energy the probability for an interaction
 235 is greater than one. Furthermore, the techniques successfully used to “renormalize”² QED
 236 fail when applied to the Fermi interaction.

The first attempt to solve the problems with the Fermi theory was made by introducing an intermediate weak boson [6]. The contact interaction is replaced by a massive propagator, the W^\pm bosons. The decay of a muon to an electron and two neutrinos then proceeds as pictured in Figure 1.2 with an amplitude given [10] by

$$M = - \left[\frac{g}{\sqrt{2}} \bar{u}_{\nu_\mu} \gamma_\rho \frac{1 - \gamma_5}{2} u_\mu \right] \frac{-g^{\rho\sigma} + \frac{q^\rho q^\sigma}{M_W^2}}{q^2 - M_W^2} \left[\frac{g}{\sqrt{2}} \bar{u}_{\nu_e} \gamma_\rho \frac{1 - \gamma_5}{2} u_e \right]. \quad (1.13) \quad \text{eq:WeakPropaga}$$

The presence of the large gauge boson mass term M_W^2 in the denominator of the central

²Renormalization of quantum field theories is a broad topic beyond the scope of this thesis. Briefly, the process involves “absorbing” infinite divergences that occur in higher-order interactions into physical observables [9].

term of Equation 1.13 is the reason why the contact interaction original formulated by Fermi effectively described low-energy weak phenomenon. When the momentum transfer q in the interaction is small compared to M_W , the effect of the propagator is an effective constant. In the low energy limit, the full propagator in equation 1.13 is equivalent to the Fermi contact interaction in 1.12 as

$$\lim_{q/M_W \rightarrow 0} \frac{g^2}{8(q^2 - M_W^2)} = \frac{G_F}{\sqrt{2}}. \quad (1.14) \quad \boxed{\text{eq:ContactVersus}}$$

Unfortunately, the weak boson exchange model did not solve the problems of unitarity and renormalizability in the weak interaction. However, the form of the boson-exchange propagator in Equation 1.14 suggests the observed “weakness” of the weak interactions is an artifact of the presence of the massive propagator (M_W) and that the fundamental scale of the interaction g is the same order of magnitude as that of QED, $g \approx e$. This observation lead to the unification of the electromagnetic and weak forces, which we describe in the next sections.

§1.1.3 Spontaneous Symmetry Breaking

(sec:SSB)
In the early 1960s Glashow, Weinberg, and Salam published a series of papers describing how the electromagnetic and weak forces could be unified into a common “electroweak” force. The fact that at low energy the electromagnetic and weak forces appear to be separate phenomena is due to the fact that the symmetry of the electroweak gauge group is “spontaneously broken.” Modern field theories (both the Standard Model and beyond) are predicated on the idea that the all interactions are part of a single, unified symmetry group and the differences between various scales (electromagnetic, weak, etc.) at lower energies are due to the unified symmetry being spontaneously broken.

A symmetry of a Lagrangian is spontaneously broken when the ground state, or vacuum, is at a value which about which the Lagrangian is not symmetric. In quantum field theories, a particle is interpreted as quantized fluctuations of its corresponding field about some constant (vacuum) ground state. The “effective” Lagrangian that we observe in the (low energy) laboratory would be the expansion of the Lagrangian about this stable point. The effective Lagrangian no longer obeys the original symmetry, which has been “broken”. We give a brief example of the phenomenological effects of a spontaneously broken symmetry

in a toy model, following the treatment in [10].

$$\mathcal{L} = \frac{1}{2}\partial_\mu\phi_1\partial^\mu\phi_1 + \frac{1}{2}\partial_\mu\phi_2\partial^\mu\phi_2 - V(\phi_1^2 + \phi_2^2) \quad (1.15) \quad \text{eq:ToySSBLagrangian}$$

253 The toy Lagrangian in Equation 1.15 has a global $U(1)$ ³ symmetry and consists of two
 254 real-valued fields, ϕ_1 and ϕ_2 . The particle mass spectra of the theory is given by expanding
 255 the field potential $V(\phi_1, \phi_2)$ about its minimum, $(\phi_1^{min}, \phi_2^{min})$. The first three terms in the
 256 series are found by

$$\begin{aligned} V(\phi_1, \phi_2) &= V(\phi_1^{min}, \phi_2^{min}) + \sum_{a=1,2} \left(\frac{\partial V}{\partial \phi_a} \right)_0 (\phi_a - \phi_a^{min}) \\ &+ \frac{1}{2} \sum_{a,b=1,2} \left(\frac{\partial^2 V}{\partial \phi_a \partial \phi_b} \right)_0 (\phi_a - \phi_a^{min})(\phi_b - \phi_b^{min}) + \dots \end{aligned} \quad (1.16) \quad \text{eq:ExpandedPotential}$$

Since at the minimum the partial derivative of V is zero with respect to all fields, the second term in equation 1.16 is zero. The third term determines the masses of the particles in the theory. Since a mass term for a particle corresponding to a field ϕ_n in the Lagrangian appears as $\frac{1}{2}m^2\phi_n\phi_n$, we can identify

$$\left(\frac{\partial^2 V}{\partial \phi_a \partial \phi_b} \right)_{\phi^{min}} \quad (1.17) \quad \text{eq:MassMatrixTerms}$$

257 as the a th row and b th column in the “mass matrix”. Off diagonal terms in this matrix
 258 indicate mixing terms between the fields. By diagonalizing the matrix, the combinations of
 259 fields which correspond to the physical particles (the “mass eigenstates”) are found. The
 260 m^2 of each particle is then the corresponding entry in the diagonal of the mass matrix.

The particle spectra of the model depends heavily on the form of the potential. An illustrative form (that is renormalizable and bounded from below) of a possible configuration for the potential V in Equation 1.15 is

$$V(\phi_1^2, \phi_2^2) = \frac{m^2}{2}(\phi_1^2 + \phi_2^2) + \frac{\lambda}{4}(\phi_1^2 + \phi_2^2)^2. \quad (1.18) \quad \text{eq:SSBPotential}$$

261 If the parameters m^2 and λ are both positive, then the minimum of V is at the origin ($\phi_1 =$
 262 $\phi_2 = 0$). In this case, the mass matrix term in Equation 1.16 takes the form $\left(\frac{\partial^2 V}{\partial \phi_a \partial \phi_b} \right)_0 =$
 263 $\frac{m^2}{2}\delta_{ab}$, where δ_{ab} is the Kronecker delta function. Therefore the mass matrix is already
 264 diagonalized, and the ϕ_1 and ϕ_2 both correspond to particles with mass m . If the m^2

³Technically, the symmetric transformation is

$$\begin{pmatrix} \phi_1 \\ \phi_2 \end{pmatrix} \rightarrow \begin{pmatrix} \phi'_1 \\ \phi'_2 \end{pmatrix} = \begin{pmatrix} \cos \theta & -\sin \theta \\ \sin \theta & \cos \theta \end{pmatrix} \begin{pmatrix} \phi_1 \\ \phi_2 \end{pmatrix},$$

which is $\mathcal{O}(2)$. However, this transformation is equivalent to $U(1)$, as the two real fields ϕ_1 and ϕ_2 can be seen to correspond to the real and imaginary parts of a complex field ϕ that does transform according to $U(1)$.

parameter in Equation 1.18 is negative, the spectrum is dramatically different. After making the replacement $m^2 = -\mu^2$ ($\mu^2 > 0$), the extrema of V are no longer unique. The requirement of $\frac{\partial V}{\partial \phi_i} = 0$ for all i is satisfied in two cases:

$$(\phi_1^{min}, \phi_2^{min}) = (0, 0) \quad (1.19) \quad \text{eq:WignerPoint}$$

$$(\phi_1^{min})^2 + (\phi_2^{min})^2 = \frac{\mu^2}{\lambda} = \nu^2. \quad (1.20) \quad \text{eq:NambuGoldst}$$

If the vacuum state is defined at the point in Equation 1.19, the symmetry is unbroken and the mass spectra is unchanged. However, the system is unstable at this point, as it is a local maximum. The true global minimum is defined as the set of points which satisfy Equation 1.20, which form a continuous circle in $\phi_1 - \phi_2$ space (and is therefore infinitely degenerate). We can choose any point on the circle as the vacuum expectation value (VEV). If the point $(\phi_1^{min} = \nu, \phi_2^{min} = 0)$ ⁴ is chosen, evaluating Equation 1.17 yields the mass matrix

$$\left(\frac{\partial^2 V}{\partial \phi_a \partial \phi_b} \right)_{\phi^{min}} = \begin{pmatrix} v^2 & 0 \\ 0 & 0 \end{pmatrix}.$$

FixMe:
check matrix

Breaking the symmetry has changed the mass spectrum of the physical particles in the model. There is now a massive particle with $m = v$ and a massless particle. This massless particle is called the “Goldstone boson.” Goldstone found [1] that a massless particle appears for each generator in the symmetry group that is broken.

§1.1.4 The Higgs Mechanism

(sec:HiggsMech) As in section 1.1.1, extending the gauge symmetry requirement to be *locally* invariant creates interesting consequences for models that have spontaneously broken symmetry. This gives rise to the “Higgs Mechanism,” which we overview here. For simplicity we will again consider a model with $U(1)$ symmetry. The model is identical to the one presented in section 1.1.3, with two exceptions. First, we express the two real fields ϕ_1 and ϕ_2 as a single complex-valued field ϕ . Second, the model is required to be locally $U(1)$ invariant, and so uses the gauge-covariant derivatives, minimal coupling to the gauge field, and contains the kinetic

⁴The point chosen for the VEV here is not arbitrary. One can choose any point that satisfies Equation 1.20 as the VEV. However, after the mass matrix is diagonalized, there will always be one physical field with a VEV = ν and one with a VEV = 0. Therefore the physical content of the theory does not depend on the choice of VEV.

term for the gauge field, as discussed in section 1.1.1. The unbroken Lagrangian is

$$\mathcal{L} = -\frac{1}{4}F_{\mu\nu}F^{\mu\nu} + (D_\mu\phi^*)(D^\mu\phi) - V(\phi^*\phi) \quad (1.21) \text{eq:LocalInvariant}$$

$$V(\phi^*\phi) = -\mu^2\phi^*\phi + \lambda(\phi^*\phi)^2, \quad (1.22) \text{eq:PotentialLocal}$$

where $F_{\mu\nu}$ is related to the gauge field by $F_{\mu\nu} = \partial_\mu A_\nu - \partial_\nu A_\mu$. The Lagrangian is invariant under the local $U(1)$ gauge transformation

$$\begin{aligned} \phi \rightarrow \phi' &= e^{-i\alpha(x)}\phi \\ A_\mu \rightarrow A'_\mu &= A_\mu - \frac{1}{2}\partial_\mu\alpha(x). \end{aligned} \quad (1.23) \{?\}$$

The potential is minimized when $\phi^*\phi = \frac{\mu^2}{2\lambda}$. To simplify the algebra, we can re-parameterize the field into a real part $\eta(x)$ defined about ν , the minimum of V , and a complex phase parameterized by $\theta(x)/\nu$

$$\phi(x) = \frac{1}{\sqrt{2}}(\nu + \eta(x))e^{i\theta(x)/\nu}. \quad (1.24) \text{eq:HiggsMechanism}$$

If the gauge transform is chosen to be $\alpha(x) = \theta(x)/\nu$, the fields are defined in the so-called “unitary gauge”⁵ and have the special forms

$$\begin{aligned} \phi(x) \rightarrow \phi'(x) &= \frac{1}{\sqrt{2}}(\nu + \eta(x)) \\ A_\mu(x) \rightarrow B_\mu(x) &= A_\mu(x) - \frac{1}{e\nu}\partial_\mu\theta(x) \end{aligned} \quad (1.25) \text{eq:AfterUnitaryGauge}$$

The kinetic term of the gauge field $F_{\mu\nu}$ is invariant under this transformation. If the gauge transformations of Equation 1.25 are substituted into the Lagrangian (1.21) the effective Lagrangian at the minimum of V is

$$\begin{aligned} \mathcal{L} = & \frac{1}{2}\partial_\mu\eta\partial^\mu\eta - \mu^2\eta^2 \\ & - \frac{1}{4}F_{\mu\nu}F^{\mu\nu} + \frac{1}{2}(e\nu)^2B_\mu B^\mu \\ & + \frac{1}{2}e^2B_\mu B^\mu\eta(\eta + 2\nu) - \lambda\nu\eta^3 - \frac{\lambda}{4}\eta^4. \end{aligned} \quad (1.26) \text{eq:HiggsMechanism}$$

The breaking of the original symmetry has dramatically altered the physical consequences of the model. In its unbroken form, the model described by Equation 1.21 would produce two real massive particles and one massless gauge boson mandated by local gauge invariance. After symmetry breaking, the effective Lagrangian in Equation 1.26 contains a massive scalar η with $m = \sqrt{2\mu^2}$ and a *massive* gauge boson B_μ with mass $m = \sqrt{2}e\nu$. By acquiring a mass, the gauge boson B_μ has acquired the degree of freedom (as it can now be longitudinally polarized) previously associated to the second degree of freedom in the

⁵In the unitary gauge, the choice of gauge ensures that the mass matrix is diagonalized.

scalar ϕ field. This phenomenon, known as the “Higgs Mechanism,” is a simplified version of the techniques successfully used to unify the electromagnetic and weak forces that we will discuss in the next section.

§1.1.5 Electroweak Unification

In the 1960s, the ideas of local gauge invariance in field theories, spontaneous symmetry breaking, and the Higgs mechanism were combined by Glashow [6], Weinberg [7] and Salam [8] to form the unified theory of electroweak interactions, the nucleus of the Standard Model. This model successfully unified the electromagnetic and weak interactions into a unified theory with a larger symmetry group. The reason for the empirically observed difference in scales between two interactions is due to the larger, unified symmetry group being broken. This broken symmetry creates heavy gauge bosons via the Higgs mechanism, whose large mass decreases the strength of “weak” interactions at low energy, as discussed in Section 1.1.2. The model successfully predicted the existence and approximate masses of the weak force carriers, the W^\pm and Z bosons. These particles were later observed [11, 12, 13, 14] with the predicted masses at the UA1 and UA2 experiments.

To provide a simple introduction to the mechanisms of the model, we will start with a model that includes only one family of leptons, the electron e and its associated neutrino ν_e . Following once again the treatment of [10], we describe the representation of the e and ν_e in the chosen symmetry group of the model. We then construct a locally gauge invariant Lagrangian with spontaneously broken symmetry, and examine the particle content of the resulting model.

The form of the charged current $J_\mu(x) = \bar{u}_{\nu_e} \gamma_\mu \frac{1-\gamma_5}{2} u_e$ in the weak interaction amplitudes (1.12) indicates that the left-handed electron and neutrino (remember that the $(1 - \gamma_5)$ kills any right-handed spinors) can be combined into a doublet L of $SU(2)$.

$$L = \frac{1 - \gamma_5}{2} \begin{pmatrix} \nu_e \\ e^- \end{pmatrix} = \begin{pmatrix} \nu_e \\ e^- \end{pmatrix}_L \quad (1.27) \quad \boxed{\text{eq:EWDouletFc}}$$

316 The operators that operate on “weak isospin,” the quantum of $SU(2)_L$, are

$$\tau^+ = \frac{\tau^1 + i\tau^2}{2} = \begin{pmatrix} 0 & 1 \\ 0 & 0 \end{pmatrix} \quad (1.28) \quad \text{?eq:Su2Generator}$$

$$\tau^- = \frac{\tau^1 - i\tau^2}{2} = \begin{pmatrix} 0 & 0 \\ 1 & 0 \end{pmatrix}, \quad (1.29) \quad \text{eq:Su2Generator}$$

where the τ^i are the Pauli matrices. The weak currents J_μ^\pm can be written by combining equations 1.27–1.29

$$J_\mu^\pm = \bar{L}\gamma_\mu\tau^\pm L. \quad (1.30) \quad \text{eq:WeakCurrentL}$$

317 Since τ^1 , τ^2 , and τ^3 are the generators of the $SU(2)$ group, we can complete the group
 318 by adding a neutral current to the charged currents of Equation 1.30. The τ^3 generator is
 319 diagonal, so the charge of the current is zero and no mixing of the fields occur:

$$\begin{aligned} J_\mu^3 &= \bar{L}\gamma_\mu\frac{\tau^3}{2}L \\ &= \bar{L}\gamma_\mu\frac{1}{2}\begin{pmatrix} 1 & 0 \\ 0 & -1 \end{pmatrix}L \\ &= \frac{1}{2}\bar{\nu}_e\gamma_\mu\nu_e - \frac{1}{2}\bar{e}_L\gamma_\mu e_L. \end{aligned} \quad (1.31) \quad \text{eq:EWNeutralCu}$$

320 Naively one might hope that the neutral current of Equation 1.31 would correspond to the
 321 electromagnetic (photon) current of QED. However, this is impossible for two reasons. First,
 322 the right-handed component e_R does not appear in the current, so this interaction violates
 323 parity, a known symmetry of the electromagnetic interactions. Second, the current couples to
 324 neutrinos, which have no electric charge. Therefore, the “charge” corresponding to the $SU(2)$
 325 gauge symmetry generators $T^i = \int J_0^i(x)d^3x$ cannot be that of the QED, and the gauge
 326 group must be enlarged to include an additional $U(1)$ symmetry. The generator of the new
 327 symmetry must commute with the generators of the $SU(2)_L$ group. The symmetry cannot
 328 be directly extended with $U(1)_{em}$ as the electromagnetic charge $Q = \int (e_L^\dagger e_L + e_R^\dagger e_R)d^3x$
 329 does not commute with T^i . The solution is to introduce the “weak hypercharge” $\frac{Y}{2} = Q - T^3$,
 330 which commutes the generators of $SU(2)_L$. Thus the symmetry group of the electroweak
 331 model is $SU(2)_L \times U(1)_Y$.

332 The $SU(2)_L \times U(1)_Y$ gauge invariant Lagrangian is written

$$\begin{aligned}\mathcal{L} = & \bar{L}i\gamma^\mu(\partial_\mu - ig\frac{\vec{\tau}}{2} \cdot \vec{A}_\mu + \frac{i}{2}g'B_\mu)L \\ & + \bar{R}i\gamma^\mu(\partial_\mu + \frac{i}{2}g'B_\mu)R \\ & - \frac{1}{4}F_{\mu\nu}^i F^{i\mu\nu} - \frac{1}{4}B_{\mu\nu}B^{\mu\nu}.\end{aligned}\tag{1.32} \text{?eq:FermionAndC}$$

333 As R is a singlet in $SU(2)$, it does not couple to the $SU(2)$ gauge bosons A_μ^i . For this
334 Lagrangian to correspond to empirical observations at low energy, the $SU(2)_L \times U(1)_Y$
335 must be broken. As $U(1)_{em}$ symmetry is observed to be good symmetry at all scales the
336 broken Lagrangian must be invariant under $U(1)_{em}$.

337 To accomplish the symmetry breaking, we introduce a new $SU(2)$ doublet of complex
338 Higgs fields ϕ that have hypercharge $Y = 1$, and contribute \mathcal{L}_S to the Lagrangian:

$$\phi = \begin{pmatrix} \phi^+ \\ \phi^0 \end{pmatrix}\tag{1.33} \{?\}$$

$$\mathcal{L}_S = (D_\mu\phi)^\dagger(D^\mu\phi) - V(\phi^\dagger\phi),\tag{1.34} \{?\}$$

where D_μ is the gauge covariant derivative containing couplings to both the $SU(2)_L$ and
 $U(1)_Y$ gauge fields, and V has a form analogous to V in Equation 1.22. At this point we
also add $SU(2)_L \times U(1)_Y$ invariant ‘‘Yukawa’’ terms

$$\mathcal{L}_Y = -G_e(\bar{L}\phi R + \bar{R}\phi^\dagger L) + h.c.\tag{1.35} \text{eq:YukawaTerms}$$

339 to the Lagrangian which couple the fermions (L and R) to the Higgs field. After symmetry
340 breaking these terms will allow the fermions to acquire masses. By choosing the m^2 and λ
341 parameters of V appropriately, the new ϕ field acquires a non-zero VEV and the symmetry
342 is spontaneously broken.

At the minimum of V , the Higgs field satisfies $\phi^\dagger\phi = \frac{v^2}{2}$ and the Higgs fields has a
VEV of

$$\phi_{min} = \begin{pmatrix} 0 \\ v/\sqrt{2} \end{pmatrix}.\tag{1.36} \{?\}$$

The new symmetry of the model can be confirmed by looking at the action of the different
symmetry generators on the VEV. If the generator acting on the vacuum state has a non-
zero value, then the corresponding symmetry is broken. It can then be seen that the original
symmetry generators T^+ , T^- , T^3 , and Y are all broken. The vacuum is invariant under Q ,

the generator of $U(1)_{em}$

$$Q\phi_{min} = (T^3 + \frac{Y}{2}) \begin{pmatrix} 0 \\ v/\sqrt{2} \end{pmatrix} = 0,$$

so the broken Lagrangian contains the correct symmetry properties.

The gauge boson content of the electroweak interaction is obtained by parameterizing the Higgs field in the magnitude–phase notation of Equation 1.24 and using the unitary gauge (see Section 1.1.4), where the gauge transformation is chosen so Higgs field is real.

The Higgs scalar doublet is then

$$\phi' = \begin{pmatrix} 0 \\ \frac{1}{\sqrt{2}}(\nu + H(x)) \end{pmatrix} = \frac{1}{\sqrt{2}}(\nu + H(x))\chi. \quad (1.37) \text{ ?eq:HiggsFieldPa}$$

The mass spectrum of the gauge bosons of the electroweak interaction (the photon, W^\pm , and Z) is determined by the interaction of the gauge field terms in the covariant derivative with the non–zero vacuum expectation value ν of the scalar Higgs field ϕ

$$(D_\mu \phi)' = (\partial_\mu - ig\frac{\vec{\tau}}{2} \cdot \vec{A}'_\mu - \frac{i}{2}g'B'_\mu)\frac{1}{\sqrt{2}}(\nu + H)\chi.$$

The terms in the expansion of the kinetic term of the Higgs field that are quadratic in ν^2 and a gauge boson field give the mass associated to that boson, and can be written as

$$\mathcal{L}_{mass} = \frac{\nu^2}{8}(g^2 A'^1_\mu A'^1{}^\mu + g^2 A'^2_\mu A'^2{}^\mu + (gA'^3_\mu - g'B'_\mu)^2). \quad (1.38) \text{ eq:GaugeBosonM}$$

The A'^1_μ and A'^2_μ fields can be combined such that the first two terms in Equation 1.38 are equivalent to the mass term of a charged boson

$$W^\pm_\mu = \frac{A'^1_\mu \mp iA'^2_\mu}{2}. \quad (1.39) \{?\}$$

This is the familiar W^\pm boson of β and muon decay, and has mass $M_W = \frac{1}{2}g\nu$. The third

term in Equation 1.38 can be written in matrix form and then diagonalized into mass

eigenstates

$$\begin{aligned} & \frac{\nu^2}{8} \begin{pmatrix} A'^3_\mu & B'_\mu \end{pmatrix} \begin{pmatrix} g^2 & -gg' \\ -gg' & g'^2 \end{pmatrix} \begin{pmatrix} A'^3{}^\mu \\ B'^\mu \end{pmatrix} \\ \rightarrow & \frac{\nu^2}{8} \begin{pmatrix} Z_\mu & A_\mu \end{pmatrix} \begin{pmatrix} g^2 + g'^2 & 0 \\ 0 & 0 \end{pmatrix} \begin{pmatrix} Z^\mu \\ A^\mu \end{pmatrix}, \end{aligned} \quad (1.40) \{?\}$$

giving a massive Z boson with

$$M_Z = \frac{\nu}{2}\sqrt{g^2 + g'^2} \quad (1.41) \text{ eq:ZBosonMass}$$

and the massless photon A_μ of QED. The mass of the Z is related to the mass of the W^\pm

by

$$M_Z \equiv \frac{M_W}{\cos \theta_W}, \quad (1.42) \{?\}$$

where θ_W is the “Weinberg angle,” which must be determined from experiment. As the Fermi contact interaction of Section 1.1.2 is an effective theory of the weak sector, the value of G_F obtained from β and muon decay experiments give clues to the masses of the W and Z .

$$M_W = \frac{1}{2} \left(\frac{e^2}{\sqrt{2}G_F} \right)^{(1/2)} \frac{1}{\sin \theta_W} \approx \frac{38 \text{ GeV}}{\sin \theta_W} > 37 \text{ GeV} \quad (1.43) \{?\}$$

$$M_Z \approx \frac{76 \text{ GeV}}{\sin 2\theta_W} > 76 \text{ GeV}. \quad (1.44) \{?\}$$

The discovery of the W [11, 12] and Z [13, 14] at the CERN SPS was a huge triumph for the electroweak model.

The model that is presented in this section assumes only one species of leptons, the electron and its associated neutrino. The electroweak model is trivially extended [10] to include the other species (μ , τ) of leptons and the three families of quarks. The masses of the fermions are determined by the Yukawa terms in Equation 1.35. Each particle species has a Yukawa term relating the Higgs VEV to its mass that is not constrained by the theory, and must be determined by experiment.

§1.1.6 Quantum Chromodynamics

After electroweak unification, the Standard Model is completed by the theory of Quantum Chromodynamics (QCD), which describes the interactions between quarks and gluons. QCD is a broad field and only a brief introduction to its motivations and the phenomenology relevant to the analysis presented in this thesis is contained in this section. The existence of quarks as composite particles of hadrons was first proposed by Gell–Man and Zweig to explain the spectroscopy of hadrons. QCD is an $SU(3)$ non–Abelian gauge theory which is invariant under *color* transformations. Color is the charge of QCD and comes in three types: red, green and blue. The gauge boson that carries the force of QCD is called the gluon, which is massless as the $SU(3)_c$ color symmetry is unbroken.

There are three marked differences between the photon of QED and the gluon of QCD. First, the gluon carries a color charge, while the photon is electrically neutral. This has the consequence that a gluon can couple to other gluons. Secondly, it is found that no

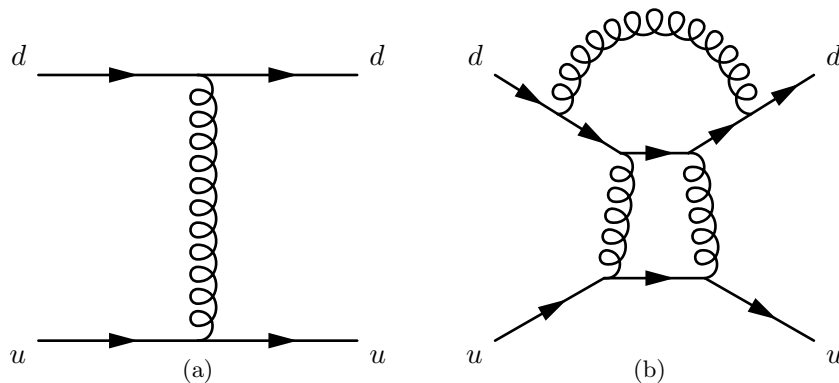


Figure 1.3: Feynman diagrams of a first-order (a) QCD interaction and a multi-loop (b) QCD interaction that have the same initial and final states. Each internal gluon propagator contributes a factor of g_s , the strong coupling constant, to the amplitude. Since $g_s > 1$, multi-loop diagrams have a larger contribution than simpler diagrams.

colored object exists in nature. The corollary of this is that it is believed to be impossible for a single quark or gluon to be observed. The mechanism that gives rise to this effect is called “color confinement.” The strength of the strong force between two interacting colored objects increases with distance. If two colored objects in a hadron are pulled apart, the energy required to separate them will eventually be large enough to produce new colored objects, resulting in two (or more) colorless hadrons. Finally, at low energy, QCD is non-perturbative. What this means in practice is that when computing an amplitude from a QCD Feynman diagram, additional gluon interactions contribute a value greater than one. The dominance of multi-loop diagrams is illustrated in Figure 1.1.6. Thus higher order diagrams with many internal loops cannot be ignored in QCD. In practice what is done is to “factorize” QCD interaction amplitudes into a perturbative (high-energy) part and a non-perturbative part. The perturbative portion is calculable using the Feynman calculus; the non-perturbative must be estimated from parameterization functions that are experimentally measured.

The practical consequence of color confinement to a physicist at a high-energy particle physics experiment is the production of quark and gluon “jets,” which are high multiplicity sprays of particles observed in the detector. In a proton-proton collision, quarks and gluons can be knocked off the incident protons. These quarks and gluons immediately “hadronize,” surrounding themselves with additional hadrons, the majority of which are charged and neutral pions. Heavier quarks, such as the charm, beauty, and top quarks un-

dergo a flavor-changing weak decays, which can give rise to structure (leptons, sub-jets) within the jet. Furthermore, due to the relative strength of the strong interaction compared that of the electroweak, collision events involving only strong interactions are produced at rates many orders of magnitudes larger than that of electroweak interactions. This makes life difficult for physicists studying the electroweak force at hadron colliders. Sections 2.7, and Chapters 3 and 5 will discuss the techniques used to identify and remove QCD events from the data at different stages of the analysis.

§1.2 Beyond the Standard Model

^{?(sec:BSM)?} The Standard model is one of the most successful theories of the natural world ever created. The predictions of the SM have been tested to many orders of magnitude and no experiment to date⁶ has found a result statistically incompatible with the Standard Model. However, there is a general consensus in the physics community that the Standard Model is not complete. It is believed that it is only an effective theory that is valid below some energy scale Λ . Above this energy, there must exist some other “new physics,” which unifies the forces of the Standard Model and correctly describes the natural world at all scales, while maintaining equivalence to the Standard Model at low energy. This concept is analogous to the relationship between the effective Fermi contact theory of Section 1.1.2 and the unified electroweak theory of Section 1.1.5. The size of the cutoff scale Λ is estimated [10] to be $\mathcal{O}(10^{15})$ GeV for a unified theory with $SU(5)$ symmetry and even larger, $\mathcal{O}(10^{19})$ GeV = M_{planck} if the theory is unified with gravity.

There are many compelling reasons that indicate that the Standard Model is incomplete. One is the fact that the model does not include gravity, which has still not been successfully reformulated into a quantum mechanical theory. Another is that cosmological observations indicate the presences of massive amounts of “dark matter” in the universe. Dark matter is expected to be composed of a stable massive neutral particle which interacts very weakly with other matter; no Standard Model particle fits this description. Finally, there is the “hierarchy,” or fine-tuning problem. This problem strongly affects the Higgs sector,

⁶The Standard Model predicts that lepton number is a good quantum number and that the neutrinos are massless. It has recently been found that the neutrinos do have non-zero mass, and that they undergo oscillations between different neutrino species, violating lepton number.

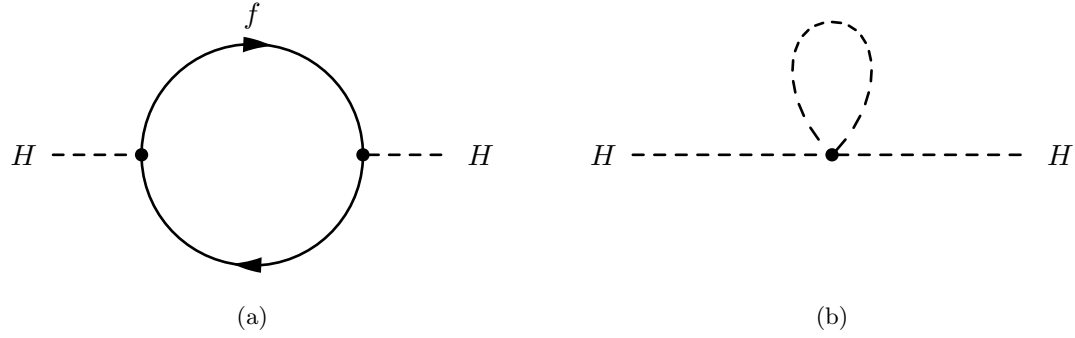


Figure 1.4: Feynman diagram of fermion (a) and scalar (b) loop corrections to Higgs mass.

and motivated the development of Supersymmetry, which are the targets of the search presented in this thesis. An short overview of the hierarchy problem and Supersymmetry are presented in the next sections.

§1.2.1 The Hierarchy Problem

The enormous size of the cutoff scale Λ in the Standard Model causes a major theoretical problem in the Standard Model. During renormalization of the Standard Model, amplitudes with divergent integrals are cut off at Λ . These large constant terms are “absorbed” into the physical observables. The cutoff term appears directly in quantum corrections to the Higgs mass [15]. The Yukawa term $-\lambda_f H \bar{f} f$ coupling the fermion f to the Higgs H produces loop corrections to Higgs mass. The two types of corrections due to fermion loops and scalar loops are illustrated in Figure 1.4. The contribution of the loop correction in Figure 1.4(a) is [15]

$$m_H^2 = -\frac{|\lambda_f|^2}{8\pi^2} \Lambda^2 + \dots, \quad (1.45) \quad \text{eq:HiggsMassCor}$$

scales with Λ^2 , which is many orders of magnitude larger than the electroweak (M_W) scale. The physical mass of the Higgs is expected to have the same scale as M_W , $O(100) \text{ GeV}/c^2$. The fact that each fermion contributes a loop correction (Equation 1.45) requires that the “bare mass” of the Higgs to be tuned to the precision of $(M_W/\Lambda)^2 \approx 10^{-26}$ for the renormalized mass to be correct! This is the so-called fine-tuning problem: it is believed that in a natural theory there will be only one scale. The electroweak unification analogy is in Equation 1.14, where it was noticed that the difference between the QED and weak scale was due to the massive M_W propagator term, and that the fundamental scale g of the

intermediate weak boson theory was compatible with QED. The most promising solution to the hierarchy problem is the introduction of a new, “super” symmetry.

§1.2.2 Supersymmetry

Supersymmetry extends the Standard Model by positing that there exists a symmetry between the integer-spin bosons (γ, W^\pm, Z, H) and the half integer-spin fermions (quarks and leptons). In Supersymmetry, every particle in the Standard Model has a “superpartner” with a spin differs by $1/2$. All of the other quantum numbers (including mass) of the superpartners are the same. The introduction of this symmetry immediately solves the hierarchy problem. For every scalar loop correction (Figure 1.4(b)) to the Higgs mass there is now a corresponding fermion loop correction (Figure 1.4(a)). As the fermion and the scalar have the same quantum numbers (except for spin) it turns out that these two diagrams have the same value, but *opposite* sign. Thus the large Λ^2 superpartner loop corrections to the Higgs mass exactly cancel out the problematic Standard Model corrections. It is clear that if Supersymmetry exists, it must be broken. We have not observed a scalar charged particle with the same mass as the electron, for example. An excellent overview of possible mechanism that create spontaneous symmetry breaking in supersymmetric models is given in Chapter 6 of [15].

§1.2.3 The Minimal Supersymmetric Model

⟨sec:MSSMAndTaus⟩

The simplest possible Supersymmetric extension to the Standard Model is the Minimal Supersymmetric Model (MSSM). The model groups superpartner pairs into chiral (a left or right-handed fermion field plus a complex scalar field) and gauge (a spin-1 vector boson and a left or right-handed *gaugino* fermion) “supermultiplets.” As the weak interactions of the Standard Model fermions are chiral, they (and their superpartners) must belong in a chiral supermultiplet. It is interesting to note that there is a different superpartner for the left and right-handed components of the fermions, even though the superpartners are spin-0 and cannot have any handedness. It is found that there must be two Higgs supermultiplets for the MSSM to be viable. As there are now fermionic particles in the Higgs sector (the Higgsinos), if only one supermultiplet is introduced the MSSM suffers from non-renormalizable gauge

Names		spin 0	spin 1/2	$SU(3)_C, SU(2)_L, U(1)_Y$
squarks, quarks ($\times 3$ families)	Q	$(\tilde{u}_L \ \tilde{d}_L)$	$(u_L \ d_L)$	$(\mathbf{3}, \mathbf{2}, \frac{1}{6})$
	\bar{u}	\tilde{u}_R^*	u_R^\dagger	$(\bar{\mathbf{3}}, \mathbf{1}, -\frac{2}{3})$
	\bar{d}	\tilde{d}_R^*	d_R^\dagger	$(\bar{\mathbf{3}}, \mathbf{1}, \frac{1}{3})$
sleptons, leptons ($\times 3$ families)	L	$(\tilde{\nu} \ \tilde{e}_L)$	$(\nu \ e_L)$	$(\mathbf{1}, \mathbf{2}, -\frac{1}{2})$
	\bar{e}	\tilde{e}_R^*	e_R^\dagger	$(\mathbf{1}, \mathbf{1}, 1)$
Higgs, higgsinos	H_u	$(H_u^+ \ H_u^0)$	$(\tilde{H}_u^+ \ \tilde{H}_u^0)$	$(\mathbf{1}, \mathbf{2}, +\frac{1}{2})$
	H_d	$(H_d^0 \ H_d^-)$	$(\tilde{H}_d^0 \ \tilde{H}_d^-)$	$(\mathbf{1}, \mathbf{2}, -\frac{1}{2})$

Table 1.1: Chiral supermultiplets in the Minimal Supersymmetric Standard Model. The spin-0 fields are complex scalars, and the spin-1/2 fields are left-handed two-component Weyl fermions. Source: [15]

(tab:chiral)

Names	spin 1/2	spin 1	$SU(3)_C, SU(2)_L, U(1)_Y$
gluino, gluon	\tilde{g}	g	$(\mathbf{8}, \mathbf{1}, 0)$
winos, W bosons	$\tilde{W}^\pm \ \tilde{W}^0$	$W^\pm \ W^0$	$(\mathbf{1}, \mathbf{3}, 0)$
bino, B boson	\tilde{B}^0	B^0	$(\mathbf{1}, \mathbf{1}, 0)$

Table 1.2: Gauge supermultiplets in the Minimal Supersymmetric Standard Model. Source: [15]

(tab:gauge)

anomalies.⁷ By introducing an additional Higgs supermultiplet with opposite hypercharge, the anomaly is canceled. The scalar portion of the MSSM Higgs sector then contains two complex doublet fields $H_u = (H_u^+, H_u^0)$ (up-type) and $H_d = (H_d^0, H_d^-)$ (down-type). The complete chiral and gauge supermultiplets of the MSSM are enumerated in Tables 1.1 and 1.2, respectively.

The superpotential (like the scalar potential of Section 1.1.3 but invariant under supersymmetric transformations) of the MSSM is then [15]

$$W_{\text{MSSM}} = \bar{u}_Y \mathbf{y}_u Q H_u - \bar{d}_Y \mathbf{y}_d Q H_d - \bar{e}_Y \mathbf{y}_e L H_d + \mu H_u H_d, \quad (1.46) \{?\}$$

where $H_u, H_d, Q, L, \bar{u}, \bar{d}, \bar{e}$ are the superfields defined in Table 1.1. The \mathbf{y} terms are Yukawa 3×3 matrices which act on the different families. It is important to note that the up-type quarks couple to the up-type Higgs H_u , while the down-type quarks and leptons couple

⁷A gauge anomaly is a linear divergence that occurs in diagrams containing a fermion loop with three gauge bosons (total) in the initial and final states. In the Electroweak model, the sum of the fermion contributions cancel the anomaly. Interestingly, the requirement of anomaly cancellation is only achieved in the SM is achieved only by requiring there be three types of color in QCD.

to the down-type Higgs. This feature has large phenomenological consequences, which are discussed in 1.3.2. The scalar portion of the W_{MSSM} potential defines the spontaneous symmetry breaking. Similar to the scalar potential V symmetry breaking of Section 1.1.3, the potential of V at the minimum is found⁸ to be

$$V = (|\mu|^2 + m_{H_u}^2)|H_u^0|^2 + (|\mu|^2 + m_{H_d}^2)|H_d^0|^2 - (bH_u^0 H_d^0 + c.c.) + \frac{1}{8}(g^2 + g'^2)(|H_u^0|^2 - |H_d^0|^2)^2. \quad (1.47) \quad \text{eq:MSSMScalarP}$$

Under suitable choices⁹ of the parameters in Equation 1.47, the up-type and down-type neutral Higgs fields acquire a VEV, ν_u and ν_d , respectively. The VEVs are related to the VEV of electroweak symmetry breaking (Equation 1.41) in the SM,

$$\nu_u^2 + \nu_d^2 = \nu^2 = \frac{2M_Z^2}{g^2 + g'^2} \approx (174 \text{ GeV})^2.$$

The ratio of the VEVs is expressed as

$$\tan \beta \equiv \frac{\nu_u}{\nu_d},$$

which is an important parameter of the MSSM. As there are two complex doublets, there are a total of eight degrees of freedom in the MSSM Higgs sector. After the symmetry breaking, three of the degrees of freedom are (like the Standard Model) eaten by the W^\pm and Z weak gauge bosons. The remaining five degrees of freedom create five massive Higgs bosons: two CP-even neutral scalars h^0 and H^0 , a CP-odd neutral scalar A^0 , and two (positive and negative) charged scalars H^\pm . The masses of the different Higgs mass eigenstates are related to each other and $\tan \beta$ at tree level by

$$m_{h^0}^2 = \frac{1}{2}(m_{A^0}^2 + m_Z^2 - \sqrt{(m_{A^0}^2 - m_Z^2)^2 + 4m_Z^2 m_{A^0}^2 \sin^2(2\beta)}) \quad (1.48) \quad \text{eq:MSSMLittleH}$$

$$m_{H^0}^2 = \frac{1}{2}(m_{A^0}^2 + m_Z^2 + \sqrt{(m_{A^0}^2 - m_Z^2)^2 + 4m_Z^2 m_{A^0}^2 \sin^2(2\beta)}). \quad (1.49) \quad \text{?eq:MSSMHiggs0}$$

It can be seen that the tree level mass m_{h^0} of Equation 1.48 is bounded from above by $m_{h^0} < m_Z |\cos(2\beta)| < 90 \text{ GeV}/c^2$. If this is true the model would have been excluded by LEP (see next section). However, there are important quantum corrections to m_{h^0} from the top-quark and top-squark loop diagrams which increase m_{h^0} . The Yukawa couplings in the MSSM depend on $\tan \beta$. The relationships for the most massive members of each family are

$$m_t = y_t v \sin \beta, \quad m_b = y_b v \cos \beta, \quad m_\tau = y_\tau v \cos \beta. \quad (1.50) \quad \text{?eq:YukawaTanB}$$

⁸A clever choice of the $SU(2)_L$ gauge has removed any contributions from the charged fields. The charged Higgs fields cannot have a VEV without breaking $U(1)_{em}$.

⁹See Chapter 7 of [15] for a detailed overview.

478 The Yukawa couplings are free parameters determined by experimentally observed masses.
 479 This means that when $\tan\beta$ is large ($\beta \rightarrow \pi$), the Yukawa terms y for the b quarks and τ
 480 leptons must be enhanced to maintain the observed masses. The effect of $\tan\beta$ on the Higgs
 481 mass spectrum and couplings in the MSSM will be discussed further in Section 1.3.2.

482 §1.3 Searches for the Higgs boson

?(sec:PreviousSearches)?
 483 The potential discovery of the Higgs boson is one of the biggest prizes in science today.
 484 Dozens of experiments, thousands of scientists and billions of dollars (a human hierarchy
 485 problem. . .) have been spent in efforts to discovery the Higgs. In this section we discuss how
 486 the Higgs and MSSM) could appear in modern colliders (with an emphasis on the LHC)
 487 and current the limits placed on the Higgs by the LEP and Tevatron experiments.

488 §1.3.1 Standard Model Higgs boson phenomenology

⟨sec:SMHiggsPhenom⟩
 The phenomenology of the Higgs boson is strongly coupled to its relationship with mass. The
 coupling of the Higgs to the fermions is determined by the Yukawa terms (Equation 1.35) in
 the Lagrangian. Taking the electron as an example, after symmetry breaking, the Yukawa
 term is found to be

$$\mathcal{L}_e = -\frac{G_e}{\sqrt{2}}(\nu + H(x))\bar{e}e = -\frac{G_e\nu}{\sqrt{2}}\bar{e}e - \frac{G_e}{\sqrt{2}}H(x)\bar{e}e. \quad (1.51) \quad \boxed{\text{eq:ElectronYukawa}}$$

The value of G_e is a free parameter of the theory and is thus determined by the measurement
 of the electron mass and ν , the VEV of the Higgs field

$$\frac{G_e\nu}{\sqrt{2}} = \frac{m_e}{\nu}. \quad (1.52) \quad \boxed{\text{eq:HiggsVEVtoC}}$$

489 The left-hand side of Equation 1.52 is the same as the constant in the electron–Higgs $H(x)\bar{e}e$
 490 coupling term in Equation 1.51. Therefore the coupling between the fermions and Higgs
 491 boson is proportional to their mass! This remarkable fact shapes the possible production
 492 modes and the branching fractions of Higgs decays.

493 The dominant modes of Higgs boson production depend on the type of experiment.
 494 In general, Higgs production is favored through high-mass intermediate states, due to the
 495 mass-proportional coupling. At the Tevatron and LEP experiments, which will be intro-
 496 duced in the next section, the dominant SM Higgs production mode is “Higgstrahlung,”

⟨fig:HiggsStrahlung⟩

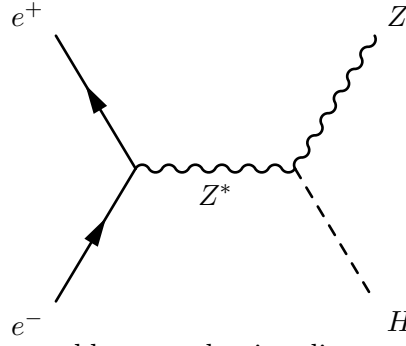
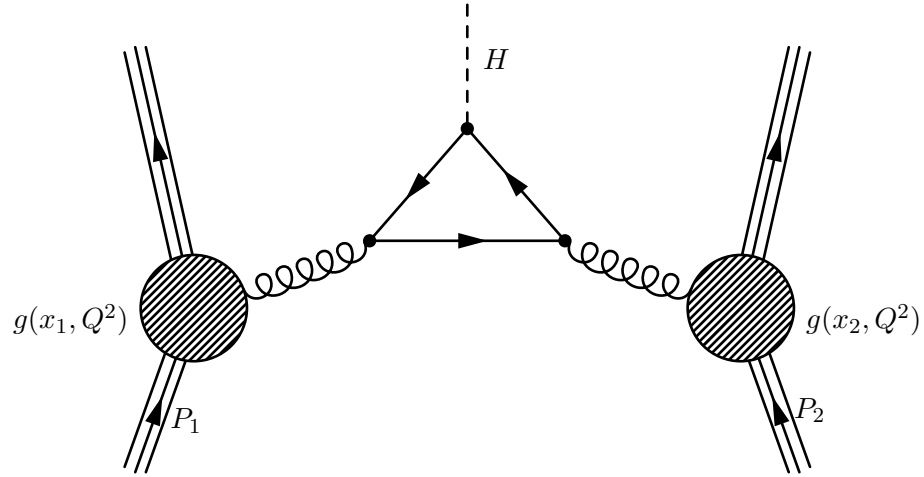
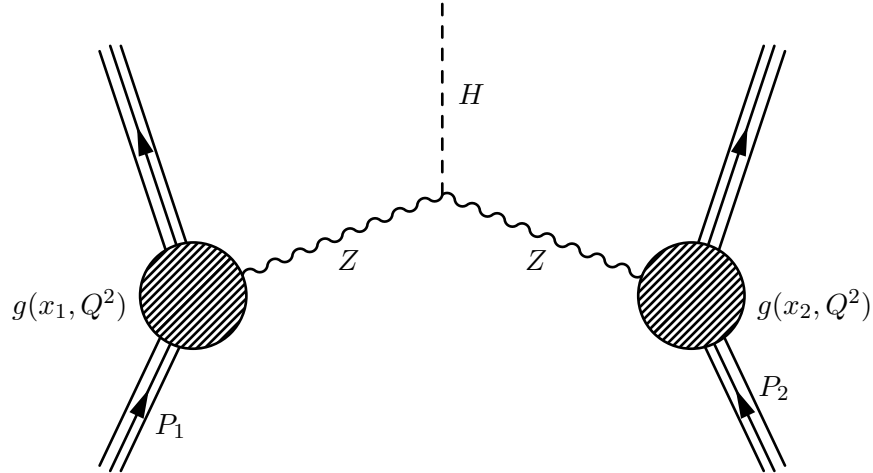


Figure 1.5: Higgstrahlung production diagram at e^+e^- colliders



⟨fig:GluonFusion⟩

Figure 1.6: Gluon fusion Higgs production mechanism in a proton–proton collision. The Higgs mass coupling favors heavy quarks in the central loop. Image credit: [16]



⟨fig:VBFProdDiagram⟩

Figure 1.7: Vector boson fusion (VBF) Higgs production mechanism in proton–proton collisions. The VBF mechanism is notable for the lack of color–flow between the two incident protons.

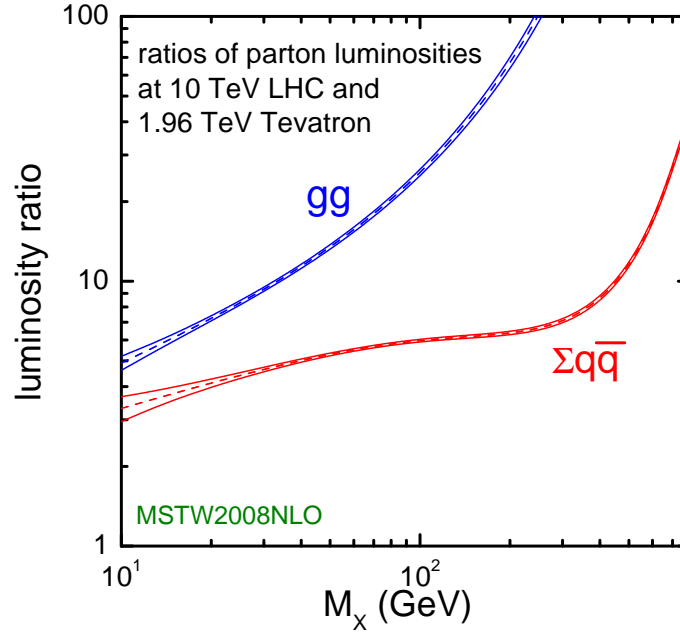


Figure 1.8: Ratio of the parton luminosity (the amount of luminosity contributed by the different species that compose the proton) of the LHC (at $\sqrt{s} = 10$ TeV) and the Tevatron. The large increase in gluon–gluon luminosity affects the favored production mechanisms of the Higgs boson.

(fig:GluonLumiRatio)

where a virtual W^\pm or Z gauge boson is produced and then radiates a Higgs boson. Higgsstrahlung is illustrated in Figure 1.3.1. At the Large Hadron Collider, higher gluon luminosities (See Figure 1.8) result in the favored cross section being “gluon fusion,” (illustrated in Figure 1.3.1) where two gluons from the incident protons combine in a quark (dominated by the massive top quark) loop which then radiates a Higgs boson. Another important channel [17] is “vector boson fusion,” (Figure 1.3.1) where weak gauge bosons (W^\pm or Z) are radiated from the incoming quarks and fuse to produce a Higgs. This is a notable channel due to the lack of “color–flow” (gluons) between the two protons, producing an event with low central jet activity and two “tag–jets” in the forward and backward regions. The theoretical cross sections for the SM Higgs at the LHC are shown in Figure 1.9.

The branching fractions of the different decay modes of the SM Higgs boson depend strongly on the mass of the Higgs boson. In general, the Higgs prefers (due to the Yukawa couplings) to decay pairs of the particles with the highest mass possible. Below the threshold to decay to pairs of weak bosons ($M_H < 160 \text{ GeV}/c^2$), the Higgs decays predominantly to either b –quarks ($b\bar{b}$, 90%) or a pair of τ leptons ($\tau^+\tau^-$, ≈ 10). Above the $W^\pm W^\mp$ threshold,

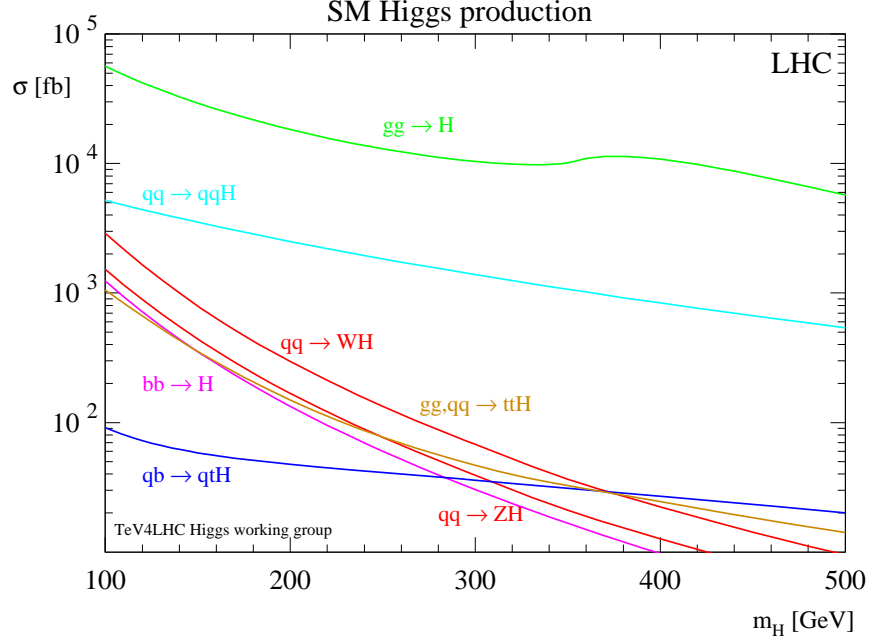


Figure 1.9: Cross section of the Standard Model Higgs boson versus the Higgs boson mass. The different curves give the contribution to the cross section from different production mechanisms. Source: [18].

(fig:LHC SM Higgs Xsec)

512 decays to vector bosons ($H \rightarrow W^\pm W^\mp$ and $H \rightarrow ZZ$) dominate. The dependence of
 513 branching fraction on M_H and the other rare decay modes are illustrated in Figure 1.10. For
 514 low mass Higgs, the $\tau^+\tau^-$ decay mode plays a particularly important role. The dominant
 515 decay mode $H \rightarrow b\bar{b}$, suffers from enormous backgrounds from QCD jet production. It
 516 is important to understand the magnitude of difference between expected Higgs boson
 517 production and the rates of various backgrounds. Figure 1.11 illustrates the cross sections
 518 for different SM processes at hadron colliders. The rate of Higgs production is many orders
 519 of magnitude ($\mathcal{O}(10^{-7})$) smaller than that of QCD production. It is important to therefore
 520 design searches to use handles that can reject the vast majority of the uninteresting events
 521 at hadron colliders.

522 §1.3.2 MSSM Higgs Phenomenology

(sec:MSSM Higgs Phenom)
 523 The phenomenology of the Higgs sector of the MSSM is similar to the Standard Model in
 524 some respects, but differs in some key aspects which have important implications for final
 525 states involving τ leptons and b quarks. When the parameter $\tan\beta$ is large, the coupling

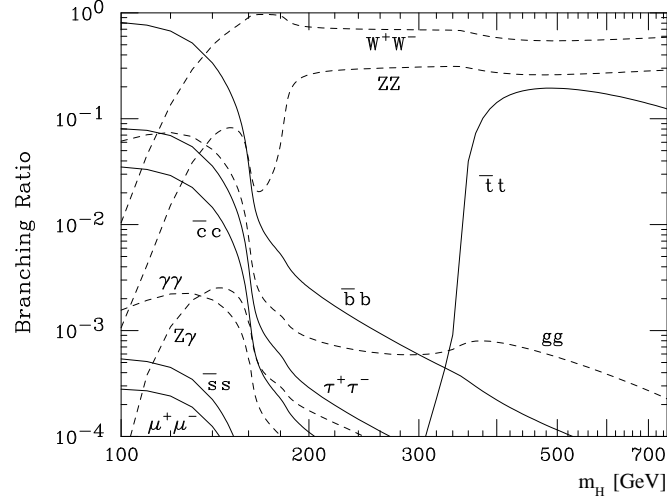


Figure 1.10: Branching fraction of the Standard Model Higgs bosons for different values of M_H . Source: [18].

(fig:SMHiggsBR)

factor between the Higgs and the down-type quarks and leptons (effectively the τ and b quark) is enhanced by $\tan \beta$. The gluon-gluon cross section is therefore increased by $\tan^2 \beta$, where the top quark loop in Figure 1.3.1 is replaced by a ($\tan \beta$ enhanced) b quark loop. Additionally, MSSM Higgs production with associated b -quarks, illustrated in Figure 1.3.2, becomes an important production mode. At tree-level, the MSSM can be defined by the mass of the CP-odd Higgs m_{A^0} and $\tan \beta$. For a reasonably high $\tan \beta$, there is always one CP-even Higgs (h^0 or H^0) which is mass-degenerate with the A^0 . When $\tan \beta$ and m_{A^0} are both large, associated b production dominates the total cross section [20]. The cross sections of the different MSSM neutral Higgs bosons are shown in Figure 1.13. The $\tan \beta$ enhancement of the MSSM Higgs coupling to the b quarks and τ leptons cause the branching fraction of all neutral MSSM Higgs to be $H \rightarrow b\bar{b}$ (90%) and $H \rightarrow \tau^+\tau^-$ (10%) across the entire range of m_{A^0} . The enhanced production rate and the high branching fraction to τ leptons make the MSSM Higgs decaying to τ leptons an exciting and promising channel to search for Higgses and Supersymmetric physics at colliders.

§1.3.3 Results from LEP and Tevatron

The LEP and Tevatron experiments have both set limits on the existence of the Standard Model and MSSM Higgs. Additionally, precision electroweak measurements give additional hints on the prospects for both models.

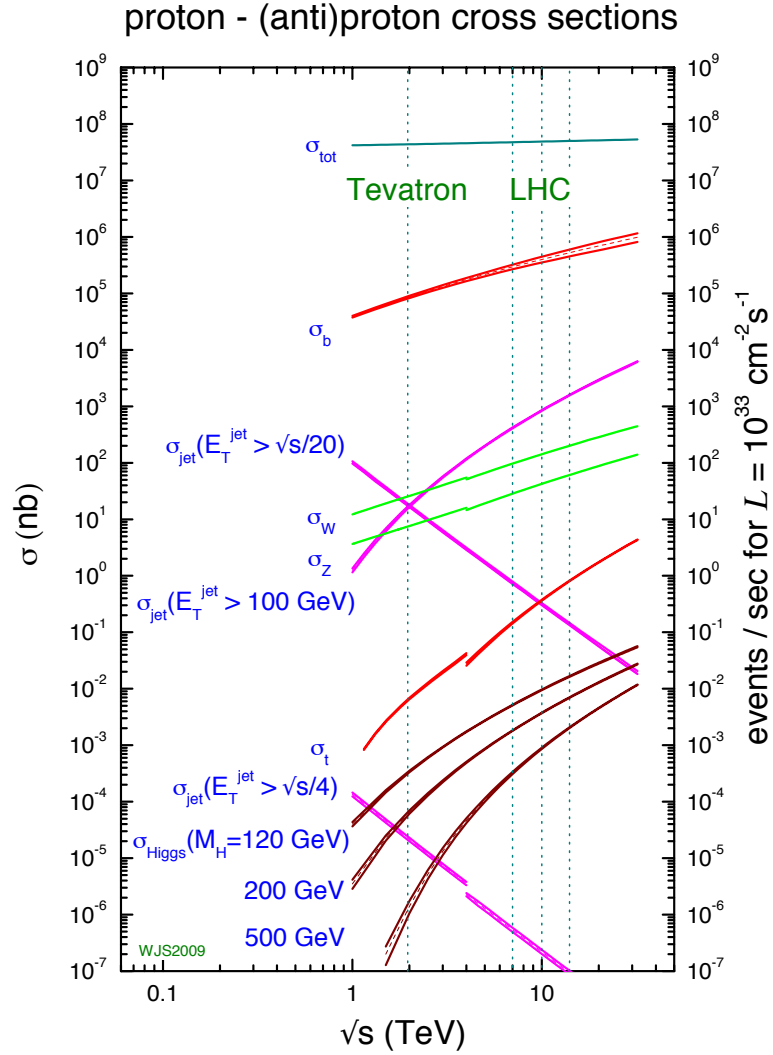
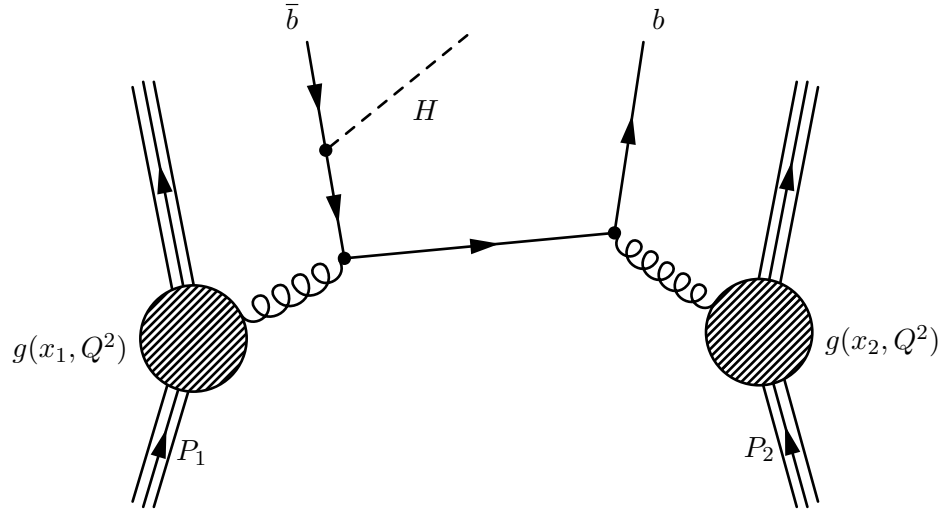


Figure 1.11: Cross sections of various processes at hadron colliders. The horizontal axis represents the center of mass energy of the collision. Of note is the vast difference in scales between Higgs production (maroon lines, $\mathcal{O}(10^{-2})$ nb) and the QCD cross section to produce $b\bar{b}$ pairs (red line, $\mathcal{O}(10^4)$ nb). Source: [19].



g:AssociatedBProduction)

Figure 1.12: One possible diagram for an MSSM Higgs produced with associated b -quarks in a proton–proton collision.

Higgs Decay	Z Decay
$b\bar{b}$	$q\bar{q}$
$\tau^+\tau^-$	$q\bar{q}$
$b\bar{b}$	$t\bar{t}$
$b\bar{b}$	$\nu\bar{\nu}$
$b\bar{b}$	$\mu^+\mu^-$
$b\bar{b}$	e^+e^-

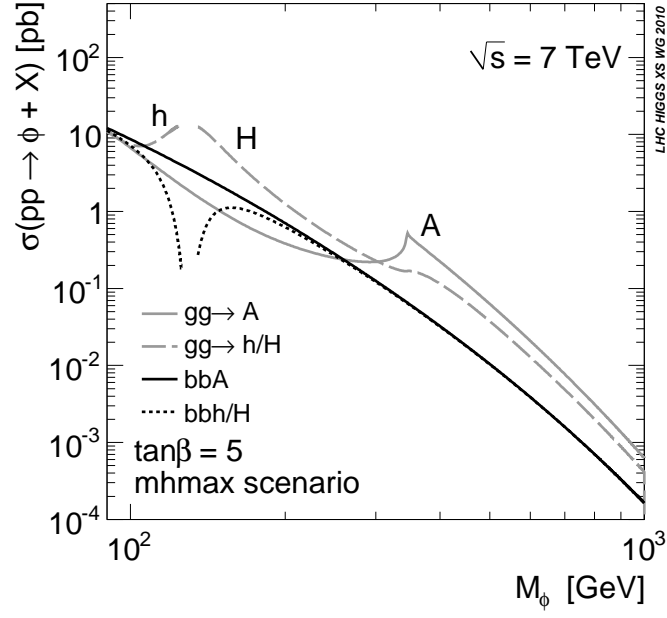
(tab:LEPModes)

Table 1.3: Different channels used at LEP to search for Higgs bosons produced with the Higgstrahlung mechanism.

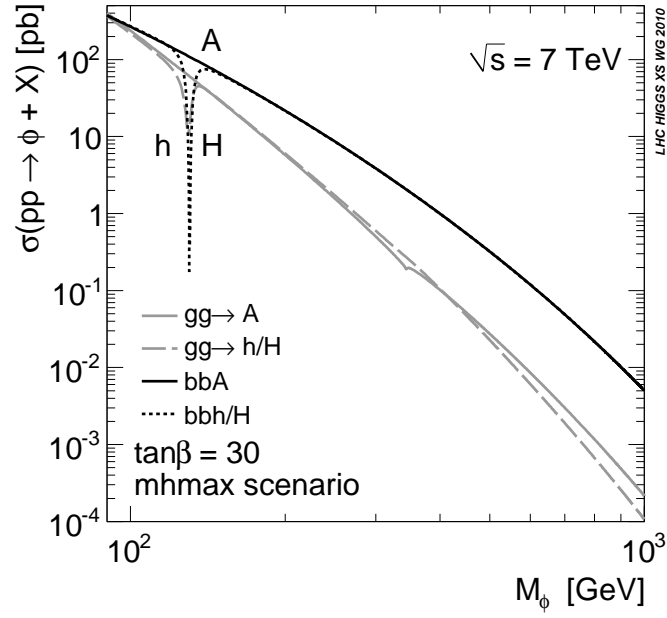
544 LEP was an e^+e^- collider at CERN and has effectively excluded the presence of a
 545 low (less than 114 GeV/c) mass Higgs boson. The dominant SM Higgs production mode
 546 at LEP is Higgstrahlung, where the Higgs is produced in association with a Z boson (see
 547 Figure 1.3.1). The search at LEP utilized a number of different decay channels [18]. The
 548 decay channels used in the LEP search are summarized in Table 1.3.3.

549 The results using all channels from the four LEP experiments¹⁰ have been combined into
 550 a single limit, shown in Figure 1.14. The analysis sets a limit on the ratio $\xi^2 = (g_{HZZ}/g_{HZZ})^2$,
 551 the total HZZ yield divided by the Standard Model. For Higgs masses below 114 GeV/c^2 ,

¹⁰ALEPH, DELPHI, L3, and OPAL



(a)



(b)

Figure 1.13: Cross sections for the different MSSM Higgs bosons versus m_{A^0} in the $m_{h^{max}}$ benchmark scenario [21] scenario for $\tan\beta = 5$ (a) and $\tan\beta = 30$ (b). Source: [20]

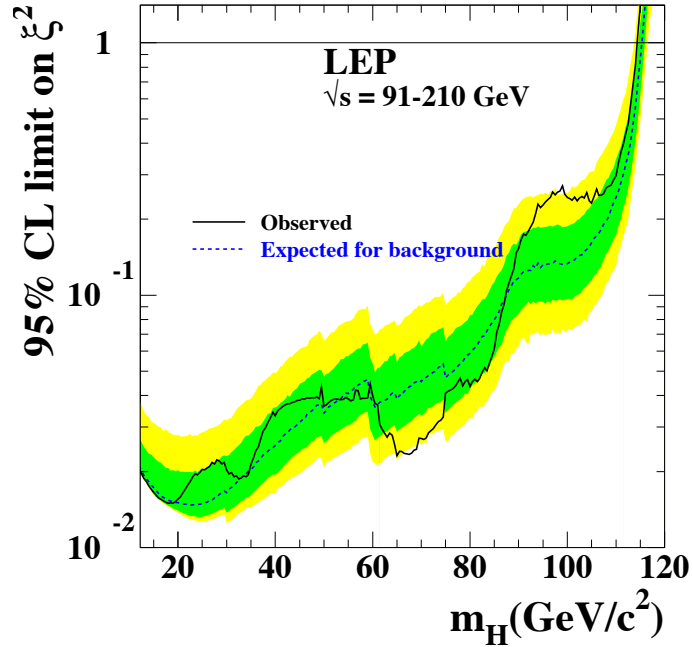


Figure 1.14: Combined LEP upper limit set on the quantity $\xi^2 = (g_{HZZ}/g_{HZZ})^2$ at 95% confidence level. Regions where the observed ratio is less than one exclude the Standard Model. The dashed line gives the expected limit for the null (background only) hypothesis, with the green and yellow bands representing the expected variance at one and two sigma, respectively, of the limit. The solid line is the observed limit from the combined LEP data. Reference: [18]

(fig:LEPHiggsLimit)

the ratio is below unity at the 95% confidence level, ruling out a Standard Model Higgs below that mass.

The Tevatron is a proton–antiproton collider with a center-of-mass energy of $\sqrt{s} = 1.96$ TeV. There are two general purpose detectors at the Tevatron, CDF and DØ. The dominant Higgs production modes at the Tevatron are Higgstrahlung and gluon fusion (see Figure 1.3.1). For low mass ($m_H < 135$ GeV/c²) Higgs bosons the dominant channel at the Tevatron is the Higgstrahlung production mode and $H \rightarrow b\bar{b}$ decays. Large multi-jet backgrounds prevent the $H \rightarrow b\bar{b}$ decay mode from being useful for searching for Higgs bosons produced by gluon fusion. The $H \rightarrow \tau^+\tau^-$ and $H \rightarrow \gamma\gamma$ decays are additionally used in an inclusive search at low mass, but do not dominate the search sensitivity. The combined low-mass limit on the Standard Model Higgs from both Tevatron experiments is shown in Figure 1.15. The Tevatron currently sets an upper limit on the SM Higgs cross

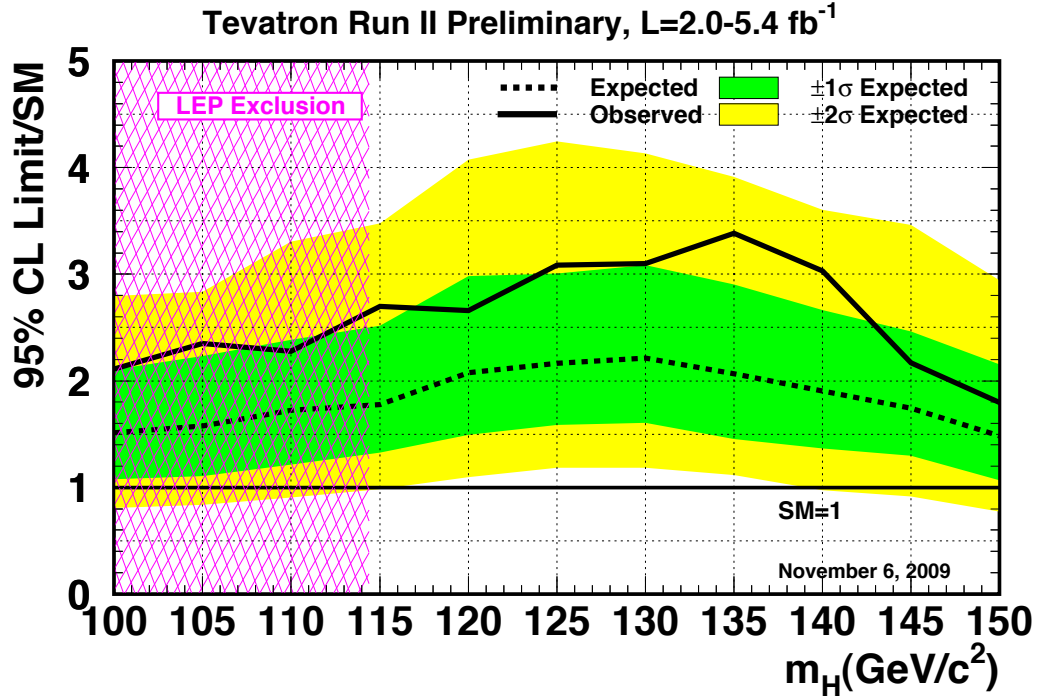


Figure 1.15: Combined CDF and DØ RunII upper limit on the cross section of a Standard Model-like Higgs boson. The LEP limit is shown in pink. Reference: [18]

section of about 2.5 times the Standard Model expectation.

When ($m_H < 135 \text{ GeV}/c^2$) the $H \rightarrow W^+W^-$ decay becomes significant. Low di-boson backgrounds allow this decay mode to probe both Higgstrahlung and gluon fusion production modes.

§1.4 The Physics of the Tau Lepton

As discussed in sections 1.3.1 and 1.2.3, the τ lepton is an important probe of Higgs physics. The τ lepton has some unusual properties which make it particularly challenging at hadron colliders. With a mass of $1.78 \text{ GeV}/c^2$, the τ lepton is heaviest of the leptons. The nominal decay distance $c\tau$ of the τ lepton is $87 \text{ } \mu\text{m}$, which in practice means that the τ will always decay before reaching the first layer of the detector. Tau decays can be effectively classified into two types. “Leptonic” decays consist of a τ decaying to a light lepton ($\ell = e, \mu$) and two neutrinos $\tau^+ \rightarrow \ell^+ \nu_\tau \bar{\nu}_\ell$. “Hadronic” decays consist of a low-multiplicity collimated group of hadrons, typically π^\pm and π^0 mesons. The hadronic decays of the τ lepton compose approx-

Visible Decay Products	Resonance	Mass (MeV/ c^2)	Fraction [18]
Leptonic modes			
$e^- \nu_\tau \bar{\nu}_e$	-	0.5	17.8%
$\mu^- \nu_\tau \bar{\nu}_\mu$	-	105	17.4%
Hadronic modes			
$\pi^- \nu_\tau$	-	135	10.9%
$\pi^- \pi^0 \nu_\tau$	ρ	770	25.5%
$\pi^- \pi^0 \pi^0 \nu_\tau$	$a1$	1200	9.3%
$\pi^- \pi^- \pi^+ \nu_\tau$	$a1$	1200	9.0%
$\pi^- \pi^- \pi^+ \pi^0 \nu_\tau$	$a1$	1200	4.5%
Total			94.4%

<tab:decay'modes>

Table 1.4: Resonances and branching ratios of the dominant decay modes of the τ lepton. The decay products listed correspond to a negatively charged τ lepton; the table is identical under charge conjugation.

577 imately 65% of the τ lepton branching fraction, with the remainder shared approximately
578 equally by the leptonic decays. The branching fractions for the leptonic and most common
579 hadronic decays are shown in table ??.

Chapter 2

The Compact Muon Solenoid Experiment

?⟨ch:detector⟩?

The Compact Muon Solenoid (CMS) Experiment is a “general purpose” particle detector designed to measure collision events at the Large Hadron Collider (LHC), a proton–proton synchrotron located at the CERN laboratory in Geneva, Switzerland. The design goals of the CMS experiment are [22], in order of priority:

- Good muon identification and momentum resolution over a wide range of momenta and angles, good dimuon mass resolution ($\approx 1\%$ at $100 \text{ GeV}/c^2$), and the ability to determine unambiguously the charge of muons with $p < 1 \text{ TeV}/c$;
- Good charged-particle momentum resolution and reconstruction efficiency in the inner tracker. Efficient triggering and offline tagging of τ ’s and b –jets, requiring pixel detectors close to the interaction region;
- Good electromagnetic energy resolution, good diphoton and dielectron mass resolution ($\approx 1\%$ at $100 \text{ GeV}/c^2$), wide geometric coverage, π^0 rejection, and efficient photon and lepton isolation at high luminosities;
- Good missing–transverse–energy and dijet–mass resolution, requiring hadron calorimeters with a large hermetic geometric coverage and with fine lateral segmentation.

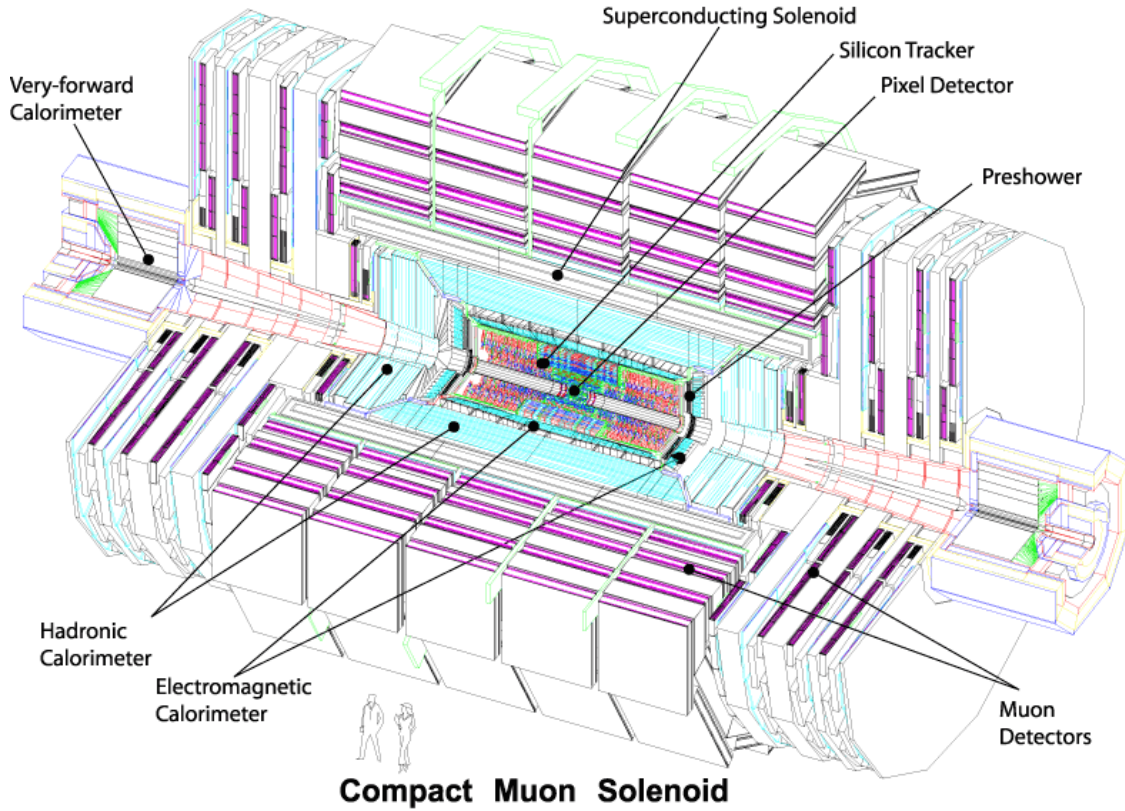
The detector uses a hermetic design that maximizes the solid–angle of the fiducial region to capture as much information about the collisions as possible. The general geometry of the detector is cylindrical. A cutaway diagram of the detector is shown in Figure 2.1. Each of the sub–detector components consists of “barrel” and “endcap” components. As its name suggests, the detector is centered around a four Tesla superconducting solenoid magnet. The individual sub–detectors of CMS are arranged in a manner that permits identification

of different species of particles. The central (closest to interaction point) sub-detectors are the charged particle tracking systems (the “tracker”). The tracker is designed to be a *non-destructive* instrument, which means that ideally that the momentum of particles are unchanged after passing through it. Outside of the tracker is the electromagnetic and hadronic calorimeters, which are abbreviated ECAL and HCAL, respectively. The calorimeter is a *destructive* detector, and is designed such that visible incident particles are completely absorbed. The outer layers of CMS are designed to measure muons, the one¹ species of particle that is immune to the effects of the calorimeter. The arrangement of destructive and non-destructive sub-detectors facilitates the identification of different types of particles. This concept is illustrated in Figure 2.1(b). In this chapter we give an brief overview of the LHC machine, and then describe the individual sub-detector systems of CMS.

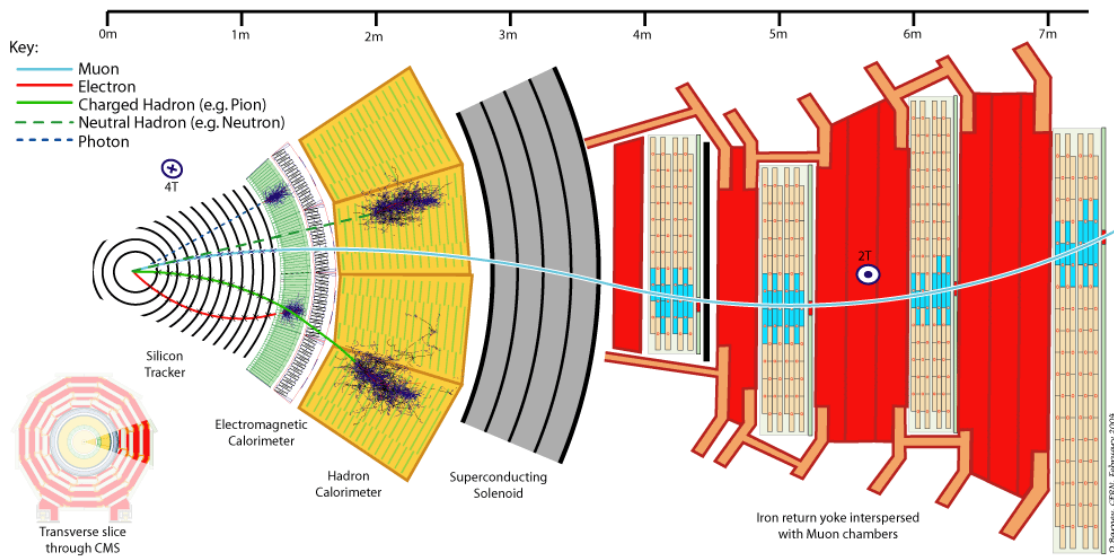
§2.1 The Large Hadron Collider

The Large Hadron Collider is a proton–proton synchrotron, with a design collision energy of 14 TeV. At the time of this writing (and for the foreseeable future), the LHC is the world’s largest and highest energy particle accelerator. A synchrotron is a machine that accelerates beams of charged particles by using magnets to steer them in a circle through radio–frequency resonating cavities which accelerate the particles. As the LHC is a collider, there are two beams that are accelerated in opposite directions. The maximum beam energy of a synchrotron is determined by its radius and the maximum strength of the magnetic fields used to bend the path of the beam. The dipole magnets used by the LHC to steer the particles are superconducting niobium–titanium. To maintain them in a superconducting state, they are cooled using superfluid liquid helium to 1.9 Kelvin. To store the beam at the injection energy of 450 GeV, the magnetic dipole fields must be maintained at 1/2 Tesla. As the energy of each beam energy is increased to its (design) maximum of 7 TeV, the dipole fields are ramped to a maximum field of over 8 Tesla.

¹Neutrinos of course fulfill this requirement as well, but are so weakly interacting that they are effectively invisible.



(a)



(b)

Figure 2.1: Figure (a), top, shows a schematic drawing of the CMS detector. The individual sub-detectors are labeled. Two humans are shown in the foreground for scale. Figure (b) shows a radial cross section of the detector and demonstrates how the (non-)destructiveness of different sub-detectors facilitates particle identification.

<fig:AllCMSCutaways>

§2.2 Solenoid Magnet

The four Tesla field of the CMS solenoid magnet is a critical factor in ability of CMS to precisely measure collisions at the LHC. The momentum of charged particles is measured in the detector by examining the curvature of the particles path as it travels through the magnetic field. The radius of curvature r of a charged particle in a magnetic field is given by

$$r = \frac{p_{\perp}}{|q|B}, \quad (2.1) \quad \text{eq:LarmorRadius}$$

where q is the charge of the particle, B is the magnetic field, and p_{\perp} is the component of the particle's relativistic momentum perpendicular to the direction of the magnetic field. From Equation 2.1, it is evident that the ability to measure high momentum charged particles (a critical goal of CMS) requires a high magnetic field. Even at very high particle energies where the resolution becomes poor, the strength of the magnetic field is still very important for identifying the bending direction of the particle; the direction corresponds to the particle's electric charge. Furthermore, the homogeneity of the magnetic field is important to minimize systematic errors in the measurement of tracks.

The CMS solenoid is extremely large. The radial bore of the magnet is 6.3 meters; the magnet is 12.5 meters in length and weighs 220 tons. The large bore of the magnet allows the tracker and calorimeter systems to be located inside the solenoid. The internal windings of solenoid is arranged in four layers to increase the total field strength and are cooled by liquid helium to a temperature of 4.5 Kelvin. The windings are magnetically coupled to the support superstructure. This coupling allows the magnetic to heat uniformly during a “quench²” event, reducing localized stresses. The nominal current at full field of the solenoid is 19.14 kA. The solenoid itself is surrounded by an iron return yoke with a total mass of 10,000 tons. The return yoke surrounding the solenoid minimizes the fringing field. The muon detector system is interspersed inside the yoke, and takes advantage of the field in the yoke to measure the momentum and charge of muons.

²A quench event occurs when some part of the magnet is suddenly no longer in a superconducting state. The coil becomes resistive and the large current in the magnet creates large amounts of heat.

§2.3 Charged Particle Tracking Systems

The charged particle tracking system measures the trajectories of charged particles emerging from the event. The tracker measures the trajectory of a charged particle by measuring “hits” along the trajectory. Each hit corresponds to the global position of the trajectory on a given surface. The trajectory can then be reconstructed by a helix to the points. The tracker is designed to have a resolution that permits the reconstruction of “secondary vertices” in b -quark and τ lepton decays. To accomplish this, there are two types of tracking detectors in CMS. The “pixel detector” composes the inner layers (three in the barrel, two in the endcaps). The pixel detector is situated as close as possible (4.4 cm) to the interaction point and has a very high resolution. Outside of the pixel detector is the silicon strip tracker, with ten layers in the barrel and 12 layers in the endcaps. A secondary vertex occurs when a particle is semi-stable, traveling some non-negligible distance in the detector, but decaying before the first layer of the tracking system. The pixel and strip tracking detectors have a fiducial region which extends to a pseudorapidity of approximately $|\eta| \approx 2.5$.

Both the pixel and strip trackers are silicon based. The principle of operation is similar to that of a charged-coupled discharge (CCD) in a modern digital camera. The sensitive portion of the detector is a silicon chip that is arranged with diode junctions formed by a p -doped layer and an n -doped layer³. Each $p - n$ junction is electrically isolated from adjacent layers. The size of each junction region determines⁴ the spatial resolution of the sensor. In the pixel detector, each sensor region “pixel” is $100 \times 150 \mu\text{m}^2$. In the strip tracker, The rear side of the chip is mounted to read-out electronics. During operation, a high-voltage reverse bias is applied to each $p - n$ junction to achieve full depletion. When a charged particle passes through the detector, the diode-junction breaks down and the readout system registers the hit.

The tracking system has been specifically designed for the high radiation environment around the interaction point. The detector is cooled to -27°C during operation to minimize

³The pixel detector actually uses a more complicated multi-layered scheme to improve radiation hardness. For details, see Section 3.2.2 of [22].

⁴Additionally, the size of the sensitive area needs to be small enough such that the hit occupancy during a typically LHC event is not too large, which would cause overlaps and spoil the ability to reconstruct tracks. The expected occupancy depends on the distance r^2 from the interaction. The expected occupancy in the pixel detector for LHC collisions is 10^{-4} .

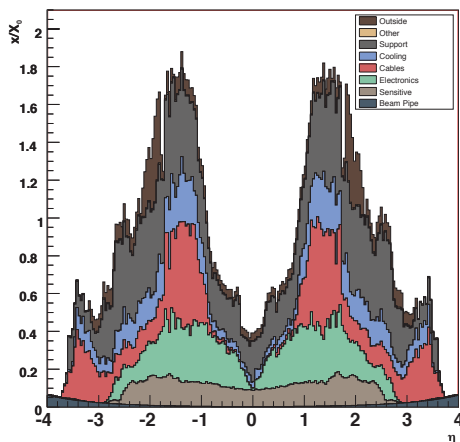


Figure 2.2: Material budget of the CMS tracker in units of radiation lengths X_0 . The material budget is broken down into the contributions from the different components of the tracker. The amount of material is largest in the “transition region” between the barrel and endcap.

ig:TrackerMaterialBudget)

674 damage. Radiation exposure produced in LHC collisions can change behavior of the tracking
 675 detector in three ways. Over time, radiation can induce positive holes in oxide layers found
 676 in the read-out electronics which increase the signal-to-noise ratio. In the sensor mass itself,
 677 radiation damage changes the doping from n to p over time. The required voltage to deplete
 678 the sensor will thus increase over time. The readout electronics, bias voltage supplies, and
 679 cooling systems are designed to scale with the radiation damage and maintain a signal-to-
 680 noise ratio of 10:1 or greater for 10 years of LHC operation. The final radiation effect is not
 681 an integrating effect. A “single event upset” is transient effect where an ionizing charged
 682 particle passes through the readout electronics and changes the state of the digital circuitry.

683 In the ideal case, the tracker would be a non-destructive instrument. However, charged
 684 particles can interact with the mass of the tracker (and its support infrastructure). These
 685 interactions limit the resolution of the tracker. The amount of matter in the tracker is
 686 referred to as the “material budget”. The material budget of the CMS tracker depends
 687 heavily on the pseudorapidity η and is illustrated in Figure 2.2. The relatively large material
 688 budget of the CMS tracker has two effects: charged particles can “multiple scattering,”
 689 interacting with material in the tracker. This can cause “kinks” in the reconstructed track.
 690 Hadronic particles (charged and neutral) can undergo “nuclear interactions,” which are

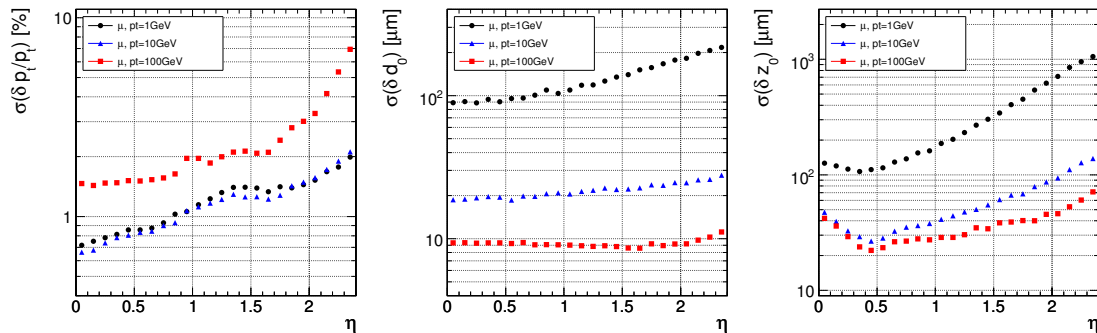


Figure 2.3: Expected resolutions of reconstructed transverse momentum (left), transverse impact parameter (center), and longitudinal impact parameter (right) versus absolute pseudorapidity $|\eta|$. The resolution is shown for three different cases of particle p_T , 1 GeV/c (black), 10 GeV/c (blue), and 100 GeV/c (red).

(fig:ExpectedTrackerRes)

a hard collisions between the incident particle and the tracker material. This typically produces a spray of hadrons from the point of interaction. Finally, the material budget can cause “photon conversions.” A photon conversion occurs when a photon (which typically does not interact with the tracker) converts into an electron–positron pair while passing through matter in the tracker.

The expected (from simulation) impact parameter and transverse momentum resolution of the tracker is shown in Figure 2.3. The momentum scale of the tracker has been measured [23] in 7 TeV 2010 CMS data using $J/\psi \rightarrow \mu^+\mu^-$ decays and is found to agree within 5% with the prediction from simulation. The impact parameter and vertex resolutions have also been measured [24] in data and found to be in excellent agreement with the simulation.

§2.4 Electromagnetic Calorimeter

The electromagnetic calorimeter (ECAL) of CMS is designed to measure the energy of particles which interact electromagnetically with high precision.⁵ The ECAL is a *scintillation* detector, and functions by counting the number of photons produced in an electromagnetic shower inside a crystal. Upon entering the crystal, a charged particle or photon will interact electromagnetically with the crystal, producing a shower of electrons and photons. The

⁵One of the design goals of the CMS experiment is to be able to conduct a search for Standard Higgs bosons decaying to pairs of photons. The branching fraction to photons is illustrated in Figure 1.10.

708 shower will expand until it consists entirely of photons. The crystal is optically clear, so
 709 these photons travel to the rear face of the crystal where they are then counted by a pho-
 710 tomultiplier. The number of detected photons can then be related to the energy that was
 711 deposited in the crystal. At 18°C, about 4.5 photoelectrons will be produced per MeV of de-
 712 posited energy. The ECAL has excellent solid angle coverage, extending to a pseudorapidity
 713 of $|\eta| = 3.0$.

714 The ECAL uses lead tungstate (PbWO_4) crystals as the scintillation medium. The
 715 crystals have a very large density, which allows the calorimeter to be relatively compact.
 716 To be able to correctly measure the energy of electrons and photons, an incident photon or
 717 electron must be completely stopped by interactions with the calorimeter. The quantities
 718 that determine if an electron or photon will be completely contained is the total depth of
 719 the crystal, the crystal density, and the radiation length property X_0 of the crystal. The
 720 radiation length X_0 is defined as the mean distance (normalized to material density) after
 721 which an electron will have lost $(1 - \frac{1}{e})$ of its energy. The PbWO_4 crystals of the CMS
 722 ECAL have a density of 8.28 g/cm² and a depth of 230 mm. A single crystal thus has a
 723 total radiation length of 25.8 X_0 , and will capture on average 99.9993% of the energy of an
 724 incident electron. The front face of the crystal is 22 mm \times 22 mm, which corresponds to an
 725 $\eta - \phi$ area of 0.00174×0.00174 . The Molière radius of a material is the average radial profile
 726 size of an electromagnetic shower, and for PbWO_4 is 2.2 cm. The fact that the Molière
 727 radius is larger than the size of the individual crystals improves the spatial resolution of
 728 the measurement. As the shower is shared between multiple crystals, the relative amounts
 729 deposited in each crystal allows the true impact point to be determined with a resolution
 730 smaller than the individual crystal size.

731 The transparency of the CMS ECAL crystals change as they are exposed to radia-
 732 tion. However, at the working temperature of the ECAL (18°C), the crystal transparency
 733 will naturally return to its nominal value. The transparency of the crystals thus decreases
 734 during the course of a run of collisions, then increases during the following period collision-
 735 less period. The changing transparency conditions need to be continuously monitored and
 736 corrected for to ensure a stable detector response. The transparency of the crystals are
 737 measured continuously using two lasers. One laser has wavelength $\lambda = 400$ nm which cor-

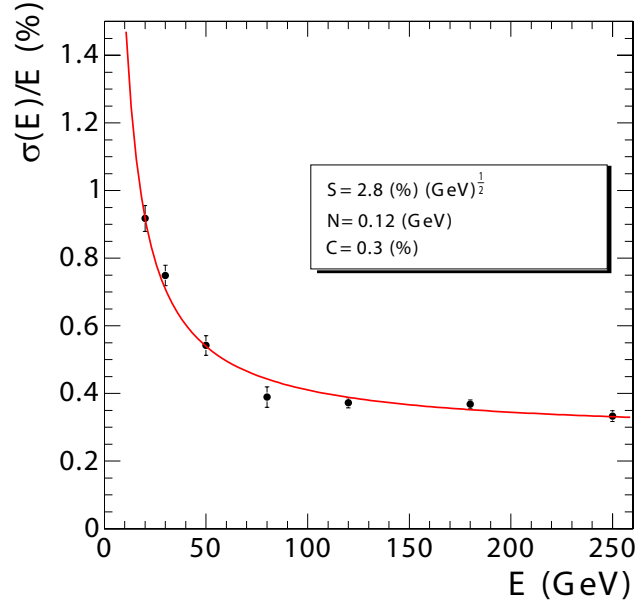


Figure 2.4: Energy resolution (in %) of the CMS ECAL measured at an electron test beam. The resolution depends on the incident energy of the electron. The points are fitted to function with the form given in Equation 2.2. The fitted parameters are given in the legend.

(fig:ECALResolution)

738 responds to the color of light produced in the scintillations and is sensitive to changes in
 739 transparency. The other laser is in the near-infrared and is used to monitor the overall
 740 stability of the crystal. The lasers synchronized to pulse between LHC bunch trains so the
 741 transparency can be continuously monitored while collisions are occurring.

The energy resolution of the ECAL is given by

$$\left(\frac{\sigma}{E}\right)^2 = \left(\frac{S}{\sqrt{E}}\right)^2 + \left(\frac{N}{E}\right)^2 + C^2, \quad (2.2) \quad \text{eq:ECALResolut}$$

742 where S is a stochastic noise term (due to photon counting statistics), N is a noise term, and
 743 C is a constant term. The parameters of Equation 2.2 have been measured at an electron
 744 test-beam (see Figure 2.4). The energy resolution is better than 1% for electron energies
 745 greater than 20 GeV.

746 §2.5 Hadronic Calorimeter

?(sec:HCAL)?
 747 The hadronic calorimeter (HCAL) surrounds the CMS ECAL and is located within the coil
 748 of the CMS solenoid magnet. To ensure incident particles are completely contained within
 749 the calorimeter volume, in the barrel region the HCAL employs a “tail-catcher”, an extra

750 layer of calorimetry outside of the magnet. The hadronic calorimeter measures the energy
 751 of charged and neutral hadronic particles. The HCAL is a *sampling* calorimeter. Layers of
 752 plastic scintillating tiles are interspersed between brass absorber plates. An incident hadron
 753 produces a hadronic shower as it passes through the absorber. The particles in the shower
 754 produce light as they pass through the scintillating tiles. Measuring the light produced in
 755 each layer of tile allows the reconstruction of the radial profile of the shower which can be
 756 related to the deposited energy. The response of the scintillator tiles are calibrated using a
 757 radioactive source, either Cs^{137} or Co^{60} . Small stainless tubes permit the radioactive sources
 758 to be moved into the center of the tile during calibration. The granularity of the HCAL is
 759 0.087×0.087 and 0.17×0.17 in $\eta - \phi$ in the barrel ($|\eta| < 1.6$) and endcap ($|\eta| > 1.6$),
 760 respectively.

761 The outer HCAL (HO), or “tail catcher” is designed to capture showers which begin
 762 late in the ECAL or HCAL and ensure they do not create spurious signals in the muon
 763 system (“punch through”). The HO is installed outside of the solenoid magnet in the first
 764 layer between the first to layers of the iron return yoke. The total depth of the HCAL,
 765 including the HO is then 11.8 interaction lengths.

766 The HCAL includes a specially designed forward calorimeter (HF). The design of the
 767 forward calorimeter is constrained by the extreme amount of radiation it is exposed to,
 768 particularly at the highest rapidities. The active material of the HF are quartz fibers. The
 769 fibers are installed inside grooves inside of a steel absorber. Charged particles created in
 770 showers in the absorber create light in the fibers, provided they have energy greater than
 771 the with energy greater than the Cherenkov threshold. As Cherenkov light is created by
 772 the passage of charged particles through matter, the HF design is not sensitive to neutrons
 773 emitted by radionucleids that may be created in the absorber material durin operation.
 774 The fibers are grouped into two sets: one set of fibers are installed over the full depth of
 775 the detector, the other only cover half the depth. A crude form of particle identification
 776 is possible, as showers created by electrons and photons will deposit the majority of the
 777 energy in the front of the detector.

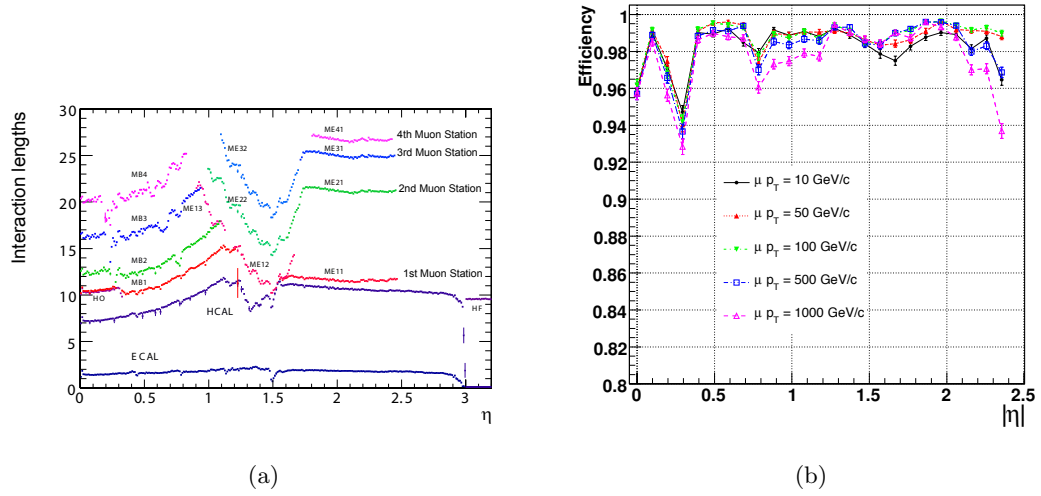


Figure 2.5: The left figure, (a), illustrates the number of interaction lengths versus pseudorapidity η of material that must be traversed before reaching the different layers of the muon system. On the right, (b) shows the efficiency versus η to reconstruct a “global” muon for different transverse momenta.

§2.6 Muon System

The ability to detect and measure muons is one of the most valuable tools an experimentalist has at a hadron collider experiment. Muons have particular properties that cause them to leave extremely signatures in the detectors.

- Muons are stable particles, for the typical energies and distances considered at a collider.
- Muons have non-zero charge, so their trajectories can be measured.
- Muons are heavy enough that they are “minimum ionizing particles,” in that they lose much less energy as they pass through material.

The approach to detecting muons is to build the detector to a thickness that typical particles (electrons, photons, hadrons) will not penetrate the outermost calorimeter. Any charged particle that is detected outside of this region can be identified as a muon. At CMS, the muon detection systems are built into the magnet return yoke outside of the CMS calorimeters and magnet, giving them excellent protection (illustrated in Figure 2.5(a)) against hadronic “punch-through.” The purity of particles that reach the muon system make it especially

effective as a “trigger” of interesting physics. The CMS muon system has the feature that it additionally can trigger on the transverse momenta of muons. The CMS muon system is composed of three types of detectors: drift tubes (DT), resistive plate chambers (RPC), and cathode strip chambers (CSC).

A drift tube detector is of a tube filled with a mixture of argon (85%) and carbon dioxide (15%) gas with a positively charged ($V = +3.6$ kV) wire running through the middle of the tube. When a charged particle passes through the tube, it ionizes some gas. The free electrons are then drawn to the positively charged wire inside the tube, creating a signal when reach it. The speed of the detector is limited by the “drift time,” the maximum amount of time it may take for an electron to reach sensor wire. The precision of the spatial measurement can be increased by recording the time at which each wire records a signal and correlating the measurements across multiple tubes. The time resolution of the CMS DTs is on the order of a few nanoseconds, allowing the DT to provide a trigger on a given proton bunch crossing. The tubes in adjacent layers are offset by one half tube width to take advantage of this effect and ensure there are no gaps in the fiducial region. In CMS, the smallest unit of the DT system is the superlayer, which consists of four layers of tubes. A DT chamber consists of three or two superlayers. The tubes in the two superlayers farthest from the beam are oriented parallel to the beam and measured the bending of the muons in the magnetic field. The inner superlayer is oriented orthogonally to the beam and measures the longitudinal position of incident muons. There are four muon “stations” in the barrel which contain DT chambers. The stations correspond to available areas in the magnetic return yoke. In the barrel, the muon momentum resolution of the DTs is better than 95%.

Cathode strip chambers (CSCs) are used in the endcap muon system, providing coverage in the pseudorapidity range $0.9 < |\eta| < 2.4$. A cathode strip chamber consists of a chamber filled with inert gas that with a number of internal wires held at a high voltage. A number of cathode strips are installed perpendicular⁶ induced to the wires on the walls of the chamber. When a muon passes through the CSC, it creates ionizes some of the gas. The high voltage on a nearby wire causes this ionized gas to break down, forming a conductive

⁶The wires are actually placed at an angle to the perpendicular to compensate for a shifting effect caused by the magnetic field Lorentz force.

passage in the gas and an “avalanche” current between the wire and a number of the cathode strips. The spatial position of the hit in two dimensions is found taking one coordinate from the wire and the other coordinate from the signal average of the cathode strips.

The CSCs in the CMS endcap are positioned such that a muon in the pseudorapidity range $1.2 < |\eta| < 2.4$ will cross three or four CSC detectors. The geometry of the CSC strips and wires is designed to provide a spatial $r - \phi$ resolution of 2 mm at the L1 trigger level and a final offline reconstruction resolution of 75 μm for the first layer and 150 μm for outer layers. The RMS of the response time for a CSC layer is about 11 ns, which is too long to correctly associate a signal in the CSCs to an LHC bunch crossing (25 ns) with high efficiency. By grouping the layers into chambers, and taking the shortest response, the correct bunch crossing can be identified with 98–99% efficiency.

The Resistive Plate Chamber (RPC) muon detectors ensure that the muon system can be used as a fast, first level trigger. The RPC detector consists of two gaps filled with gas (up and down) with a common set of strips between the two gaps. The strips are oriented parallel to the beam line to permit measurement of the transverse momentum of the muons.

§2.7 Trigger System

(sec:Trigger) At the LHC, proton bunch crossings (collisions) occur every 25 ns. This corresponds to an interaction of 40 MHz. At this high rate, and with the huge number of channels in the CMS detector, the front-end bandwidth readout from the detector is over 1 Pb/s. Due to bandwidth and storage requirements, the rate at which events are permanently recorded must be reduced by more than a factor of a million. This reduction is achieved by CMS trigger system. As only a fraction of the total events can be stored, and the rate of diffractive and common QCD multi-jet production is many orders of magnitude larger than “interesting” new physics (see Figure 1.11). The trigger must therefore be designed to select “interesting” events. A typical requirement applied at the trigger level might be the presence of a high- p_T muon, an isolated ECAL deposit, or a large deposit of energy in the event.

The CMS trigger consists of two stages: a fast Level-1 (L1) trigger and a High-Level Trigger (HLT). The L1 trigger system is built on custom, typically re-programmable elec-

tronics and interfaces directly to the detector subsystems. The L1 trigger has access to information from the muon and calorimeter systems. The L1 does not have access to the full granularity of the muon system and calorimeters but must make the decision based on coarse segments. The design acceptance rate of the L1 trigger is 100 kHz. The trigger typically operates at a nominal rate of 30 kHz. The maximum latency of the L1 is 3.2 μ s, requiring that the output from detector electronics be passed through memory pipelines to ensure that no bunch crossings go unanalyzed. The High-Level trigger runs on a farm of about 1000 commercial compute nodes and processes events that pass that are accepted by the L1 trigger. A High-Level trigger decision (“path”) has the ability to reconstruct tracks and do a full regional unpacking of the recorded hits in a regions of the calorimeter. Each HLT path has a strict rate budget, as the total rate of the HLT is required to be less than 100 Hz. The triggers used at CMS change as the conditions change. To limit the total rate to 100 Hz as the luminosity increases, trigger paths must either increase their thresholds, or apply a “prescale.” When a prescale is applied, a fraction of events passing the trigger are thrown away randomly.

The CMS trigger is a deep subject and a complete description is beyond the scope of this thesis. A detailed description can be found in [25]. The triggers used in the analysis presented in this thesis will be briefly described. Two types of trigger selections were applied to the 2010 datasets used in this analysis. During the initial period of low luminosity running, single muon triggers were used. As the luminosity increased, the p_T threshold of the trigger was increased. In some cases, an “isolated muon” HLT trigger was required, in which a veto was applied on muons with associated energy deposits in the calorimeter. In the final period of data taking, two “cross-triggers” were used. These required the presence of both a muon and a hadronic tau decay in the event. The triggers used in this analysis in the different 2010 run periods are enumerated in Table 5.3.

The muon component of all the triggers used in this analysis is based on the “L1 seed trigger” BLAH. The L1 muon trigger decision is determined by the Global Muon Trigger (GMT), which combines information from the DT, CSC, and RPC sub-detectors, and is able to trigger muons up to a pseudorapidity of $|\eta| < 2.1$. Each sub-detector has a “local trigger,” which can reconstruct tracks in the muon system. For the drift tubes,

FiXme:
what is it?

880 the Bunch Track Identifiers (BTI), a custom integrated circuit, searches for aligned hits in
881 the associated DT chamber. The CSCs and RPCs employ similar strategies to detect local
882 muon tracks. The sub-detectors send the GMT the charge, p_T , η , ϕ , and a quality code of
883 up to four local muons. The measurements from the sub-detectors are combined and a final
884 decision is made by the GMT.

885 §2.8 Particle Flow Reconstruction Algorithm

886 §2.9 DAQ

Chapter 3

Tau Identification: The Tau Neural Classifier

High tau identification performance is important for the discovery potential of many possible new physics signals at the Compact Muon Solenoid (CMS). The Standard Model background rates from true tau leptons are typically the same order of magnitude as the expected signal rate in many searches for new physics. The challenge of doing physics with taus is driven by the rate at which objects are incorrectly tagged as taus. In particular, quark and gluon jets have a significantly higher production cross-section and events where these objects are incorrectly identified as tau leptons can dominate the backgrounds of searches for new physics using taus. Efficient identification of hadronic tau decays and low misidentification rate for quarks and gluons is thus essential to maximize the significance of searches for new physics at CMS.

Tau leptons are unique in that they are the only type of leptons which are heavy enough to decay to hadrons. The hadronic decays compose approximately 65% of all tau decays, the remainder being split nearly evenly between $\tau^- \rightarrow \mu^- \bar{\nu}_\mu \nu_\tau$ and $\tau^- \rightarrow e^- \bar{\nu}_e \nu_\tau$. The hadronic decays are typically composed of one or three charged pions and zero to two neutral pions. The neutral pions decay almost instantaneously to pairs of photons.

In this chapter, we describe a technique to identify hadronic tau decays. Tau decays to electrons and muons are difficult to distinguish from prompt production of electrons and muons in pp collisions. Analyses that use exclusively use the leptonic (e, μ) decays of taus typically require that the decays be of opposite flavor. With the Tau Neural Classifier, we aim to improve the discrimination of true hadronic tau decays from quark and gluon jets using a neural network approach.

§3.1 Geometric Tau Identification Algorithms

(sec:GeometricTauId) The tau identification strategies used in previously published CMS analyses are fully described in [26]. A summary of the basic methods and strategies is given here. There are two primary methods for selecting objects used to reconstruct tau leptons. The CaloTau algorithm uses tracks reconstructed by the tracker and clusters of hits in the electromagnetic and hadronic calorimeter. The other method (PFTau) uses objects reconstructed by the CMS particle flow algorithm, which is described in [27]. The particle flow algorithm provides a global and unique description of every particle (charged hadron, photon, electron, etc.) in the event; measurements from sub-detectors are combined according to their measured resolutions to improve energy and angular resolution and reduce double counting. All of the tau identification strategies described in this thesis use the particle flow objects.

Both methods typically use an “leading object” and an isolation requirement to reject quark and gluon jet background. Quark and gluon jets are less collimated and have a higher constituent multiplicity and softer constituent p_T spectrum than a hadronic tau decay of the same transverse momentum. The “leading track” requirement is applied by requiring a relatively high momentum object near the center of the jet; typically a charged track with transverse momentum greater than 5 GeV/c within $\Delta R < 0.1$ about the center of the jet axis. The isolation requirement exploits the collimation of true taus by defining an isolation annulus about the kinematic center of the jet and requiring no detector activity about a threshold in that annulus. This approach yields a misidentification rate of approximately 1% for QCD backgrounds and a hadronic tau identification efficiency of approximately 50% [26].

§3.2 Decay Mode Tau Identification: Motivation

The tau identification strategy described previously can be extended by looking at the different hadronic decay modes of the tau individually. The dominant hadronic decays of taus consist of a one or three charged π^\pm mesons and up to two π^0 mesons and are enumerated in Table 1.4. The majority of these decays proceed through intermediate resonances and each of these decay modes maps directly to a tau final state multiplicity. Each intermediate resonance has a different invariant mass (see Figure 3.1). This implies that the problem of

939 hadronic tau identification can be re-framed from a global search for collimated hadrons
 940 satisfying the tau mass constraint into a ensemble of searches for single production of the
 941 different hadronic tau decay resonances. The Tau Neural Classifier algorithm implements
 942 this approach using two complimentary techniques: a method to reconstruct the decay mode
 943 and an ensemble of neural network classifiers used to identify each decay mode resonance
 944 and reject quark and gluon jets with the same final state topology.

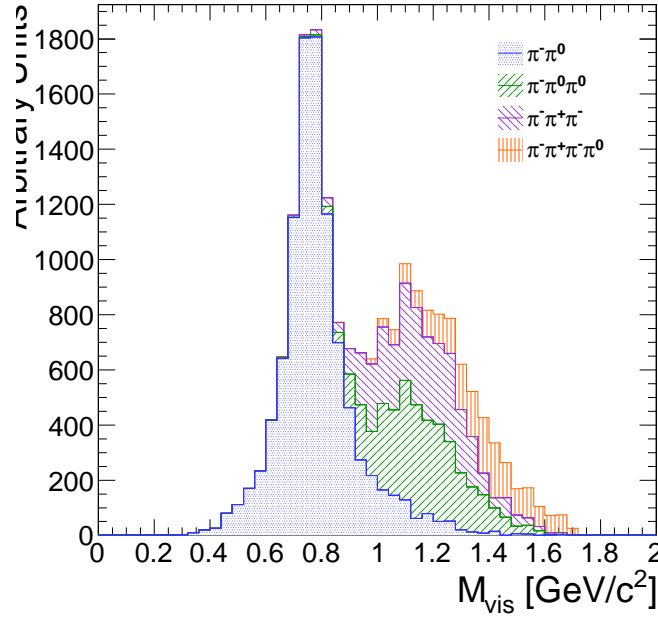


Figure 3.1: The invariant mass of the visible decay products in hadronic tau decays. The decay mode $\tau^- \rightarrow \pi^- \nu_\tau$ is omitted. The different decay modes have different invariant masses corresponding to the intermediate resonance in the decay.

(fig:trueInvMass)

945 §3.3 The Tau Neural Classifier

(sec:Tanc)
 946 The Tau Neural Classifier algorithm reconstructs the decay mode of the tau-candidate and
 947 then feeds the tau-candidate to a discriminator associated to that decay mode to make the
 948 classification decision. Each discriminator therefore maps to a reconstructed decay mode in a
 949 one-to-one fashion. To optimize the discrimination for each of the different decay modes, the
 950 TaNC uses an ensemble of neural nets. Each neural net corresponds to one of the dominant
 951 hadronic decay modes of the tau lepton. These selected hadronic decays constitute 95% of

all hadronic tau decays. Tau-candidates with reconstructed decay modes not in the set of dominant hadronic modes are immediately tagged as background.

§3.3.1 Decay mode reconstruction

The major task in reconstructing the decay mode of the tau is determining the number of π^0 mesons produced in the decay. A π^0 meson decays almost instantaneously to a pair of photons. The photon objects are reconstructed using the particle flow algorithm [27]. The initial collection of photon objects considered to be π^0 candidates are the photons in the signal cone described by using the “shrinking-cone” tau algorithm, described in [26].

The reconstruction of photons from π^0 decays present in the signal cone is complicated by a number of factors. To suppress calorimeter noise and underlying event photons, all photons with minimum transverse energy less than 0.5 GeV are removed from the signal cone, which removes some signal photons. Photons produced in secondary interactions, pile-up events, and electromagnetic showers produced by signal photons that convert to electron-positron pairs can contaminate the signal cone with extra low transverse energy photons. Highly boosted π^0 mesons may decay into a pair of photons with a small opening angle, resulting in two overlapping showers in the ECAL being reconstructed as one photon. The π^0 meson content of the tau-candidate is reconstructed in two stages. First, photon pairs are merged together into candidate π^0 mesons. The remaining un-merged photons are then subject to a quality requirement.

Photon merging

Photons are merged into composite π^0 candidates by examining the invariant mass of all possible pairs of photons in the signal region. Only π^0 candidates (photon pairs) with a composite invariant mass less than 0.2 GeV/c are considered. The combination of the high granularity of the CMS ECAL and the particle flow algorithm provide excellent energy and angular resolution for photons; the π^0 mass peak is readily visible in the invariant mass spectrum of signal photon pairs (see figure 3.3.1). The π^0 candidates that satisfy the invariant mass requirement are ranked by the difference between the composite invariant mass of the photon pair and the invariant mass of the π^0 meson given by the PDG [18]. The

best pairs are then tagged as π^0 mesons, removing lower-ranking candidate π^0 s as necessary to ensure that no photon is included in more than one π^0 meson.

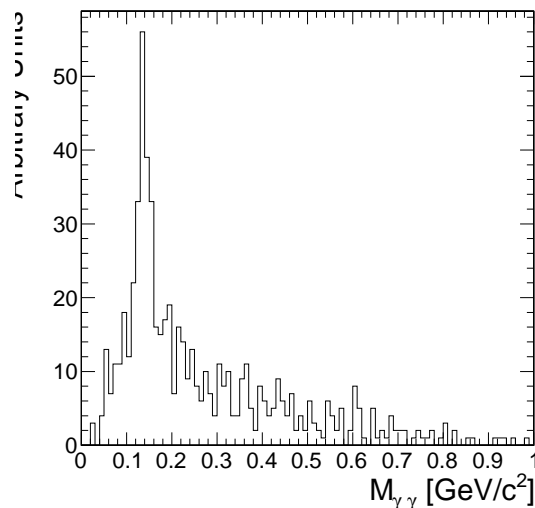


Figure 3.2: Invariant mass of the photon pair for reconstructed tau-candidates with two reconstructed photons in the signal region that are matched to generator level $\tau^- \rightarrow \pi^- \pi^0 \nu_\tau$ decays.

mDiPhotonsForTrueDM1)

Quality requirements

Photons from the underlying event and other reconstruction effects cause the number of reconstructed photons to be greater than the true number of photons expected from a given hadronic tau decay. Photons that have not been merged into a π^0 meson candidate are recursively filtered by requiring that the fraction of the transverse momentum carried by the lowest p_T photon be greater than 10% with respect to the entire (tracks, π^0 candidates, and photons) tau-candidate. In the case that a photon is not merged but meets the minimum momentum fraction requirement, it is considered a π^0 candidate. This requirement removes extraneous photons, while minimizing the removal of single photons that correspond to a true π^0 meson (see 3.3). A mass hypothesis with the nominal [18] value of the π^0 is applied to all π^0 candidates. All objects that fail the filtering requirements are moved to the isolation collection.

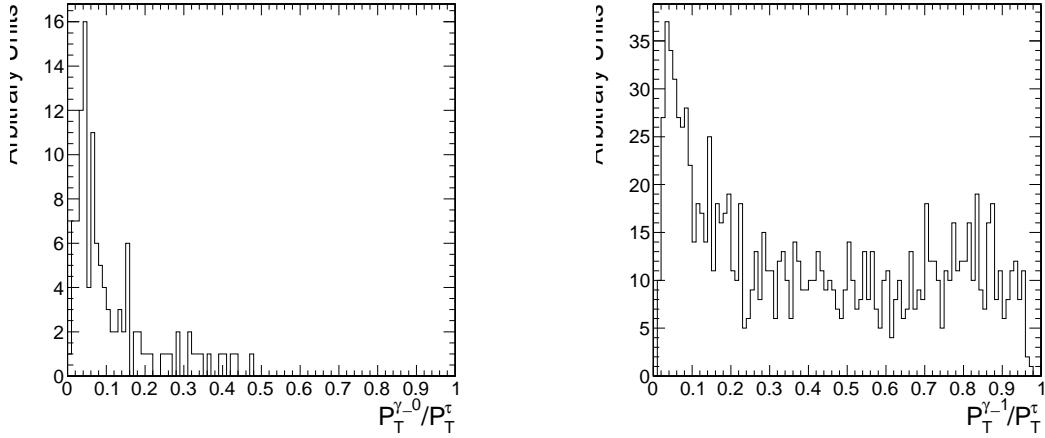


Figure 3.3: Fraction of total τ -candidate transverse momenta carried by the photon for reconstructed taus containing a single photons for two benchmark cases. On the left, the reconstructed tau-candidate is matched to generator level $\tau^- \rightarrow \pi^- \nu_\tau$ decays, for which no photon is expected. On the right, the reconstructed tau-candidate is matched to generator level $\tau^- \rightarrow \pi^- \pi^0 \nu_\tau$ decays and the photon is expected to correspond to a true π^0 meson. The requirement on the p_T fraction of the lowest p_T photon improves the purity of the decay mode reconstruction.

(fig:photonFiltering)

994 Performance

995 The performance of the decay mode reconstruction can be measured for tau-candidates that
 996 are matched to generator level hadronically decaying tau leptons by examining the correla-
 997 tion of the reconstructed decay mode to the true decay mode determined from the Monte
 998 Carlo generator level information. Figure 3.4 compares the decay mode reconstruction per-
 999 formance of a naive approach where the decay mode is determined by simply counting
 1000 the number of photons to the performance of the photon merging and filtering approach
 1001 described in section 3.3.1. The correlation for the merging and filtering algorithm is much
 1002 more diagonal, indicating higher performance. The performance is additionally presented for
 1003 comparison in tabular form in table 3.3.1 (merging and filtering approach) and table 3.3.1
 1004 (naive approach).

1005 The performance of the decay mode reconstruction is dependent on the transverse
 1006 momentum and η of the tau-candidate and is shown in figure 3.5. The p_T dependence
 1007 is largely due to threshold effects; high multiplicity decay modes are suppressed at low
 1008 transverse momentum as the constituents are below the minimum p_T quality requirements.

1009 In the forward region, nuclear interactions and conversions from the increased material
 1010 budget enhances modes containing π^0 mesons.

True decay mode	Reconstructed Decay Mode					
	$\pi^-\nu_\tau$	$\pi^-\pi^0\nu_\tau$	$\pi^-\pi^0\pi^0\nu_\tau$	$\pi^-\pi^+\pi^-\nu_\tau$	$\pi^-\pi^+\pi^-\pi^0\nu_\tau$	Other
$\pi^-\nu_\tau$	14.8%	1.6%	0.4%	0.1%	0.0%	0.7%
$\pi^-\pi^0\nu_\tau$	6.0%	17.1%	9.0%	0.1%	0.1%	5.5%
$\pi^-\pi^0\pi^0\nu_\tau$	0.9%	3.8%	4.2%	0.0%	0.1%	5.9%
$\pi^-\pi^+\pi^-\nu_\tau$	0.8%	0.3%	0.1%	9.7%	1.6%	6.2%
$\pi^-\pi^+\pi^-\pi^0\nu_\tau$	0.1%	0.2%	0.1%	1.7%	2.7%	4.5%

Table 3.1: Decay mode correlation table for the selected dominant decay modes for the naive approach. The percentage in a given row and column indicates the fraction of hadronic tau decays from $Z \rightarrow \tau^+\tau^-$ events that are matched to a generator level decay mode given by the row and are reconstructed with the decay mode given by the column. Entries in the "Other" column are immediately tagged as background.

True decay mode	Reconstructed Decay Mode					
	$\pi^-\nu_\tau$	$\pi^-\pi^0\nu_\tau$	$\pi^-\pi^0\pi^0\nu_\tau$	$\pi^-\pi^+\pi^-\nu_\tau$	$\pi^-\pi^+\pi^-\pi^0\nu_\tau$	Other
$\pi^-\nu_\tau$	16.2%	1.0%	0.1%	0.1%	0.0%	0.3%
$\pi^-\pi^0\nu_\tau$	10.7%	21.4%	3.6%	0.2%	0.1%	1.9%
$\pi^-\pi^0\pi^0\nu_\tau$	1.8%	7.1%	4.4%	0.1%	0.0%	1.5%
$\pi^-\pi^+\pi^-\nu_\tau$	0.9%	0.2%	0.0%	11.5%	0.6%	5.4%
$\pi^-\pi^+\pi^-\pi^0\nu_\tau$	0.1%	0.3%	0.0%	3.2%	2.9%	2.7%

Table 3.2: Decay mode correlation table for the selected dominant decay modes for the merging and filtering approach. The percentage in a given row and column indicates the fraction of hadronic tau decays from $Z \rightarrow \tau^+\tau^-$ events that are matched to a generator level decay mode given by the row and are reconstructed with the decay mode given by the column. Entries in the "Other" column are immediately tagged as background.

1011 §3.3.2 Neural network classification

1012 Neural Network Training

(sec:tanc`nn`training)

1013 The samples used to train the TaNC neural networks are typical of the signals and back-
 1014 grounds found in common physics analyses using taus. The signal-type training sample is

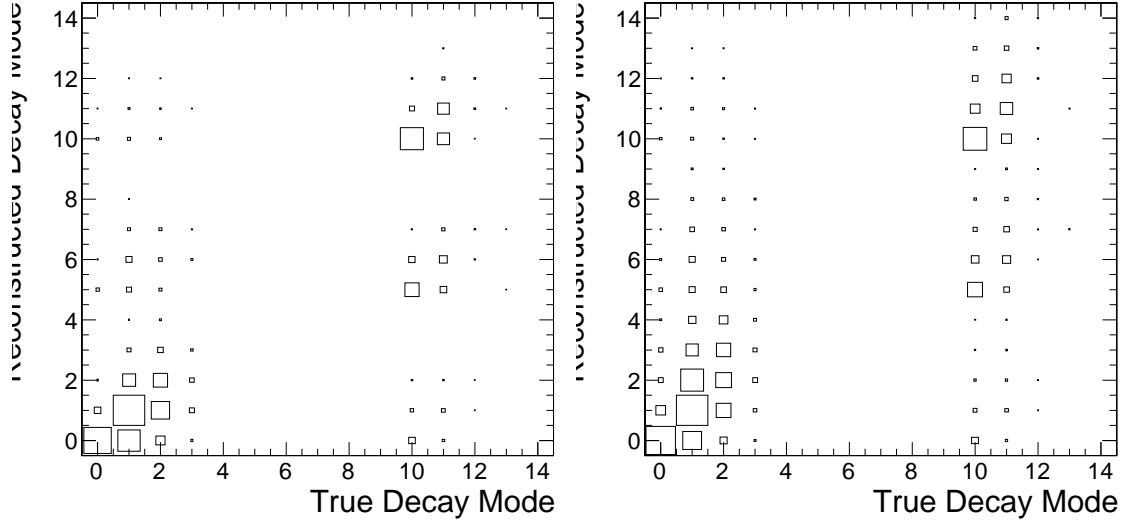


Figure 3.4: Correlations between reconstructed tau decay mode and true tau decay mode for hadronic tau decays in $Z \rightarrow \tau^+\tau^-$ events. The correlation when no photon merging or filtering is applied is shown on the right, and the correlation for the algorithm described in section 3.3.1 is on the left. The horizontal and vertical axis are the decay mode indices of the true and reconstructed decay mode, respectively. The decay mode index N_{DM} is defined as $N_{DM} = (N_{\pi^\pm} - 1) \cdot 5 + N_{\pi^0}$. The area of the box in each cell is proportional to the fraction of tau-candidates that were reconstructed with the decay mode indicated on the vertical axis for the true tau decay on the horizontal axis. The performance of a decay mode reconstruction algorithm can be determined by the spread of the reconstructed number of π^0 mesons about the true number (the diagonal entries) determined from the generator level Monte Carlo information. If the reconstruction was perfect, the correlation would be exactly diagonal.

(fig:dmResolution)

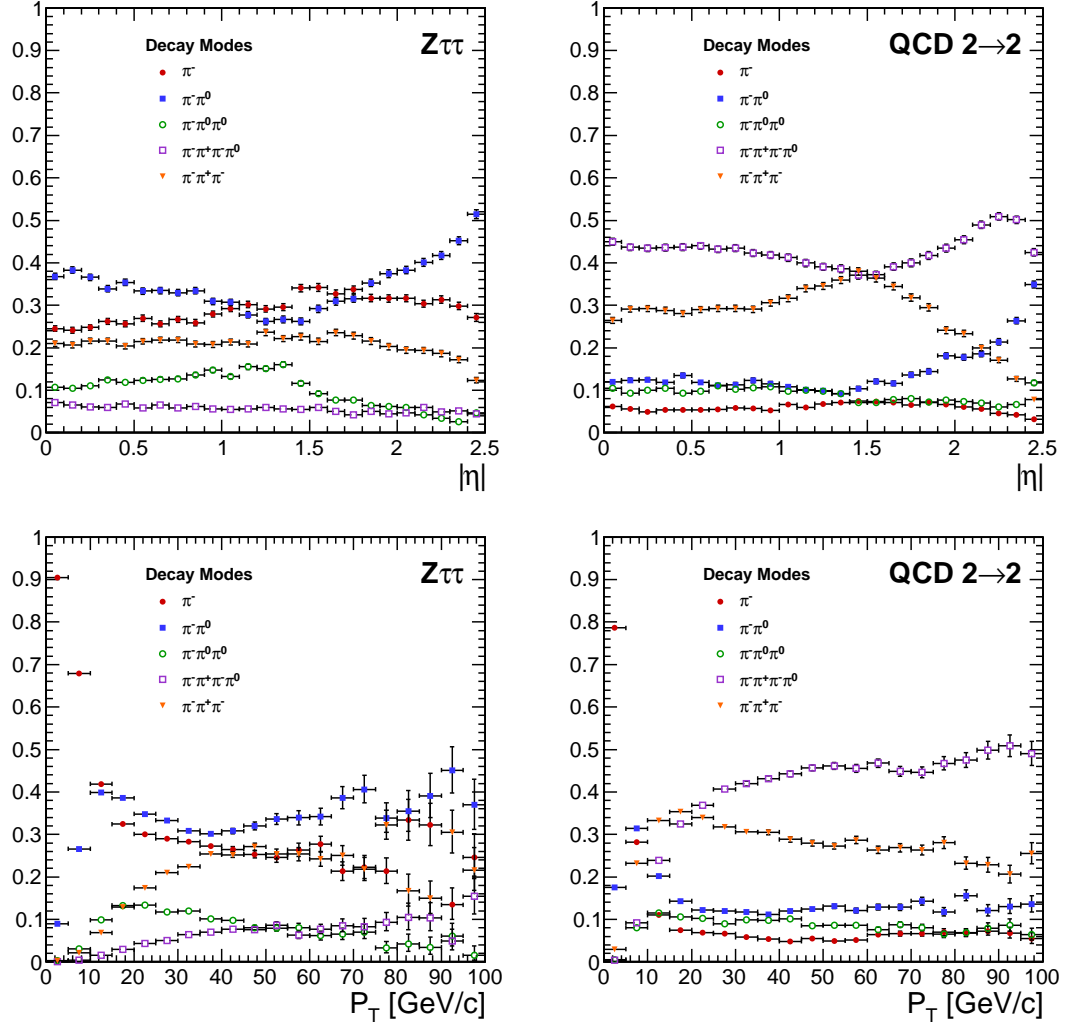


Figure 3.5: Kinematic dependence of reconstructed decay mode for tau-candidates from $Z \rightarrow \tau^+\tau^-$ (left) and QCD di-jets (right) versus transverse momentum (top) and pseudo-rapidity (bottom). Each curve is the probability for a tau-candidate to be reconstructed with the associated decay mode after the leading pion and decay mode preselection has been applied.

(fig:dmKinematics)

1015 composed of reconstructed tau-candidates that are matched to generator level hadronic tau
 1016 decays coming from simulated $Z \rightarrow \tau^+\tau^-$ events. The background training sample consists
 1017 of reconstructed tau-candidates in simulated QCD $2 \rightarrow 2$ hard scattering events. The QCD
 1018 p_T spectrum is steeply falling, and to obtain sufficient statistics across a broad range of p_T
 1019 the sample is split into different \hat{p}_T bins. Each binned QCD sample imposes a generator
 1020 level cut on the transverse momentum of the hard interaction. During the evaluation of
 1021 discrimination performance the QCD samples are weighted according to their respective
 1022 integrated luminosities to remove any effect of the binning.

1023 The signal and background samples are split into five subsamples corresponding to
 1024 each reconstructed decay mode. An additional selection is applied to each subsample by
 1025 requiring a “leading pion”: either a charged hadron or gamma candidate with transverse
 1026 momentum greater than 5 GeV/ c . A large number of QCD training events is required as
 1027 both the leading pion selection and the requirement that the decay mode match one of the
 1028 dominant modes given in table 1.4 are effective discriminants. For each subsample, 80%
 1029 of the signal and background tau-candidates are used for training the neural networks by
 1030 the TMVA software, with half (40%) used as a validation sample used to ensure the neural
 1031 network is not over-trained. The number of signal and background entries used for training
 1032 and validation in each decay mode subsample is given in table 3.3.2.

1033 The remaining 20% of the signal and background samples are reserved as a statistically
 1034 independent sample to evaluate the performance of the neural nets after the training is
 1035 completed. The TaNC uses the “MLP” neural network implementation provided by the
 1036 TMVA software package, described in [28]. The “MLP” classifier is a feed-forward artificial
 1037 neural network. There are two layers of hidden nodes and a single node in the output layer.
 1038 The hyperbolic tangent function is used for the neuron activation function.

The neural networks used in the TaNC have two hidden layers and single node in the
 output layers. The number of nodes in the first and second hidden layers are chosen to be
 $N + 1$ and $2N + 1$, respectively, where N is the number of input observables for that neural
 network. According to the Kolmogorov’s theorem [29], any continuous function $g(x)$ defined

	Signal	Background
Total number of tau-candidates	874266	9526176
Tau-candidates passing preselection	584895	644315
Tau-candidates with $W(p_T, \eta) > 0$	538792	488917
Decay Mode	Training Events	
π^-	300951	144204
$\pi^- \pi^0$	135464	137739
$\pi^- \pi^0 \pi^0$	34780	51181
$\pi^- \pi^- \pi^+$	53247	155793
$\pi^- \pi^- \pi^+ \pi^0$	13340	135871

(tab:trainingEvents)

Table 3.3: Number of events used for neural network training and validation for each selected decay mode.

on a vector space of dimension d spanned by x can be represented by

$$g(x) = \sum_{j=1}^{j=2d+1} \Phi_j \left(\sum_{i=1}^d \phi_i(x) \right) \quad (3.1) \quad \text{eq:Kolmogorov}$$

1039 for suitably chosen functions for Φ_j and ϕ_j . As the form of equation 3.1 is similar to the
 1040 topology of a two hidden-layer neural network, Kolmogorov's theorem suggests that *any*
 1041 classification problem can be solved with a neural network with two hidden layers containing
 1042 the appropriate number of nodes.

The neural network is trained for 500 epochs. At ten epoch intervals, the neural network error is computed using the validation sample to check for over-training (see figure 3.6).

The neural network error E is defined [28] as

$$E = \frac{1}{2} \sum_{i=1}^N (y_{ANN,i} - \hat{y}_i)^2 \quad (3.2) \quad \text{eq:NNerrorFunc}$$

1043 where N is the number of training events, $y_{ANN,i}$ is the neural network output for the i th
 1044 training event, and y_i is the desired (-1 for background, 1 for signal) output the i th event.
 1045 No evidence of over-training is observed.

1046 The neural networks use as input observables the transverse momentum and η of the
 1047 tau-candidates. These observables are included as their correlations with other observables
 1048 can increase the separation power of the ensemble of observables. For example, the opening
 1049 angle in ΔR for signal tau-candidates is inversely related to the transverse momentum,

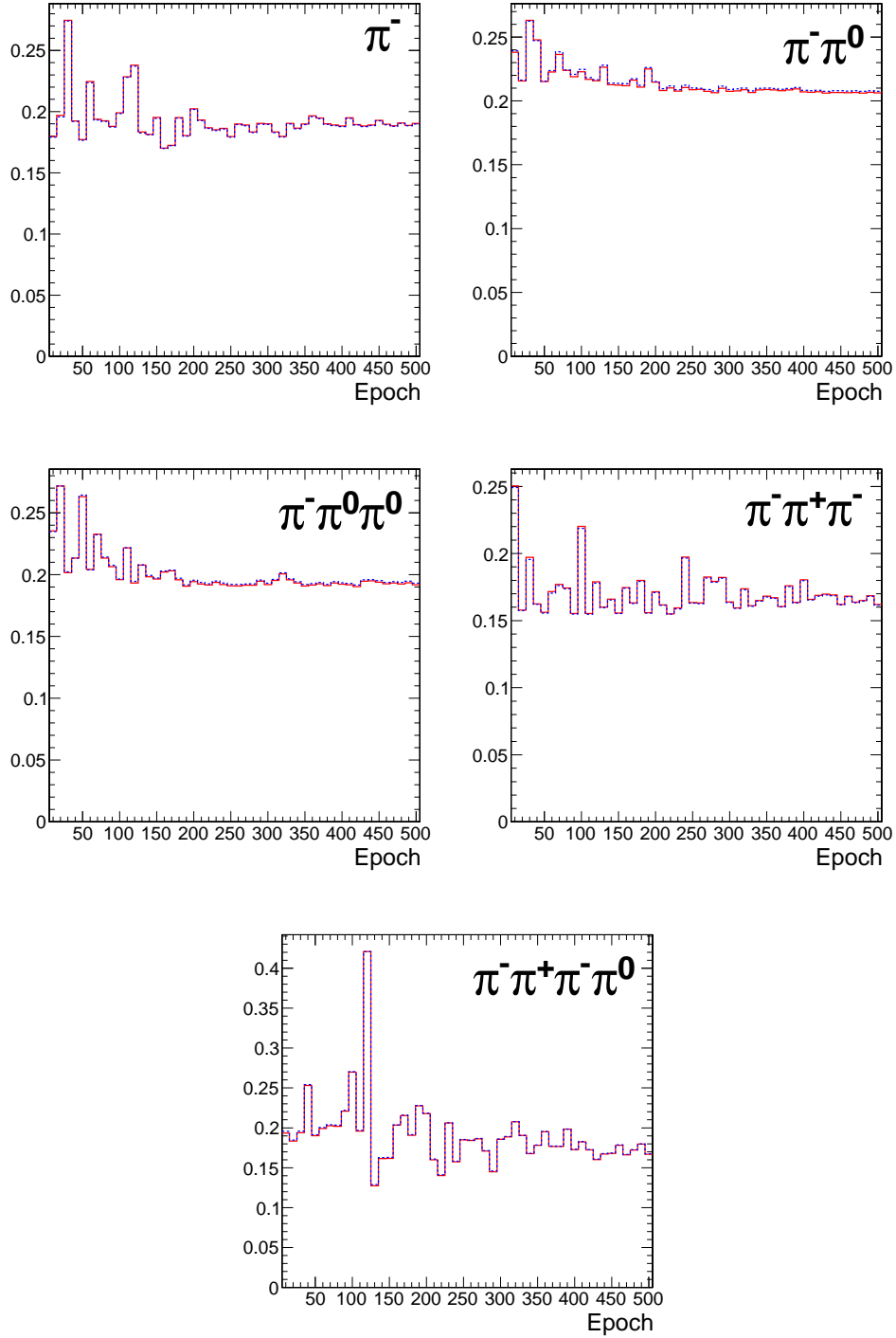


Figure 3.6: Neural network classification error for training (solid red) and testing (dashed blue) samples at ten epoch intervals over the 500 training epochs for each decay mode neural network. The vertical axis represents the classification error, defined by equation 3.2. N.B. that the choice of hyperbolic tangent for neuron activation functions results in the desired outputs for signal and background to be 1 and -1, respectively. This results in the computed neural network error being larger by a factor of four than the case where the desired outputs are (0, 1). Classifier over-training would be evidenced by divergence of the classification error of the training and testing samples, indicating that the neural net was optimizing about statistical fluctuations in the training sample.

(fig:overTrainCheck)

1050 while for background events the correlation is very small [30]. In the training signal and
 1051 background samples, there is significant discrimination power in the p_T spectrum. However,
 1052 it is desirable to eliminate any systematic dependence of the neural network output on p_T
 1053 and η , as in practice the TaNC will be presented with tau-candidates whose $p_T - \eta$ spectrum
 1054 will be analysis dependent. The dependence on p_T and η is removed by applying a p_T and
 1055 η dependent weight to the tau-candidates when training the neural nets.

The weights are defined such that in any region in the vector space spanned by p_T and η where the signal sample and background sample probability density functions are different, the sample with higher probability density is weighted such that the samples have identical $p_T - \eta$ probability distributions. This removes regions of $p_T - \eta$ space where the training sample is exclusively signal or background. The weights are computed according to

$$W(p_T, \eta) = \text{less}(p_{sig}(p_T, \eta), p_{bkg}(p_T, \eta))$$

$$w_{sig}(p_T, \eta) = W(p_T, \eta) / p_{sig}(p_T, \eta)$$

$$w_{bkg}(p_T, \eta) = W(p_T, \eta) / p_{bkg}(p_T, \eta)$$

1056 where $p_{sig}(p_T, \eta)$ and $p_{bkg}(p_T, \eta)$ are the probability densities of the signal and background
 1057 samples after the “leading pion” and dominant decay mode selections. Figure 3.7 shows the
 1058 signal and background training p_T distributions before and after the weighting is applied.

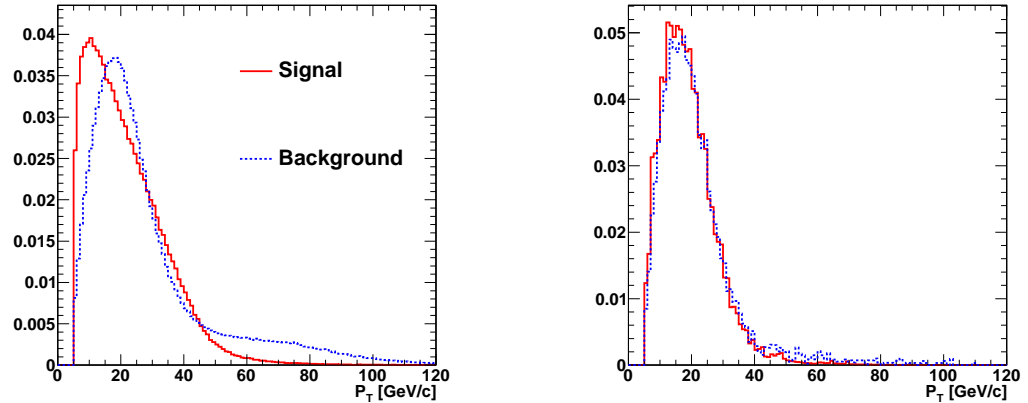


Figure 3.7: Transverse momentum spectrum of signal and background tau-candidates used in neural net training before (left) and after (right) the application of $p_T - \eta$ dependent weight function. Application of the weights lowers the training significance of tau-candidates in regions of $p_T - \eta$ phase space where either the signal or background samples has an excess of events.

(fig:nnTrainingWeights)

1059 Discriminants

1060 Each neural network corresponds to a different decay mode topology and as such each
 1061 network uses different observables as inputs. However, many of the input observables are
 1062 used in multiple neural nets. The superset of all observables is listed and defined below.
 1063 Table 3.4 maps the input observables to their associated neural networks. In three prong
 1064 decays, the definition of the “main track” is important. The main track corresponds to the
 1065 track with charge opposite to that of the total charge of the three tracks. This distinction is
 1066 made to facilitate the use of the “Dalitz” observables, allowing identification of intermediate
 1067 resonances in three-body decays. This is motivated by the fact that the three prong decays
 1068 of the tau generally proceed through $\tau^- \rightarrow a1^- \nu_\tau \rightarrow \pi^- \rho^0 \nu_\tau \rightarrow \pi^- \pi^+ \pi^- \nu_\tau$; the oppositely
 1069 charged track can always be identified with the ρ^0 decay.

1070 **ChargedOutlierAngleN**

1071 ΔR between the Nth charged object (ordered by p_T) in the isolation region and the
 1072 tau-candidate momentum axis. If the number of isolation region objects is less than
 1073 N, the input is set at one.

1074 **ChargedOutlierPtN**

1075 Transverse momentum of the Nth charged object in the isolation region. If the number
 1076 of isolation region objects is less than N, the input is set at zero.

1077 **DalitzN**

1078 Invariant mass of four vector sum of the “main track” and the Nth signal region
 1079 object.

1080 **Eta**

1081 Pseudo-rapidity of the signal region objects.

1082 **InvariantMassOfSignal**

1083 Invariant mass of the composite object formed by the signal region constituents.

1084 **MainTrackAngle**

1085 ΔR between the “main track” and the composite four-vector formed by the signal
1086 region constituents.

1087 **MainTrackPt**

1088 Transverse momentum of the “main track.”

1089 **OutlierNCharged**

1090 Number of charged objects in the isolation region.

1091 **OutlierSumPt**

1092 Sum of the transverse momentum of objects in the isolation region.

1093 **PiZeroAngleN**

1094 ΔR between the Nth π^0 object in the signal region (ordered by p_T) and the tau-
1095 candidate momentum axis.

1096 **PiZeroPtN**

1097 Transverse momentum of the Nth π^0 object in the signal region.

1098 **TrackAngleN**

1099 ΔR between the Nth charged object in the signal region (ordered by p_T) and the
1100 tau-candidate momentum axis, exclusive of the main track.

1101 **TrackPtN**

1102 Transverse momentum of the Nth charged object in the signal region, exclusive of the
1103 main track.

1104 **Neural network performance**

1105 The classification power of the neural networks is unique for each of the decay modes.
1106 The performance is determined by the relative separation of the signal and background
1107 distributions in the parameter space of the observables used as neural network inputs. A
1108 pathological example is the case of tau-candidates with the reconstructed decay mode of
1109 $\tau^- \rightarrow \pi^- \nu_\tau$. If there is no isolation activity, the neural net has no handle with which it

1110 can separate the signal from the background. The neural net output for tau-candidates in
 1111 the testing sample (independent of the training and validation samples) for each of the five
 1112 decay mode classifications is shown in figure 3.8.

1113 When a single neural network is used for classification, choosing an operating point is
 1114 relatively straightforward: the requirement on neural network output is tuned such that the
 1115 desired purity is attained. However, in the case of the TaNC, multiple neural networks are
 1116 used. Each network has a unique separation power (see figure 3.9) and each neural network
 1117 is associated to a reconstructed decay mode that composes different relative fractions of the
 1118 signal and background tau-candidates. Therefore, a set of five numbers is required to define
 1119 an “operating point” (the signal efficiency and background misidentification rate) in the
 1120 TaNC output. All points in this five dimensional cut-space map to an absolute background
 1121 fake-rate and signal efficiency rate. Therefore there must exist a 5D “performance curve”
 1122 which for any attainable signal efficiency gives the lowest fake-rate. A direct method to
 1123 approximate the performance curve is possible using a Monte Carlo technique.

1124 The maximal performance curve can be approximated by iteratively sampling points in
 1125 the five-dimensional cut space and selecting the highest performance points. The collection
 1126 of points in the performance curve are ordered by expected fake rate. During each iteration,
 1127 the sample point is compared to the point before the potential insertion position of the
 1128 sample in the ordered collection. The sample point is inserted into the collection if it has
 1129 a higher signal identification efficiency than the point before it. The sample point is then
 1130 compared to all points in the collection after it (i.e. those with a larger fake rate); any point
 1131 with a lower signal efficiency than the sample point is removed. After the performance curve
 1132 has been determined, the set of cuts are evaluated on an independent validation sample
 1133 to ensure that the measured performance curve is not influenced by favorable statistical
 1134 fluctuations being selected by the Monte Carlo sampling. The performance curves for two
 1135 different transverse momentum ranges are shown in figure 3.10.

The 5D performance curve can also be parameterized by using the probability for a
 tau-candidate to be identified for a given decay mode. An artificial neural network maps
 a point in the space of input observables to some value of neural network output x . The
 neural network training error is given by equation 3.2. A given point in the vector space

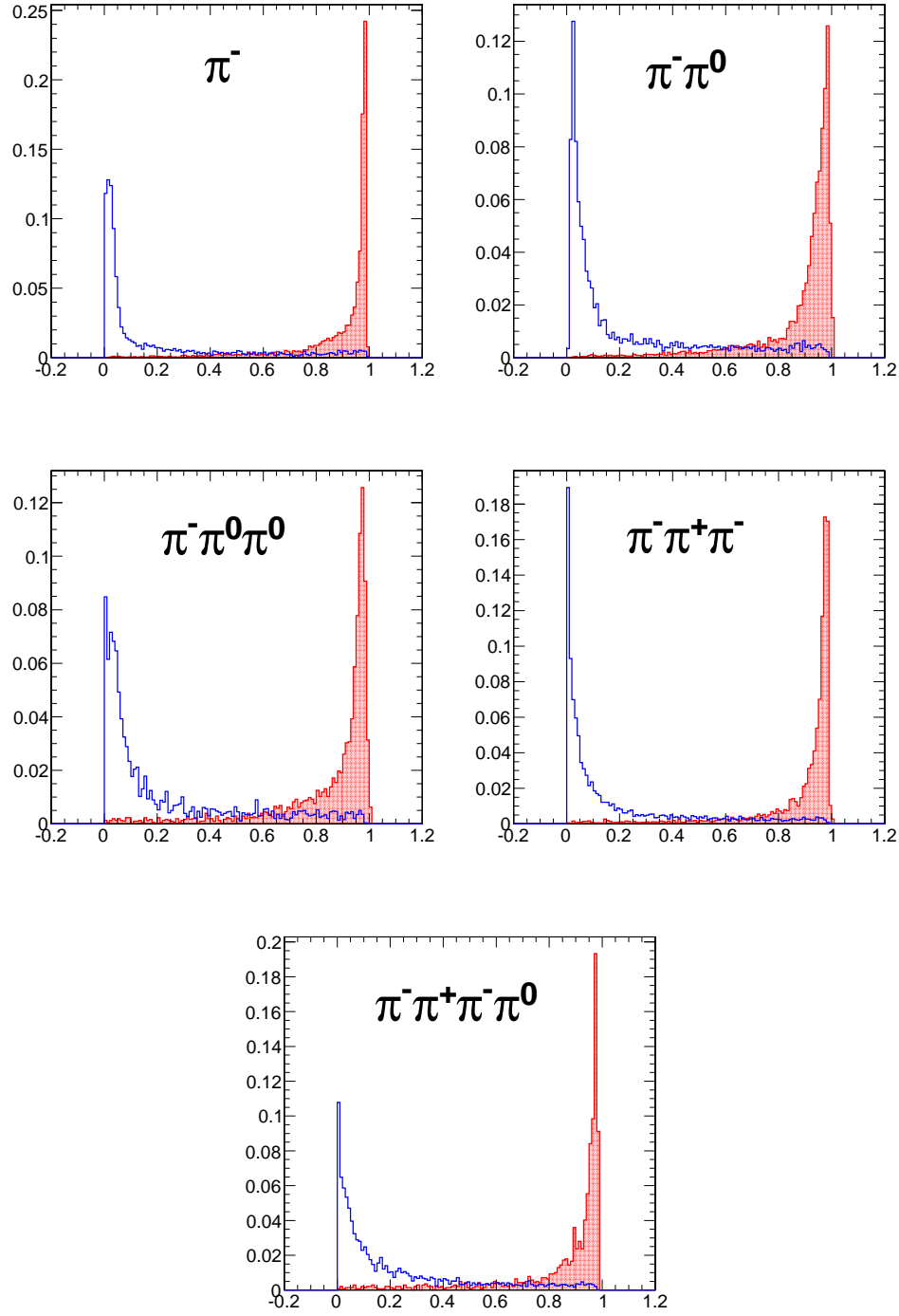


Figure 3.8: Neural network output distributions for the five reconstructed tau-candidate decay modes used in the TaNC for $Z \rightarrow \tau^+\tau^-$ events (red) and QCD di-jet events (blue).

fig:NNoutputDisributions)

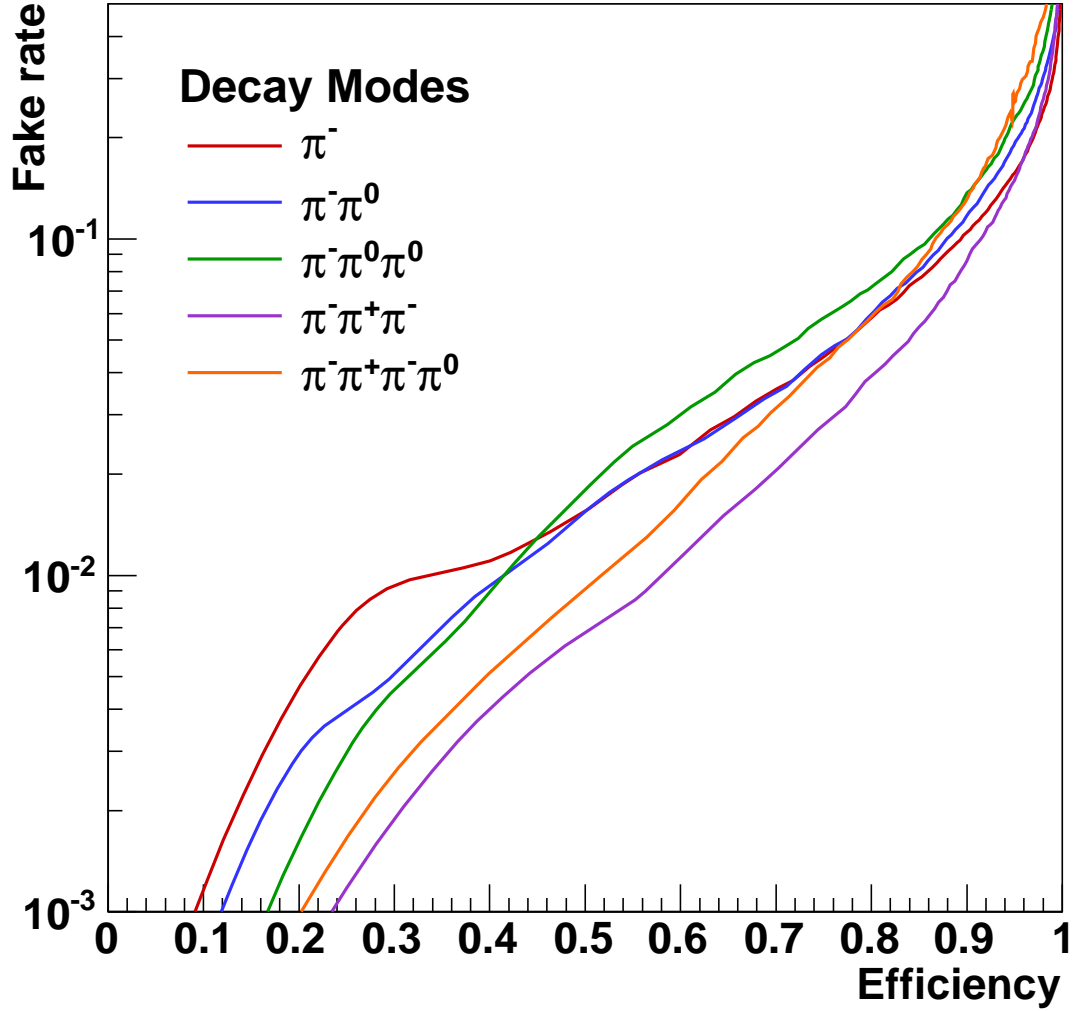


Figure 3.9: Performance curves for the five neural networks used by the TaNC for tau-candidates with transverse momentum greater than 20 GeV/ c . Each curve represents the signal efficiency (on the horizontal axis) and background misidentification rate (vertical axis) for a scan of the neural network selection requirement for a single neural network. The efficiency (or misidentification rate) for each neural network performance curve is defined with respect to the preselected tau-candidates that have the reconstructed decay mode associated with that neural network. Each neural network has a different ability to separate signal and background as each classifier uses different observables as inputs.

(fig:nnPerfCurves)

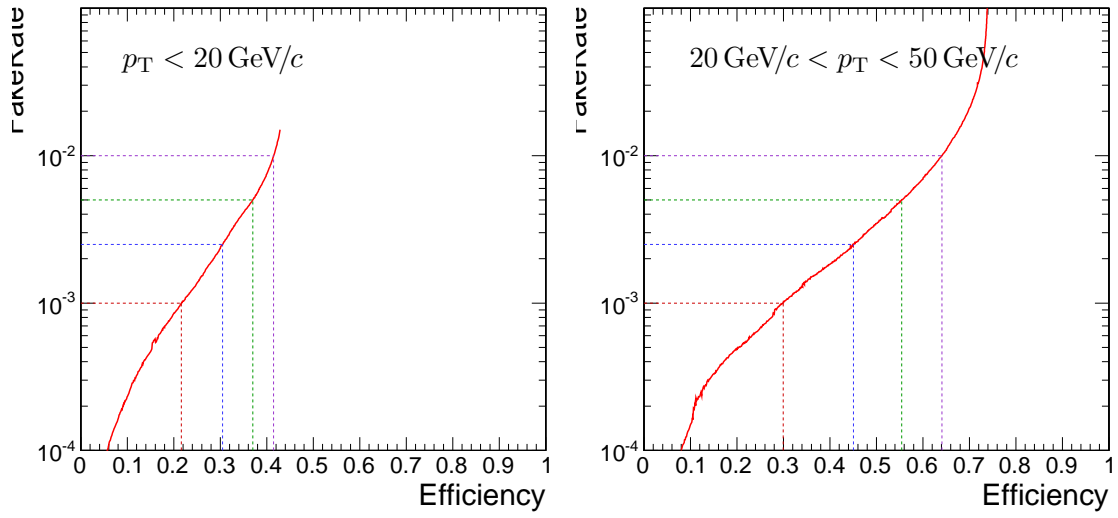


Figure 3.10: Tau Neural Classifier performance curves for tau-candidates with $p_T < 20 \text{ GeV}/c$ (left) and $20 \text{ GeV}/c < p_T < 50 \text{ GeV}/c$ (right). The vertical axis represents the expected fake-rate of QCD jets and the horizontal axis the expected signal efficiency for hadronic tau decays. The performance curve for the low transverse momentum range is worse due to leading pion selection. While both true taus and QCD are removed by this cut, the selection preferentially keeps the QCD tau-candidates with low multiplicities, which increases the number of QCD tau-candidates passing the decay mode selection.

(fig:mcPerfCurves)

spanned by the neural network input observables (denoted as “feature space”) contributes to the neural network training error E by

$$E' = (1 - x)^2 \cdot \rho^\tau + x^2 \cdot \rho^{QCD} \quad (3.3) \quad \{?\}$$

1136 where $\rho^\tau(\rho^{QCD})$ denotes the training sample density of the τ signal and QCD-jet back-
1137 ground at that point in feature space.

The value x assigned by the neural network to this region in feature space should satisfy the requirement of minimal error:

$$\frac{\partial E'}{\partial x} = 0$$

$$0 = -2(1 - x) \cdot \rho^\tau + 2x \cdot \rho^{QCD}$$

$$x = \frac{\rho^\tau}{\rho^\tau + \rho^{QCD}} \quad (3.4) \quad \text{eq:probFracToX}$$

$$\rho^\tau = x(\rho^\tau + \rho^{QCD})$$

$$\frac{\rho^{QCD}}{\rho^\tau} = \frac{1}{x} - 1 \quad (3.5) \quad \text{eq:rawTransform}$$

1138 The ratio $\frac{\rho^{QCD}}{\rho^\tau}$ corresponds to the ratio of the normalized probability density functions of
1139 signal and background input observable distributions, i.e. $\int \rho^\tau d\vec{x} = 1$.

In the case of multiple neural networks, one can derive a formula that maps the output x_j of the neural network corresponding to decay mode j according to the “prior probabilities” $p_j^\tau(p_j^{QCD})$ for true τ lepton hadronic decays (quark and gluon jets) to pass the preselection criteria and be reconstructed with decay mode j . By substituting $\rho^s \rightarrow \rho^s p_j^s$ for $s \in \{\tau, QCD\}$ in equation 3.4, the output x_j can be related to $p_j^\tau(p_j^{QCD})$ by

$$x'_j = \frac{\rho^\tau \cdot p_j^\tau}{\rho^\tau \cdot p_j^\tau + \rho^{QCD} \cdot p_j^{QCD}} = \frac{p_j^\tau}{p_j^\tau + \frac{\rho^{QCD}}{\rho^\tau} \cdot p_j^{QCD}} \quad (3.6) \quad \text{eq:probFracToX}$$

Substituting equation 3.5 into equation 3.6 yields the transformation of the output x_j of the neural neural network corresponding to any selected decay mode j to a single discriminator output x'_j which for a given point on the optimal performance curve should be independent of j .

$$x'_j = \frac{p_j^\tau}{p_j^\tau + \left(\frac{1}{x_j} - 1\right) \cdot p_j^{QCD}} \quad (3.7) \quad \text{eq:TransformCut}$$

1140 In this manner a single number (the “transform cut”) given by Equation 3.7 can be used
1141 to specify any point on the performance curve. The training sample neural network output
1142 after the transformation has been applied is shown in figure 3.12. The performance curve

for the cut on the transformed output is nearly identical to the optimal performance curve determined by the Monte Carlo sampling technique.

The discriminator output of the TaNC algorithm is a continuous quantity, enabling analysis specific optimization of the selection to maximize sensitivity. For the convenience of the user, four operating point benchmark selections are provided in addition to the continuous output. The four operating points are chosen such that for tau-candidates with transverse momentum between 20 and 50 GeV/c, the expected QCD di-jet fake rate will be 0.1%, 0.25%, 0.50% and 1.0%, respectively.

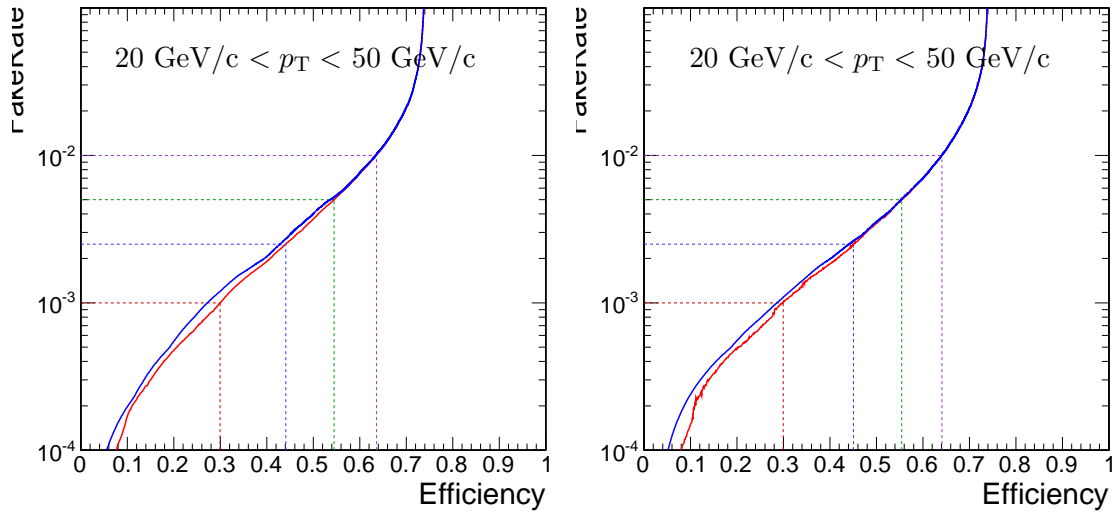


Figure 3.11: Tau Neural Classifier performance curves for tau-candidates with $20 \text{ GeV}/c < p_T < 50 \text{ GeV}/c$. The figure on the left compares the optimal performance curve determined by the Monte Carlo sampling method (red) to the performance curve obtained by scanning the “transform cut” (blue) defined in equation 3.7 from zero to one. The figure on the right is the same set of cuts (and cut transformation values) applied on an independent sample to remove any biases introduced by the Monte Carlo sampling. The four dashed lines indicate the performance for the four benchmark points.

acCurvesWithTransform)?

§3.4 Summary

The Tau Neural classifier introduces two complimentary new techniques for tau lepton physics at CMS: reconstruction of the hadronic tau decay mode and discrimination from quark and gluon jets using neural networks. The decay mode reconstruction strategy presented in section 3.3.1 significantly improves the determination of the decay mode. This

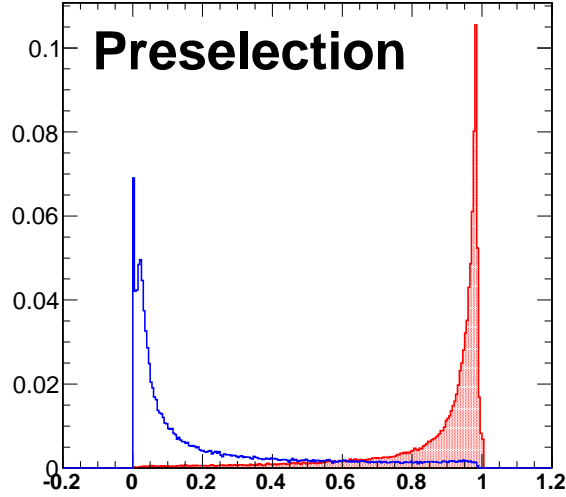


Figure 3.12: Transformed TaNC neural network output for tau-candidates with transverse momentum between 20 and 50 GeV/c that pass the pre-selection criteria. The neural network output for each tau-candidate has been transformation according to equation 3.7. The decay mode probabilities ρ_i^{bkg} , ρ_i^{signal} are computed using the entire transverse momentum range of the sample.

fig:transformedNNOuput)

1156 information has the potential to be useful in studies of tau polarization and background
1157 estimation.

1158 The Tau Neural classifier tau identification algorithm significantly improves tau dis-
1159 crimination performance compared to isolation-based approaches [26] used in previous CMS
1160 analyses. Figure 3.13 compares the performance of the “shrinking cone” isolation tau-
1161 identification algorithm [26] to the performance of the TaNC for a scan of requirements
1162 on the transformed neural network output. The signal efficiency and QCD di-jet fake rate
1163 versus tau-candidate transverse momentum and pseudo-rapidity for the four benchmark
1164 points and the isolation based tau identification are show in figure 3.14. For tau-candidates
1165 with transverse momentum between 20 and 50 GeV/c, the TaNC operating cut can be
1166 chosen such that the two methods have identical signal efficiency; at this point the TaNC
1167 algorithm reduces the background fake rate by an additional factor of 3.9. This reduction
1168 in background will directly improve the significance of searches for new physics using tau
1169 leptons at CMS.

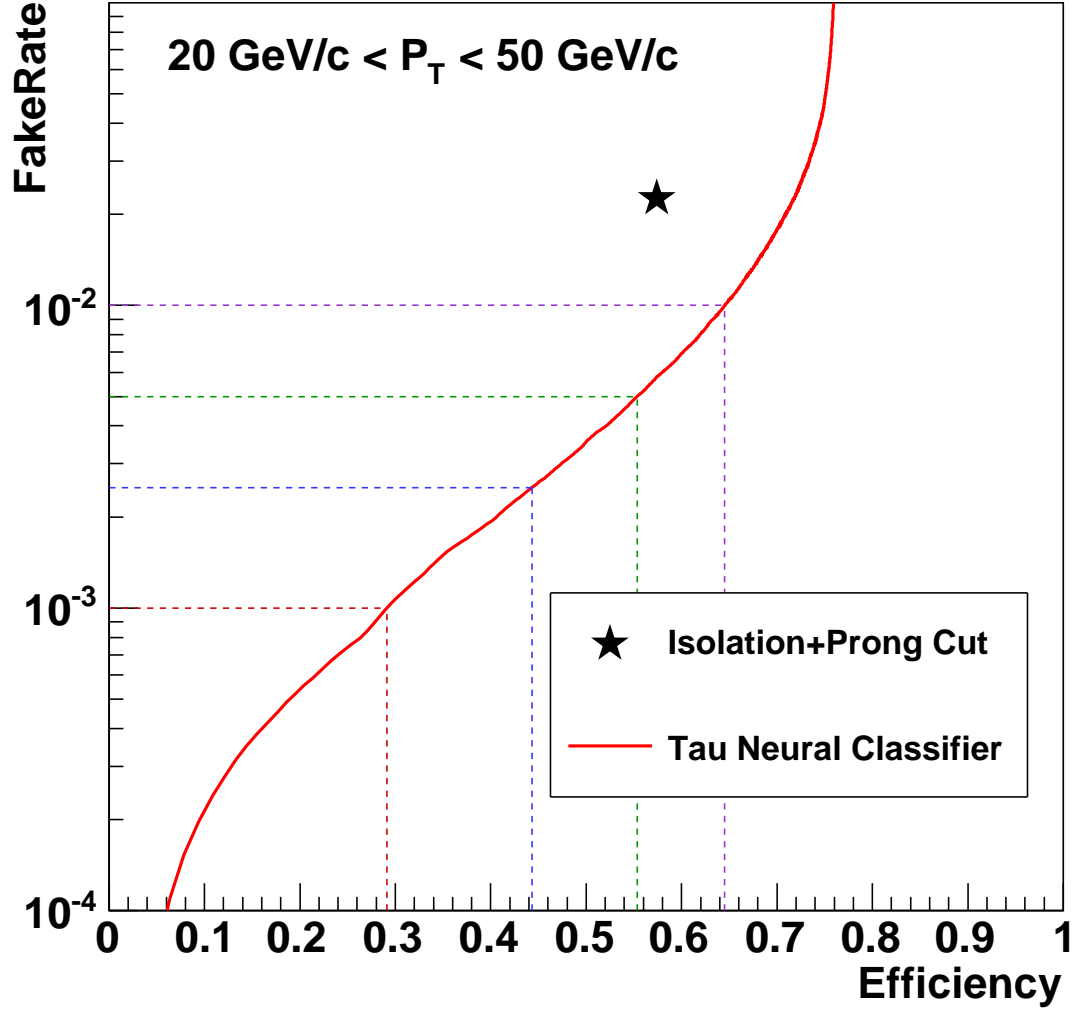


Figure 3.13: Performance curve (red) of the TaNC tau identification for various requirements on the output transformed according to equation 3.7. The horizontal axis is the efficiency for true taus with transverse momentum between 20 and 50 GeV/c to satisfy the tau identification requirements. The vertical axis gives the rate at which QCD di-jets with generator-level transverse momentum between 20 and 50 GeV/c are incorrectly identified as taus. The performance point for the same tau-candidates using the isolation based tau-identification [26] used in many previous CMS analyses is indicated by the black star in the figure. An additional requirement that the signal cone contain one or three charged hadrons (typical in a final physics analysis) has been applied to the isolation based tau-identification to ensure a conservative comparison.

⟨fig:finalPerfCurve⟩

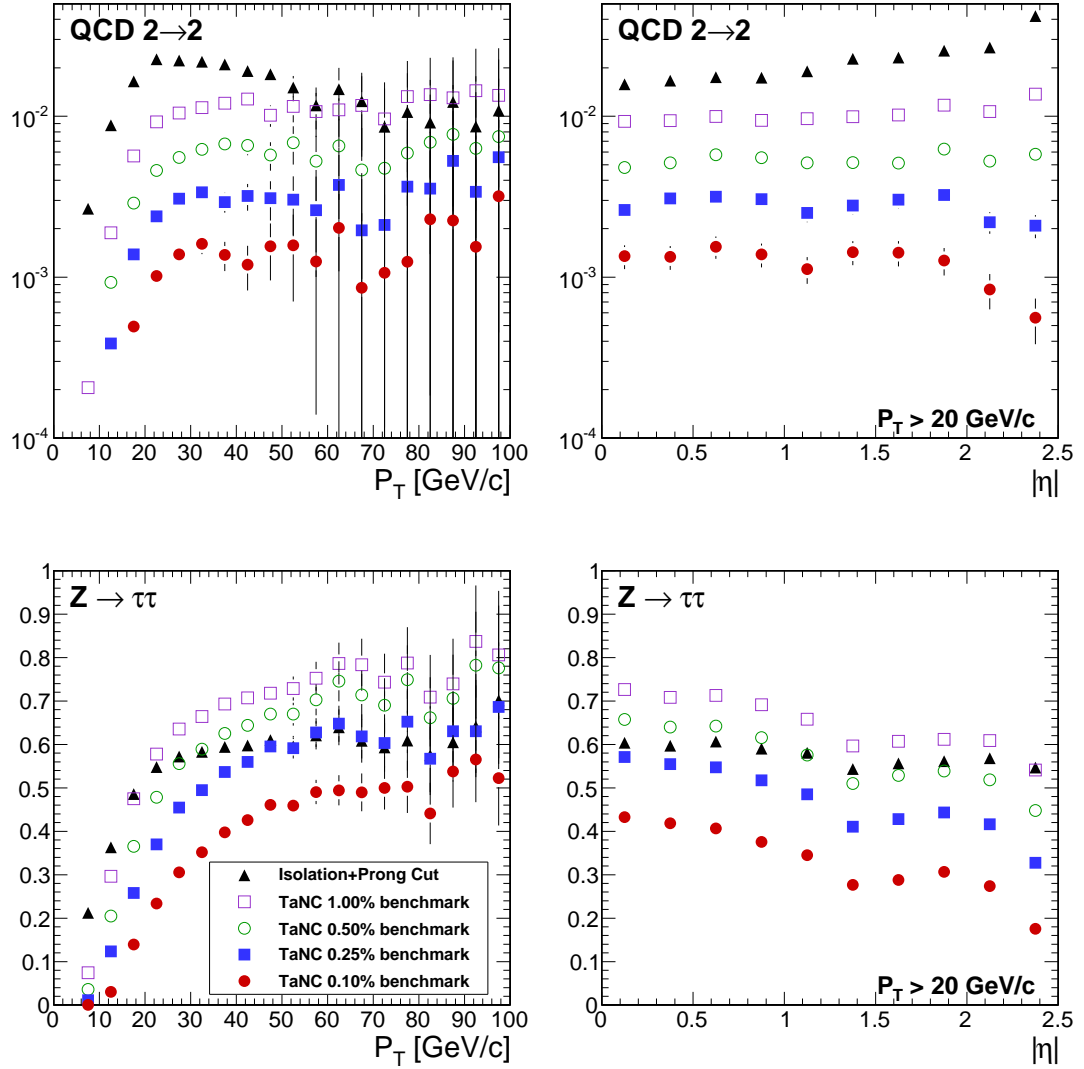


Figure 3.14: Comparison of the identification efficiency for hadronic tau decays from $Z \rightarrow \tau^+\tau^-$ decays (bottom row) and the misidentification rate for QCD di-jets (top row) versus tau-candidate transverse momentum (left) and pseudo-rapidity (right) for different tau identification algorithms. The efficiency (fake-rate) in a given bin is defined as the quotient of the number of true tau hadronic decays (generator level jets) in that bin that are matched to a reconstructed tau-candidate that passes the identification algorithm divided by the number of true tau hadronic decays (generator level jets) in that bin. In the low transverse momentum region both the number of tau-candidates in the denominator and the algorithm acceptance vary rapidly with respect to p_T for both signal and background; a minimum transverse momentum requirement of 20 GeV/c is applied to the pseudorapidity plots to facilitate interpretation of the plots.

(fig:kinematicPerformance)

§3.5 HPS+TaNC: A Hybrid Algorithm

The techniques used in the TaNC have been hybridized with techniques used by the “Hadrons plus Strips” (HPS) algorithm [31]. The combined algorithm is referred to “Hadrons plus Strips and Tau Neural Classifier” (HPS + TaNC) identification algorithm. The algorithm combines the HPS methods of constructing the signal components of the tau candidate and the discrimination methods of the TaNC algorithm. Both algorithms are based on reconstructing individual tau lepton hadronic decay modes, which has been demonstrated to improve the tau identification performance significantly with respect to previously used cone isolation based algorithms [32]. The HPS + TaNC algorithm first reconstructs the hadronic decay mode of the tau, and applies different discriminants based on the reconstructed decay mode. Identification of hadronic tau decays by the HPS + TaNC algorithm proceeds in two stages: first, the hadronic decay mode of the tau is reconstructed and then different discriminators are applied, based on the reconstructed decay mode. In the decay mode reconstruction particular attention is paid to the reconstruction of neutral pions, which are expected for the majority of hadronic decay modes.

§3.5.1 Decay mode reconstruction

The decay mode reconstruction algorithm is seeded by particle-flow jets reconstructed by the anti- k_T algorithm [33]. In order to reconstruct the decay mode, the algorithm needs to merge photon candidates into candidate π^0 mesons. The π^0 candidates are reconstructed by two algorithms which are executed concurrently. The “combinatoric” π^0 algorithm produces a π^0 candidate for every possible pair of photons within the jet. The “strips” algorithm clusters photons strips in $\eta - \phi$. The results of both algorithms are combined and then “cleaned”, resolving multiple hypotheses. The quality of a π^0 candidate is determined according to the following categorical rankings:

- The π^0 candidate is in the ECAL barrel region ($|\eta| < 1.5$) and has invariant mass $|m_{\gamma\gamma} - m_{\pi^0}| < 0.05 \text{ GeV}/c^2$.
- The π^0 candidate is in the ECAL endcap region ($|\eta| > 1.5$) and has invariant mass $m_{\gamma\gamma} < 0.2 \text{ GeV}/c^2$.

- The π^0 candidate contains two or more photons within an $\eta-\phi$ strip of size 0.05×0.20 .
- Photons not satisfying any of the other categories are considered as unresolved π^0 candidates in case they have $p_T > 1.0$ GeV/c.

The symbol m_{π^0} denotes the nominal neutral pion mass [18]. The size of the invariant mass windows in the ECAL endcap and barrel regions is motivated by the resolution on the π^0 mass (illustrated in Figure 3.15) during the commissioning of the particle-flow algorithm in early CMS data [34]. Multiple π^0 candidates in the same category are ranked in quality according to the difference of the reconstructed photon pair mass to the nominal π^0 mass. After the π^0 candidates are ranked, the highest ranked candidate is selected for the final collection. The photon constituents of the highest ranked candidate are removed from remaining π^0 candidates not yet selected for the final collection in order to prevent photons from entering more than one π^0 candidate. The rank of remaining π^0 candidates is reevaluated and the π^0 candidate with the next highest rank is selected for the output collection. The process is repeated until no more π^0 candidates are remaining.

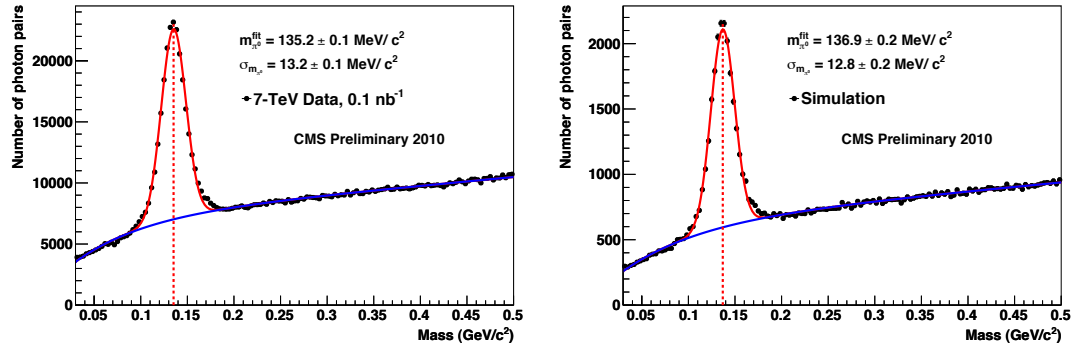


Figure 3.15: Invariant mass distribution of photon pairs reconstructed by the particle-flow in 2010 CMS minimum bias events (left), and predicted by the simulation (right). A clear resonant pick corresponding to the π_0 meson is visible above the combinatoric background. Reference: [34]

(fig:PFPiZeroRes)

Once the final collection of π^0 candidates is determined, tau reconstruction in the HPS + TaNC algorithm proceeds by building tau candidates from reconstructed π^0 candidates and charged hadrons reconstructed by the particle-flow algorithm. A combinatoric approach is again employed for the tau candidate building. A tau candidate hypothesis is

built for every combination of jet constituents (π^0 candidates plus charged hadrons) which has a multiplicity consistent with a hadronic tau decay. The tau candidates are ranked analogous to the ranking utilized for the π^0 reconstruction, but with the following categorical rankings:

- In each decay mode category, the tau candidate with the highest neural network output is selected.
- The tau candidate has unit charge.
- The tau candidate passes the “lead pion” criteria, requiring that there is a photon or charged pion candidate with $p_T > 5 \text{ GeV}/c$.
- The tau candidate passes the HPS invariant mass and collimation¹ requirements.

In case multiple tau candidates satisfy all four categorical requirements, the tau candidate with the highest energy sum of charged and neutral pions is selected as the highest ranking one.

§3.5.2 Hadronic tau discrimination

The final level of discrimination is performed by an ensemble of neural networks, with each neural network corresponding to a specific decay mode, analogously to the method used original TaNC algorithm (Section 3.3.2). The inputs of each neural network are different and correspond to the observables (invariant mass, Dalitz masses) available for its associated decay mode. The neural networks are trained on samples simulated $Z \rightarrow \tau^+ \tau^-$ events (“signal”) and QCD di-jet events selected in the 7 TeV data collected by CMS in 2010 (“background”). All of the tau hypothesis from a given jet reconstructed in data are used for training. The $Z \rightarrow \tau^+ \tau^-$ signal sample is generated by PYTHIA [35] which has been interfaced TAUOLA [36] for the purpose of generating the tau decays and simulated passed through the “full” GEANT [37] based simulation of the CMS detector. Only tau candidates which have been reconstructed in a decay mode matching the true decay mode of the tau

¹The invariant mass of the signal candidates is required to be compatible with the resolution for that decay mode. The collimation selection requires the maximum ΔR between any two signal candidates to be less than $2.8/E_T$, where E_T is the total transverse energy of the signal candidates. A full description is available in [31].

on generator level enter the signal training sample. The neural network implementation, network layout, and training strategies are the same as in the original TaNC algorithm described in this chapter. To account for differences in the input signal purity and separation power of the neural networks between decay modes, the outputs of each neural network are transformed according to the method described in [38]. Multiple working-points corresponding to different purities are provided. The “loose” working point corresponds to an approximate fake-rate of 1%, and has slightly higher signal efficiency performance at high p_T than the corresponding HPS-only working point.

§3.6 Electron and Muon Rejection

Additional discriminators must be applied to prevent electrons and muons from being identified as hadronic tau decays. This is especially important for removing $Z \rightarrow e^+e^-$ and $Z \rightarrow \mu^+\mu^-$ contributions when selecting events with two taus and requiring one of them to decay leptonically and the other hadronically. The electron and muon discrimination algorithms and performance are described in detail in [26]. A cursory overview of the techniques used are given here. Muon removal is achieved with high purity by requiring that no track in the signal collection of the tau candidate is matched to a segment² in the muon system. The rejections of true electrons is more difficult. Electrons leave no signal in the muon system and produce Bremsstrahlung photons as they travel through the magnetic field. The most significant difference from a true hadronic tau is that an electron is not expected to deposit any energy in the hadronic calorimeter. Electrons are thus rejected by requiring that there is a HCAL energy deposit with a magnitude that is greater than 10% of the momentum of the leading track in the tau.

²A track reconstructed in the DT or CSC sub-detectors.

Input observable	Neural network				
	$\pi^- \nu_\tau$	$\pi^- \pi^0 \nu_\tau$	$\pi^- \pi^0 \pi^0 \nu_\tau$	$\pi^- \pi^+ \pi^- \nu_\tau$	$\pi^- \pi^+ \pi^- \pi^0 \nu_\tau$
ChargedOutlierAngle1	•	•	•	•	•
ChargedOutlierAngle2	•	•	•	•	•
ChargedOutlierPt1	•	•	•	•	•
ChargedOutlierPt2	•	•	•	•	•
ChargedOutlierPt3	•	•	•	•	•
ChargedOutlierPt4	•	•	•	•	•
Dalitz1			•	•	•
Dalitz2			•	•	•
Eta	•	•	•	•	•
InvariantMassOfSignal		•	•	•	•
MainTrackAngle		•	•	•	•
MainTrackPt	•	•	•	•	•
OutlierNCharged	•	•	•	•	•
OutlierSumPt	•	•	•	•	•
PiZeroAngle1		•	•		•
PiZeroAngle2			•		
PiZeroPt1		•	•		•
PiZeroPt2			•		
TrackAngle1				•	•
TrackAngle2				•	•
TrackPt1				•	•
TrackPt2				•	•

Table 3.4: Input observables used for each of the neural networks implemented by the Tau Neural Classifier. The columns represents the neural networks associated to various decay modes and the rows represent the superset of input observables (see section 3.3.2) used in the neural networks. A dot in a given row and column indicates that the observable in that row is used in the neural network corresponding to that column.

(tab:nn'var'table)

1263

Chapter 4

1264

Mass Reconstruction: The Secondary Vertex Fit

1265

`<ch:svfit>`

1266

The dominant background in the search for a Higgs decaying to a $\tau^+\tau^-$ pair is Standard Model $Z \rightarrow \tau^+\tau^-$ events. The most “natural” observable to discriminate between Higgs signal and Z background would be the invariant mass of the di-tau system, utilizing the fact that the Z resonance is well known ($m_Z = 91.1876 \pm 0.0021 \text{ GeV}/c^2$) and has a narrow width ($\Gamma_Z = 2.4952 \pm 0.0023 \text{ GeV}$) [18]. The experimental complication in this approach is due to the neutrinos produced in the tau lepton decays, which escape detection and carry away an unmeasured amount of energy, and making it difficult to reconstruct the tau lepton four-vectors. In this chapter we give an overview of techniques used in previous literature [17, 39, 40] to construct an observable related to the tau pair mass. We then introduce a new algorithm, called the Secondary Vertex (SV) fit. The SVfit reconstructs the “full” tau pair mass, and provides increased performance with respect to techniques previously used in the literature.

1277

1278

§4.1 Existing mass reconstruction algorithms

1279

The simplest observable related to the $\tau^+\tau^-$ mass is one can construct that is sensitive to new particle content is the invariant mass of the visible (reconstructible) decay products associated with each tau decays. This quantity, referred in this document as the “Visible Mass,” has the advantages of simplicity and lack of exposure to systematic errors associated with the reconstruction of the E_T^{miss} . However, no attempt is made to reconstruct the neutrinos in the event. The reconstructed mass is thus systematically smaller than mass of the resonance which produced the tau leptons. The visible mass is typically on the order of

1285

1286 1/2 of the resonance mass, depending on the kinematic requirements applied to the visible
1287 products of the tau decays.

The Collinear Approximation is a technique previously used [17] to reconstruct the *full* $\tau^+\tau^-$ mass. In an event with two tau decays, there are a total of six unknowns associated with the missing energy: the three components of the momentum of each neutrino. The Collinear Approximation makes the assumption that the neutrinos have the same direction as their associated visible decay products. This assumption reduces the number of unknown quantities to two, corresponding to the total energy of each neutrino. These two unknowns can be solved for by using the two components of the reconstructed missing transverse energy, which in the ideal case corresponds to the transverse component of the vector sum of the two neutrino's four momentum. The characteristic equation of the Collinear Approximation is

$$\begin{pmatrix} E_x^{\text{miss}} \\ E_y^{\text{miss}} \end{pmatrix} = \begin{pmatrix} \cos \phi_1 & \cos \phi_2 \\ \sin \phi_1 & \sin \phi_2 \end{pmatrix} \begin{pmatrix} E_1 \\ E_2 \end{pmatrix} \quad (4.1) \quad \text{eq:CollinearAppr}$$

where $(E_x^{\text{miss}}, E_y^{\text{miss}})$ are the two components of the reconstructed missing transverse energy, $\phi_{1(2)}$ is the azimuthal angle of the visible component of the first (second) tau decay, and $E_{1(2)}$ is the reconstructed energy of neutrino of the first (second) tau decay. E_1 and E_2 can be extracted by inverting the matrix on the right hand side of Equation 4.1.

$$\begin{pmatrix} E_1 \\ E_2 \end{pmatrix} = \frac{1}{\sin(\phi_2 - \phi_1)} \begin{pmatrix} \sin \phi_2 & -\cos \phi_2 \\ -\sin \phi_1 & \cos \phi_1 \end{pmatrix} \begin{pmatrix} E_x^{\text{miss}} \\ E_y^{\text{miss}} \end{pmatrix} \quad (4.2) \quad \text{eq:CollinearAppr}$$

1288 The Collinear Approximation suffers from two problems. The approximation can fail
1289 (yielding unphysical negative energies for the reconstructed neutrinos) when the missing
1290 transverse energy is mis-measured. The events with unphysical solutions must be removed
1291 from the analysis, leading to a dramatic reduction in acceptance (on the order of 50% in
1292 this analysis). Improvements to the collinear approximation algorithm have recently been
1293 made which aim to recover part of the events with unphysical solutions [41]. But even with
1294 these improvements, no physical solution is still found for a large fraction of signal events.
1295 Additionally, the method is numerically sensitive when the two τ lepton are nearly back-

1296 to-back in azimuth. In these cases the $\sin(\phi_2 - \phi_1)^{-1}$ term in Equation 4.2 is very large
 1297 and small mis-measurements of the missing transverse energy can produce a large tail on
 1298 the reconstructed mass. This tail is particularly large for low-mass resonances. The large
 1299 tail for low mass is predominantly due to the fact (discussed in subsection 4.4.2) that the
 1300 kinematic requirements¹ applied on the visible decay products preferentially selects events
 1301 where the visible decay products carry the majority of the energy of the original τ lepton,
 1302 reducing the amount of true missing energy in the event.

1303 §4.2 The Secondary Vertex fit

1304 A novel algorithm is presented in the following, which succeeds in finding a physical solution
 1305 for every event. As an additional benefit, the new algorithm is found to improve the di-tau
 1306 invariant mass resolution, making it easier to separate the Higgs signal from the $Z \rightarrow \tau^+ \tau^-$
 1307 background.

1308 The novel Secondary Vertex fit (SVfit) algorithm for di-tau invariant mass reconstruc-
 1309 tion that we present in the following utilizes a likelihood maximization to fit a $\tau^+ \tau^-$ in-
 1310 variant mass hypothesis for each event. The likelihood is composed of separate terms which
 1311 represent probability densities of:

- 1312 • tau decay kinematics
- 1313 • matching between the momenta of neutrinos produced in the tau decays and the
 1314 reconstructed missing transverse momentum
- 1315 • a regularization “ p_T -balance” term which accounts for the effects on the di-tau in-
 1316 variant mass of acceptance cuts on the visible tau decay products
- 1317 • the compatibility of tau decay parameters with the position of reconstructed tracks
 1318 and the known tau lifetime of $c\tau = 87 \mu\text{m}$ [18].

1319 The likelihood is maximized as function of a set of parameters which fully describe the tau
 1320 decay.

¹The kinematic requirements on the visible decay products are necessary to reduce backgrounds and maintain compatibility with un-prescaled event triggers. This topic is discussed in detail in Chapter 5.

§4.3 Parametrization of tau decays

The decay of a tau of visible four-momentum p_{vis} measured in the CMS detector (“laboratory”) frame can be parametrized by three variables. The invisible (neutrino) momentum is fully determined by these parameters.

The “opening-angle” θ is defined as the angle between the boost direction of the tau lepton and the momentum vector of the visible decay products in the rest frame of the tau. The azimuthal angle of the tau in the lab frame is denoted as $\bar{\phi}$ (we denote quantities defined in the laboratory frame by a overline). A local coordinate system is defined such that the \bar{z} -direction lies along the visible momentum and $\bar{\phi} = 0$ lies in the plane spanned by the momentum vector of the visible decay products and the proton beam direction. The third parameter, $m_{\nu\nu}$, denotes the invariant mass of the invisible momentum system.

Given θ , $\bar{\phi}$ and $m_{\nu\nu}$, the energy and direction of the tau lepton can be computed by means of the following equations: The energy of the visible decay products in the rest frame of the tau lepton is related to the invariant mass of the neutrino system by:

$$E^{vis} = \frac{m_\tau^2 + m_{vis}^2 - m_{\nu\nu}^2}{2m_\tau} \quad (4.3) \quad \text{eq:restFrameMor}$$

Note that for hadronic decays, $m_{\nu\nu}$ is a constant of value zero, as only a single neutrino is produced. Consequently, the magnitude of P^{vis} depends on the reconstructed mass of the visible decay products only and is a constant during the SVfit.

The opening angle $\bar{\theta}$ between the tau lepton direction and the visible momentum vector in the laboratory frame is determined by the rest frame quantities via the (Lorentz invariant) component of the visible momentum perpendicular to the tau lepton direction:

$$\begin{aligned} p_\perp^{vis} &= \bar{p}_\perp^{vis} \\ \Rightarrow \sin \bar{\theta} &= \frac{p_\perp^{vis} \sin \theta}{\bar{p}^{vis}} \end{aligned} \quad (4.4) \quad \text{eq:labFrameOpen}$$

Substituting the parameters $m_{\nu\nu}$ and θ into equations 4.3 and 4.4, the energy of the tau is obtained by solving for the boost factor γ in the Lorentz transformation between tau rest frame and laboratory frame of the visible momentum component parallel to the tau

direction:

$$\begin{aligned}\bar{p}^{vis} \cos \bar{\theta} &= \gamma \beta E^{vis} + \gamma p^{vis} \cos \theta \\ \Rightarrow \gamma &= \frac{E^{vis}[(E^{vis})^2 + (\bar{p}^{vis} \cos \bar{\theta})^2 - (p^{vis} \cos \theta)^2]^{1/2} - p^{vis} \cos \theta \bar{p}^{vis} \cos \bar{\theta}}{(E^{vis})^2 - (p^{vis} \cos \theta)^2}, \\ E^\tau &= \gamma m_\tau\end{aligned}$$

1335 The energy of the tau lepton in the laboratory frame as function of the measured visible
1336 momentum depends on two of the three parameters only - the rest frame opening angle θ and
1337 the invariant mass $m_{\nu\nu}$ of the neutrino system. The direction of the tau lepton momentum
1338 vector is not fully determined by θ and $m_{\nu\nu}$, but is constrained to lie on the surface of a
1339 cone of opening angle $\bar{\theta}$ (given by equation 4.4), the axis of which is given by the visible
1340 momentum vector. The tau lepton four-vector is fully determined by the addition of the
1341 third parameter $\bar{\phi}$, which describes the azimuthal angle of the tau lepton with respect to the
1342 visible momentum vector. The spatial coordinate system used is illustrated in Figure 4.1.

1343 §4.4 Likelihood for tau decay

The probability density functions for the tau decay kinematics are taken from the kinematics review of the PDG [18]. The likelihood is proportional to the phase-space volume for two-body ($\tau \rightarrow \tau_{had}\nu$) and three-body ($\tau \rightarrow e\nu\nu$ and $\tau \rightarrow \mu\nu\nu$) decays. For two-body decays the likelihood depends on the decay angle θ only:

$$d\Gamma \propto |\mathcal{M}|^2 \sin \theta d\theta$$

For three-body decays, the likelihood depends on the invariant mass of the neutrino system also:

$$d\Gamma \propto |\mathcal{M}|^2 \frac{((m_\tau^2 - (m_{\nu\nu} + m_{vis})^2)(m_\tau^2 - (m_{\nu\nu} - m_{vis})^2))^{1/2}}{2m_\tau} m_{\nu\nu} dm_{\nu\nu} \sin \theta d\theta \quad (4.5) \quad \text{eq:pdfKineLepton}$$

1344 In the present implementation of the SVfit algorithm, the matrix element is assumed to be
1345 constant, so that the likelihood depends on the phase-space volume of the decay only ².

1346 §4.4.1 Likelihood for reconstructed missing transverse momentum

1347 Momentum conservation in the plane perpendicular to the beam axis implies that the
1348 vectorial sum of the momenta of all neutrinos produced in the decay of the tau lepton pair

²The full matrix elements for tau decays may be added in the future, including terms for the polarization of the tau lepton pair, which is different in Higgs and Z decays [42].

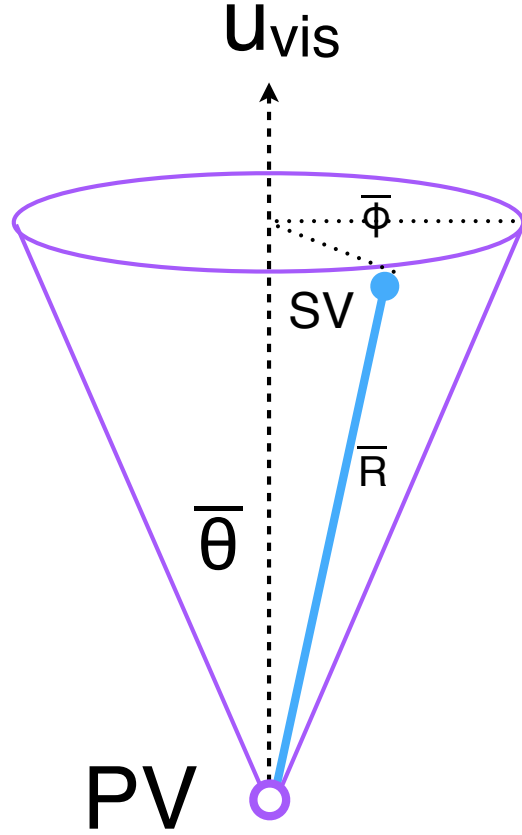


Figure 4.1: Illustration of the coordinate system used by the SVfit to describe the decays of tau leptons.

fig:svFitDecayParDiagram)

1349 matches the reconstructed missing transverse momentum. Differences are possible due to
 1350 the experimental resolution and finite p_T of particles escaping detection in beam direction
 1351 at high $|\eta|$.

The E_T^{miss} resolution is measured in $Z \rightarrow \mu^+ \mu^-$ events selected in the 7 TeV data collected by CMS in 2010. Corrections are applied to the distribution of E_T^{miss} in the Monte Carlo simulated events to match the resolution measured in data. The uncertainty on this correction factor is taken as a “shape systematic.” The treatment of this correction and its corresponding uncertainty are described in Chapters 7 and 8. The momentum vectors of reconstructed E_T^{miss} and neutrino momenta given by the fit parameters are projected in direction parallel and perpendicular to the direction of the $\tau^+ \tau^-$ momentum vector. For both components, a Gaussian probability function is assumed. The width and mean values

of the Gaussian in parallel (“ \parallel ”) and perpendicular (“ \perp ”) direction are:

$$\sigma_{\parallel} = \max(7.54(1 - 0.00542 \cdot q_T), 5.)$$

$$\mu_{\parallel} = -0.96$$

$$\sigma_{\perp} = \max(6.85(1 - 0.00547 \cdot q_T), 5.)$$

$$\mu_{\perp} = 0.0,$$

1352 where q_T denotes the transverse momentum of the tau lepton pair.

1353 §4.4.2 Likelihood for tau lepton transverse momentum balance

(sec:ptBalance)

The tau lepton transverse momentum balance likelihood term represents the probability $p(p_T^{\tau}|M_{\tau\tau})$ for a tau to have a certain p_T , given that the tau is produced in the decay of a resonance of mass $M_{\tau\tau}$. The likelihood is constructed by parametrizing the shape of the tau lepton p_T distribution in simulated Higgs $\rightarrow \tau^+\tau^-$ events as a function of the Higgs mass. The functional form of the parametrization is taken to be the sum of two terms. The first term, denoted by $p^*(p_T|M)$, is derived by assuming an isotropic two-body decay, that is

$$dp^* \propto \sin\theta d\theta.$$

Performing a variable transformation from θ to $p_T \sim \frac{M}{2} \sin\theta$, we obtain

$$\begin{aligned} p^*(p_T|M) &= \frac{dp}{dp_T} = \frac{dp}{d\cos\theta} \left| \frac{d\cos\theta}{dp_T} \right| \\ &\propto \left| \frac{d}{dp_T} \sqrt{1 - \left(2\frac{p_T}{M}\right)^2} \right| \\ &= \frac{1}{\sqrt{\left(\frac{M}{2p_T}\right)^2 - 1}}. \end{aligned} \tag{4.6} \text{eq:ptBalanceTerm}$$

The first term of the p_T -balance likelihood is taken as the convolution of equation 4.6 with a Gaussian of width s . The second term is taken to be a Gamma distribution of scale parameter θ and shape parameter k , in order to account for tails in the p_T distribution of the tau lepton pair. The complete functional form is thus given by

$$p(p_T|M) \propto \int_0^{\frac{M}{2}} p^*(p'_T|M) e^{-\frac{(p_T - p'_T)^2}{2s^2}} dp'_T + a\Gamma(p_T, k, \theta). \tag{4.7} \text{eq:ptBalanceLike}$$

Numerical values of the parameters s , θ and k are determined by fitting function 4.7 to the tau lepton p_T distribution in simulated Higgs $\rightarrow \tau^+\tau^-$ events. The relative weight a of the two terms is also determined in the fit. Replacing the integrand in equation 4.7 by its Taylor

expansion, so that the integration can be carried out analytically, keeping polynomial terms up to fifth order, and assuming the fit parameters to depend at most linearly on the Higgs mass, we obtain the following numerical values for the parameters:

$$\begin{aligned}s &= 1.8 + 0.018 \cdot M_{\tau\tau} \\ k &= 2.2 + 0.0364 \cdot M_{\tau\tau} \\ \theta &= 6.74 + 0.02 \cdot M_{\tau\tau} \\ a &= 0.48 - 0.0007 \cdot M_{\tau\tau}.\end{aligned}$$

1354 The motivation to add the p_T -balance likelihood to the SVfit is to add a “regulariza-
1355 tion” term which compensates for the effect of p_T cuts applied on the visible decay products
1356 of the two tau leptons. In particular for tau lepton pairs produced in decays of resonances
1357 of low mass, the visible p_T cuts significantly affect the distribution of the visible momentum
1358 fraction $x = \frac{E_{vis}}{E_\tau}$. The effect is illustrated in figures 4.3 and 4.4. If no attempt would be
1359 made to compensate for this effect, equations 4.4, 4.5 would yield likelihood values that
1360 are too high at low x , resulting in the SVfit to underestimate the energy of visible decay
1361 products (overestimate the energy of neutrinos) produced in the tau decay, resulting in a
1362 significant tail of the reconstructed mass distribution in the high mass region. The $\tau^+\tau^-$
1363 invariant mass distribution reconstructed with and without the p_T -balance likelihood term
1364 is shown in figure 4.2. A significant improvement in resolution and in particular a significant
1365 reduction of the non-Gaussian tail in the region of high masses is seen.

1366 §4.4.3 Secondary vertex information

1367 The parametrization of the tau decay kinematics described in section 4.3 can be extended
1368 to describe the production and decay of the tau. As the flight direction of the tau is already
1369 fully determined by the parameters θ , $\bar{\phi}$ and $m_{\nu\nu}$, the position of the secondary (decay)
1370 vertex is hence fully determined by addition of a single parameter for the flight distance,
1371 r . The tau lifetime $c\tau = 87 \mu\text{m}$ is large enough to allow the displacement of the tau decay
1372 vertex from the primary event vertex to be resolved by the CMS tracking detector. The
1373 resolution provided by the CMS tracking detector is utilized to improve the resolution on
1374 the $\tau^+\tau^-$ invariant mass reconstructed by the SVfit algorithm. The likelihood term based on
1375 the secondary vertex information is based on the compatibility of the decay vertex position

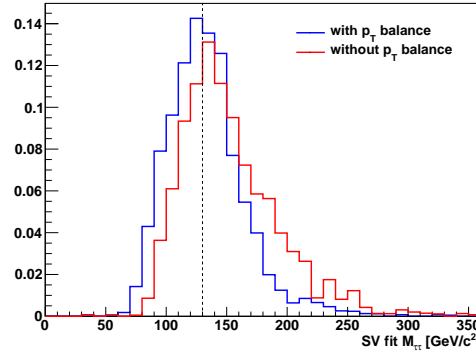


Figure 4.2: Distribution of di-tau invariant mass reconstructed by the SVfit algorithm in simulated Higgs events with $m_{A^0} = 130 \text{ GeV}/c^2$. The SVfit algorithm is run in two configurations, with (blue) and without (red) the p_T -balance likelihood term included in the fit.

with the reconstructed tracks of charged tau decay products. Perhaps surprisingly, it turns out that the flight distance parameter R is sufficiently constrained even for tau decays into a single charged hadron, electron or muon.

The parameter R can be constrained further by a term which represents the probability for a tau lepton of momentum P to travel a distance d before decaying:

$$p(d|P) = \frac{m_\tau}{Pc\tau} e^{-\frac{m_\tau d}{Pc\tau}}$$

The likelihood terms for the secondary vertex fit have been implemented in the SVfit algorithm. In the analysis presented in this note, the decay vertex information is not used, however, because of systematic effects arising from tracker (mis-)alignment which are not yet fully understood.

§4.5 Performance

The tau pair mass reconstructed by the Secondary Vertex fit (“SVfit mass”) provides the observable with the largest separation between signal Higgs events and the dominant $Z \rightarrow \tau^+\tau^-$ background. The mean of the SVfit mass is located at the true mass of the di-tau pair. The SVfit algorithm has a higher acceptance and better resolution than the Collinear Approximation algorithm. The SVfit always finds a physical solution, improving the efficiency of the collinear approximation by a factor of two. Additionally, it has a much better resolution. The collinear approximation reconstructed mass distribution has a large

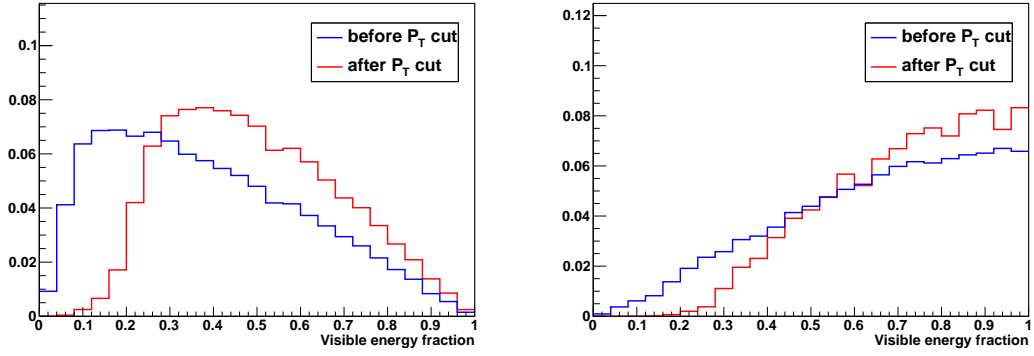


Figure 4.3: Normalized distributions of the fraction of total tau decay energy carried by the muon (left) and hadronic constituents (right) in simulated Higgs events with $m_{A^0} = 130 \text{ GeV}/c^2$. The distribution is shown before (blue) and after (red) the requirement on the p_T of the visible decay products described in Chapter 5.

(fig:ptBalancePtVisCuts)

1391 tail at high mass due to events with poorly measured E_T^{miss} . The shape of the SVfit dis-
 1392 tribution is nearly Gaussian. The comparison is illustrated in Figure 4.5. Previous searches
 1393 for Higgs bosons decaying to tau leptons [39] have in general used the “visible mass” as
 1394 the observable used to search for new resonances. The SVfit method has the obvious dif-
 1395 ference that it reconstructs the “full” tau pair mass, which is the most natural observable
 1396 corresponding to a particle decaying to tau leptons. In addition, the relative resolution³ of
 1397 the SV fit is superior to that of the visible mass. This feature is illustrated in Figure 4.6.
 1398 In Figure 4.6, the visible mass distribution is scaled by an arbitrary number such that the
 1399 scaled mean of the distribution matches the true mass of the tau pair (and the SVfit mass).
 1400 The width of the SVfit distribution is smaller than that of the scaled visible mass distri-
 1401 bution, indicating better performance. The increase in relative resolution allows a “bump,”
 1402 due to the presence of signal events, to be more easily distinguished from the $Z \rightarrow \tau^+\tau^-$
 1403 background. This increases the power of the search for the new signal.

³We define this metric of performance as the variance of a distribution divided by its mean.

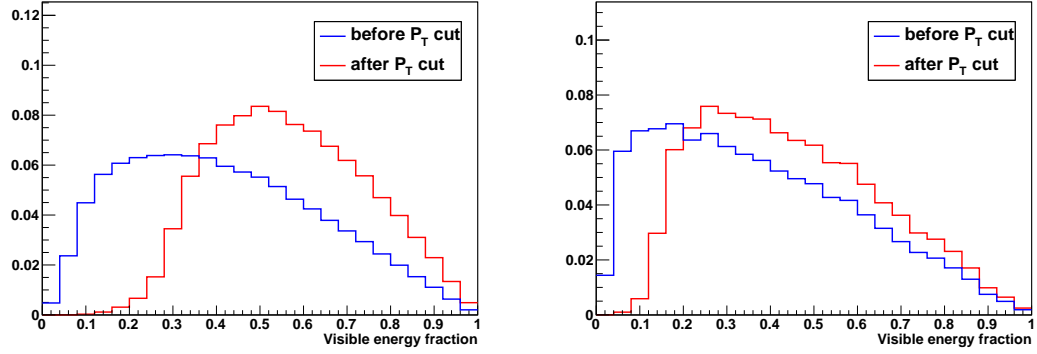


Figure 4.4: Normalized distributions of the fraction of total tau decay energy carried by the muon in simulated $Z \rightarrow \tau^+\tau^-$ (left) and Higgs events with $m_{A^0} = 200 \text{ GeV}/c^2$ (right). The distribution is shown before (blue) and after (red) the requirement that the p_T of the muon be greater than $15 \text{ GeV}/c$.

ptVisCutsCompareMasses)

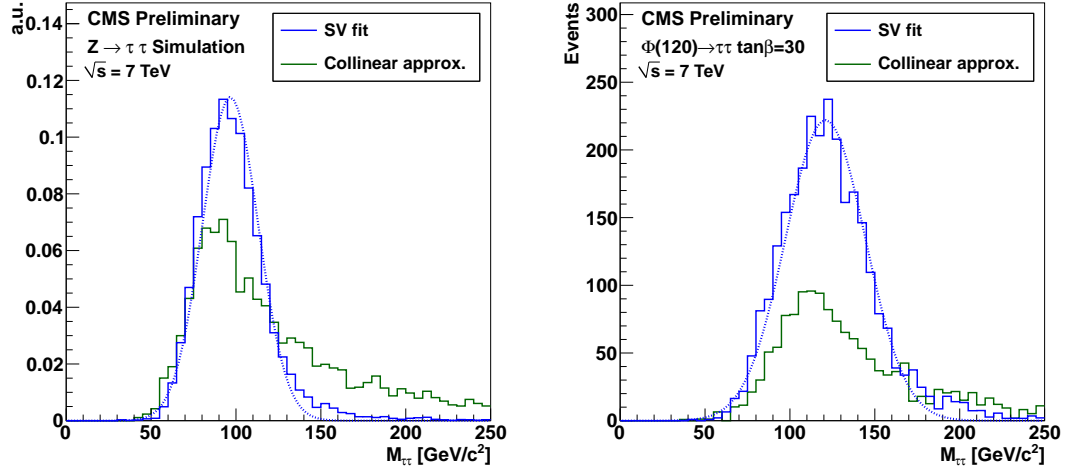


Figure 4.5: Comparison of the reconstructed tau pair mass spectrum in $Z \rightarrow \tau^+\tau^-$ (left) and MSSM $H(120) \rightarrow \tau^+\tau^-$ (right) events after the selections described in chapter 5. The mass spectrum reconstructed by the Secondary Vertex fit is shown in blue, the result of the collinear approximation algorithm is given in green. In the left plot, both distributions are normalized to unity, illustrating the improvement in resolution (shape) provided by the SVfit. In the right plot, the distributions are normalized to an (arbitrary) luminosity, illustrating the loss of events that occurs due to unphysical solutions in the application of the collinear approximation.

(fig:SVversusCollinear)

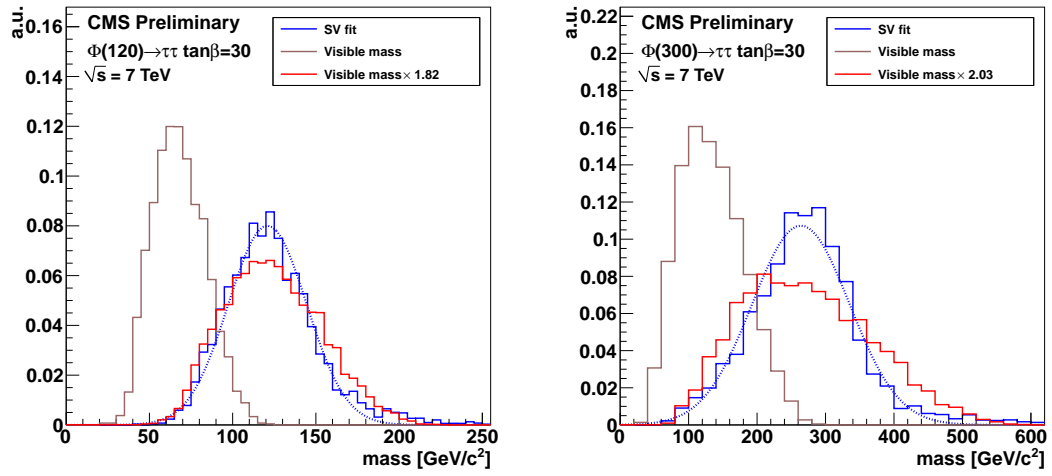


Figure 4.6: Comparison of the invariant mass of the muon and τ_{jet} (the “visible mass”) with the full $\tau^+\tau^-$ mass reconstructed by the SVfit. The spectrum is shown for two simulated MSSM Higgs samples, with $m_{A^0} = 120 \text{ GeV}/c^2$ (left), and $m_{A^0} = 200 \text{ GeV}/c^2$ (right). To illustrate that relative resolution of the SVfit is superior to that of the visible mass, the visible mass is also shown scaled up such that the mean of the two distributions are identical.

(fig:SVversusVis)

Chapter 5

Analysis Selections

⟨ch:selections⟩

§5.1 Particle Identification

§5.1.1 Muons

⟨sec:MuonId⟩

Muon candidates are required to be reconstructed as global and as tracker muons, meaning that a full track is reconstructed in the muon system and is well matched to a track in the silicon strip and pixel trackers. Additionally, they are required to pass the “Vector Boson Task Force” (VBTF) muon identification criteria developed for the $Z \rightarrow \mu^+ \mu^-$ cross-section measurement [43]:

- ≥ 1 Pixel hits
- ≥ 10 hits in silicon Pixel + Strip detectors
- ≥ 1 hit(s) in muon system
- ≥ 2 matched segments
- $\chi^2/DoF < 10$ for global track fit
- transverse impact parameter of “inner” track $d_{IP} < 2$ mm with respect to beam-spot

In order to reduce background contributions from muons originating from heavy quark decays in QCD multi-jet events, muons are required to be isolated. Isolation is computed as the p_T sum of charged and neutral hadrons plus photons reconstructed by the CMS particle-flow algorithm [27] within a cone of size $\Delta R_{iso} = 0.4$ around the muon direction. The innermost region of size $\Delta R_{veto} = 0.08$ (0.05) is excluded from the computation of

the isolation p_T sum with respect to neutral hadrons (photons), in order to avoid energy deposits in the electromagnetic and hadronic calorimeters which are due to the muon to enter the sum. In order to reduce pile-up effects, particles entering the isolation p_T sum are required to have transverse momenta $p_T > 1.0$ GeV/ c . Charged particles are additionally required to originate from the same vertex as the muon. The muons are required to be isolated with respect to charged hadrons of $p_T > 1.0$ GeV/ c and photons of $p_T > 1.5$ GeV/ c as reconstructed by the particle-flow algorithm [27] in a cone of size $\Delta R = 0.4$ around the direction of the muon.

§5.1.2 Hadronic Taus

Hadronic decays of taus are identified by the HPS + TaNC hybrid algorithm described in Section 3.5. The “medium” working point is used, corresponding to an expected QCD fake-rate of about 1%. $Z \rightarrow \mu^+\mu^-$ background contributions are largely due to muons which failed to get reconstructed as global muons (thus failing the muon identification requirement) and are misidentified as tau-jet candidates. These muons are typically isolated and have a large chance to pass the hadronic tau ID discriminators. To reject these events, hadronic taus are additionally required to pass an anti-muon veto described in Section 3.6.

§5.1.3 Missing Transverse Energy

The missing transverse energy E_T^{miss} , in the event is reconstructed based on the vectorial momentum sum of particle candidates reconstructed by the particle-flow algorithm [27, 44]. In the ideal case, the E_T^{miss} corresponds to the vector sum of the transverse components of all neutrinos in the event. The E_T^{miss} resolution in simulated $Z \rightarrow \mu^+\mu^-$ events is found to be smaller (better) than in the data. The reconstructed E_T^{miss} in the simulated events is “smeared” by a correction factor such that the data and simulation are in agreement. The “Z-recoil” E_T^{miss} correction procedure is described in Section 7.4.

§5.2 Event Selections

The selections applied to the analysis are designed to reject large fractions of the background while maintaining a high efficiency for identifying signal (Higgs) events. The backgrounds

Background	Cross Section (pb)
QCD Heavy Flavor	84679 ²
$W \rightarrow \mu\nu + \text{jets}$	10435
$Z \rightarrow \mu\mu + \text{jets}$	1666
$t\bar{t} + \text{jets}$	158

Table 5.1: The different backgrounds to the analysis presented in this thesis that include misidentified hadronic taus.

can be divided into two classifications: “fake” backgrounds, in which there is at least one misidentified hadronic tau decay, and the irreducible $Z \rightarrow \tau^+\tau^-$ background, which cannot¹ be distinguished from the potential presence of a Higgs boson of the same mass. Strategies for dealing with the irreducible Z background will be discussed in the Chapter 9. The different fake backgrounds, their cross section, and the basic removal strategies are outlined in Table 5.1.

Events in the muon plus tau-jet channel are selected by requiring a muon of $p_T^\mu > 15 \text{ GeV}/c$ within $|\eta_\mu| < 2.1$ and a tau-jet candidate of $p_T^{\tau\text{-jet}} > 20 \text{ GeV}/c$ within $|\eta_{\tau\text{-jet}}| < 2.3$. The η requirement on the muon ensures that it is within the fiducial region of the muon trigger system. The η requirement on the hadronic tau ensures it is well within the fiducial region of the tracker ($|\eta| < 2.5$) and minimizes exposure to large QCD backgrounds in the very forward region.

The muon and tau-jet candidate are required to be of opposite charge, as the Higgs is neutral and charge is conserved. The muon is required to be pass the identification criteria described in Section 5.1.1. The tau-jet candidate is required to pass the “medium” TaNC tau identification discriminator.

Additional event selection criteria are applied to reduce contributions of specific background processes. In order to reject this background, a dedicated discriminator against muons is applied [26]. Remaining muon background is suppressed by rejecting events which

¹Due to the differences in spin between the Z (spin 1) and the Higgs (spin 0), it maybe be possible to separate the two using spin correlations of the two tau decays.

FixMe: is
it really
medium??

Requirement	
Trigger	HLT_Mu9 for MC <i>cf.</i> table 5.3 for Data
Vertex	reconstructed with beam-spot constraint: $-24 < z_{vtx} < +24$ cm, $ \rho < 2$ cm, $N_{\text{DOF}} > 4$
Muon	reconstructed as global Muon with: $p_T > 15$ GeV, $ \eta < 2.1$, VBTF Muon ID passed, isolated within $\Delta R = 0.4$ cone with respect to charged hadrons of $p_T > 1.0$ GeV and neutral electromagnetic objects of $p_T > 1.5$ GeV
Tau-jet Candidate	reconstructed by HPS + TaNC combined Tau ID algorithm TaNC “medium” Tau ID discriminator and discriminators against electrons and muons passed, calorimeter muon rejection passed
Muon + Tau-jet	$\text{charge}(\text{Muon}) + \text{charge}(\text{Tau-jet}) = 0$, $\Delta R(\text{Muon}, \text{Tau-jet}) > 0.5$
Kinematics	$M_T(\text{Muon-MET}) < 40$ GeV $P_\zeta - 1.5 \cdot P_\zeta^{\text{vis}} > -20$ GeV

Table 5.2: Event selection criteria applied in the muon + tau-jet channel.

HtoMuTauEventSelection)

1470 have a track of $p_T > 15$ GeV and for which the sum of energy deposits in ECAL plus
1471 HCAL is below $0.25 \cdot P$ within a cylinder of radius 15 cm(ECAL) and 25 cm(HCAL),
1472 respectively. The $t\bar{t}$ and W +jets backgrounds are suppressed by cuts on the transverse mass
1473 of the $\mu - E_T^{\text{miss}}$ system and the P_ζ variable. Contamination from $Z \rightarrow \tau^+\tau^-$ events in
1474 which the reconstructed tau-jet candidate is due to a $\tau \rightarrow e\nu\nu$ decay is reduced by applying
1475 a dedicated tau ID discriminator against electrons.

1476 The complete set of event selection criteria applied in the muon + tau-jet channel are
1477 summarized in table 5.2.

1478 The events are triggered by a combination of muon and muon + tau-jet “cross-channel”
1479 triggers. For the muon triggers, paths with lowest P_T thresholds are used as long as the path

Trigger path	run-range
HLT_Mu9	132440 - 147116
HLT_IsoMu9	147196 - 148058
HLT_Mu11	147196 - 148058
HLT_Mu15	147196 - 149442
HLT_IsoMu13	148822 - 149182
HLT_IsoMu9_PFTau15	148822 - 149182
HLT_Mu11_PFTau15	148822 - 149182

Table 5.3: Muon and muon + tau-jet “cross-channel” trigger paths utilized to trigger events in the muon + tau-jet channel in different data-taking periods.

(tab:AHtoMuTauTriggers)

1480 remained unscaled (see Table 5.3). The muon + tau-jet “cross-channel” trigger paths
 1481 increase the trigger efficiency for events containing muons of transverse momenta close to
 1482 the $p_T^\mu > 15$ GeV/ c cut threshold. The trigger efficiency is measured in data via the tag-and-
 1483 probe technique. Details of the muon trigger efficiency measurement are given in Section 7.1
 1484 of the appendix. Monte Carlo simulated events are required to pass the HLT_Mu9 trigger
 1485 path. Weights are applied to simulated events to account for the difference between the sim-
 1486 ulated HLT_Mu9 efficiency and the combined efficiency of the set HLT_Mu9, HLT_IsoMu9,
 1487 HLT_Mu11, HLT_IsoMu13, HLT_Mu15, HLT_IsoMu9_PFTau15 and HLT_Mu11_PFTau15
 1488 used to trigger the data.

Chapter 6

Data–Driven Background Estimation

(ch:backgrounds)

For the result of this analysis to be reliable, it is of paramount importance that the backgrounds be well understood. The CMS experiment has adopted a policy that if possible, all background processes should be measured in a “data-driven” way. By requiring that the background comes from data, biases due to incorrectly modeling the background processes in simulation can be minimized or eliminated. In general, the data-driven methods also have the advantage that they are independent of the uncertainty on the integrated luminosity. This analysis measures the backgrounds using two complementary methods, the “Template Method” and the “Fake-rate method.” In both cases, predictions are made about backgrounds in the signal region using measurements obtained in background enriched control regions of the data. The Template Method fits the sum of background shape templates to the M_{vis} spectrum of events selected in the final analysis and is described in Section 6.3. The Fake-rate Method is based on applying probabilities for quark and gluon jets to be misidentified as hadronic tau decays to events passing all event selection criteria except the tau identification requirements. The probabilities with which jets fake hadronic tau signatures are measured in data. Contrary to the Template Method, The Fake-rate Method estimates the sum of the contributions of backgrounds that contain incorrectly identified taus. The Fake-rate method is detailed in Section 6.2. The two methods are complementary as the Template Method uses only information about the different visible mass distribution shapes of the backgrounds, while the Fake-rate method uses only information about the hadronic tau fake-rate.

§6.1 Background Enriched Control Regions

The criteria applied to select events in the background enriched control regions for the Template Method is based on the work described in [45]. With respect to that work, the muon isolation criteria applied to select $Z \rightarrow \mu^+\mu^-$, $W + \text{jets}$, $t\bar{t} + \text{jets}$ and QCD background enriched control samples has been changed to relative isolation with respect to charged hadrons and neutral electromagnetic objects reconstructed by the particle-flow algorithm. The selection of the enriched backgrounds is accomplished by disabling or inverting specific selections of Chapter 5 that were implemented to reject the given background. The selection of control regions used to measure the fake-rates for different types of background processes are very similar to the selections used for the Template Method. The details of the fake-rate measurement selections may be found in [46].

All control regions are selected from the 2010 CMS muon primary datasets using single muon HLT trigger paths. The set of triggers and run-ranges used to select events in the background enriched control samples is the same as for the analysis (see Table 5.3). The Monte Carlo simulated events used for comparison with the control region selections are required to pass the HLT_Mu9 trigger path and are weighted according to the description in Chapter 7 to account for the difference in efficiency between HLT_Mu9 and the trigger paths required to have passed in the data.

QCD di-jet events containing a muon (originating from the leptonic decay of a b or c quark) are selected by applying an *anti*-isolation requirement on the jet containing a muon. $W + \text{jets}$ and $t\bar{t} + \text{jets}$ are selected by requiring an isolated muon, and inverting the transverse mass (M_T) and P_ζ selections. Tau-jet candidates considered in the $Z \rightarrow \mu^+\mu^-$ sample where the reconstructed tau-jet candidate is faked by a misidentified muon and in the $t\bar{t} + \text{jets}$ control sample are required to pass the “loose” TaNC discriminator. For the Template Method, the $Z \rightarrow \mu^+\mu^-$ sample where the reconstructed tau-jet candidate is faked by a misidentified quark or gluon jet, the $W + \text{jets}$ and the QCD enriched control samples have a loose hadronic tau “preselection” applied. The tau-jet candidates are required to pass the “very loose”, but fail the “loose” TaNC discriminator. The criteria applied to select events in the different background enriched control samples are summarized in Table 6.1. The goal

Requirement	Enriched background process				
	$Z \rightarrow \mu^+ \mu^-$				
	Muon fake	Jet fake	$W + \text{jets}$	$t\bar{t} + \text{jets}$	QCD
Muon rel. iso.	< 0.15	< 0.1	< 0.1	< 0.1	$> 0.10 \ \&\& \ < 0.30$
Muon Track IP	-	-	-	-	-
Tau TaNC discr.	-	1	1	medium passed	1
Tau 1 3-Prong	-	-	-	-	-
Charge(Tau) = ± 1	-	-	-	-	-
Tau μ -Veto	inverted	applied	applied	applied	applied
Charge(Muon+Tau)	applied	-	-	applied	-
$M_T(\text{Muon-MET})$	-	$< 40 \text{ GeV}$	-	-	$< 40 \text{ GeV}$
$P_\zeta - 1.5 \cdot P_\zeta^{vis}$	$> -20 \text{ GeV}$	-	-	-	$> -20 \text{ GeV}$
global Muons	< 2	-	< 2	< 2	< 2
central Jet Veto	-	-	2	-	-
b-Tagging	-	-	-	3	-

¹ vlose passed && loose failed ² no Jets of $E_T > 20 \text{ GeV}$ within $|\eta| < 2.1$ (other than the τ -jet candidate)

³ min. two Jets of $E_T > 40 \text{ GeV}$, at least one of which with $E_T > 60 \text{ GeV}$ and at least of which with “TrackCountingHighEff” discriminator > 2.5

Table 6.1: Criteria to select events in different background enriched control samples. Hyphens indicate event selection criteria which are not applied.

MuTauBgControlRegions)

1540 of the background enriched selection process is to select different background processes with
 1541 high purity. A highly pure background control sample improves the stability of inferences
 1542 about the signal region made using information in the enriched control region. The purity
 1543 of the control regions (estimated using simulation) are summarized in Table 6.2.

1544 The number of events observed in the different control samples is compared to the
 1545 Monte Carlo expectation in table 6.2. Except for the contribution of $Z \rightarrow \mu^+ \mu^-$ events
 1546 in which the reconstructed tau-jet candidate is due to a misidentified quark or gluon jet,
 1547 good agreement between data and Monte Carlo simulation is observed. Differences observed
 1548 between data and simulation will be accounted for as systematic uncertainties.

1549 The distributions of visible and “full” $\tau^+ \tau^-$ invariant mass reconstructed by the SVfit
 1550 algorithm (see Chapter 4) observed in the background enriched control regions is compared

Enriched Selection	Contribution from							Purity
	Data	Σ SM	$Z \rightarrow \tau^+\tau^-$	$Z \rightarrow \mu^+\mu^-$	$W + \text{jets}$	$t\bar{t} + \text{jets}$	QCD	
$Z \rightarrow \mu^+\mu^-$								
Muon fake	15156	17109.8	331.6	16586.6	55.1	80.4	35.0	96.9%
Jet fake	85	62.7	2.5	55.5	0.5	1.4	2.4	88.5%
$W + \text{jets}$	514	642.4	17.9	22.9	581.7	0.8	16.7	90.6%
$t\bar{t} + \text{jets}$	26	39.7	0.7	< 0.1	0.6	38.4	< 1.0	96.7%
QCD	2510	2571.8	16.6	0.8	9.3	1.6	2543.4	98.9%

Table 6.2: Number of events observed in the different background enriched control samples compared to Monte Carlo expectations. Σ SM denotes the sum of $Z \rightarrow \tau^+\tau^-$, $Z \rightarrow \mu^+\mu^-$, $W + \text{jets}$, $t\bar{t} + \text{jets}$ and QCD processes. The expected purity of each control sample is computed as the ratio of contribution of the enriched process to Σ SM.

to the Monte Carlo simulation in Figures 6.1 and 6.2. The template for the $W + \text{jets}$ background has been corrected for the bias on the $M_{vis}^{\mu\tau had}$ shape caused by the $M_T^{\mu E_T^{miss}} < 50 \text{ GeV}/c^2$ and $P_\zeta - 1.5 \cdot P_\zeta^{vis} > -20 \text{ GeV}$ requirements applied in the final analysis via the reweighting procedure described in [45]. In the $t\bar{t} + \text{jets}$ enriched control region a peak at the Z mass is observed in data, which is not modeled by the Monte Carlo samples considered. The peak could be due to $Z \rightarrow \mu^+\mu^-$ events produced in association with b quarks. On the other hand, the contribution from $t\bar{t} + \text{jets}$ events to that sample seems to be overestimated. The origin of the Z mass peak merits further investigation, but overall the $t\bar{t} + \text{jets}$ is a negligible background contribution.

§6.2 The Fake-rate Method

The probabilities with which quark and gluon jets get misidentified as tau-jets may be utilized to obtain an estimate of background contributions in physics analyses. As an illustrative example and in order to demonstrate the precision achievable with the method, we introduce the method in the context of a “closure test,” using a simulated samples, a simple method of computing the fake-rate, and a simpler¹ hadronic tau identification algorithm. The closure test demonstrates that the method is self-consistent, and that the

¹The closure test uses the “shrinking cone” tau identification algorithm, which is described briefly in Section 3.1. A full description can be found in [26].

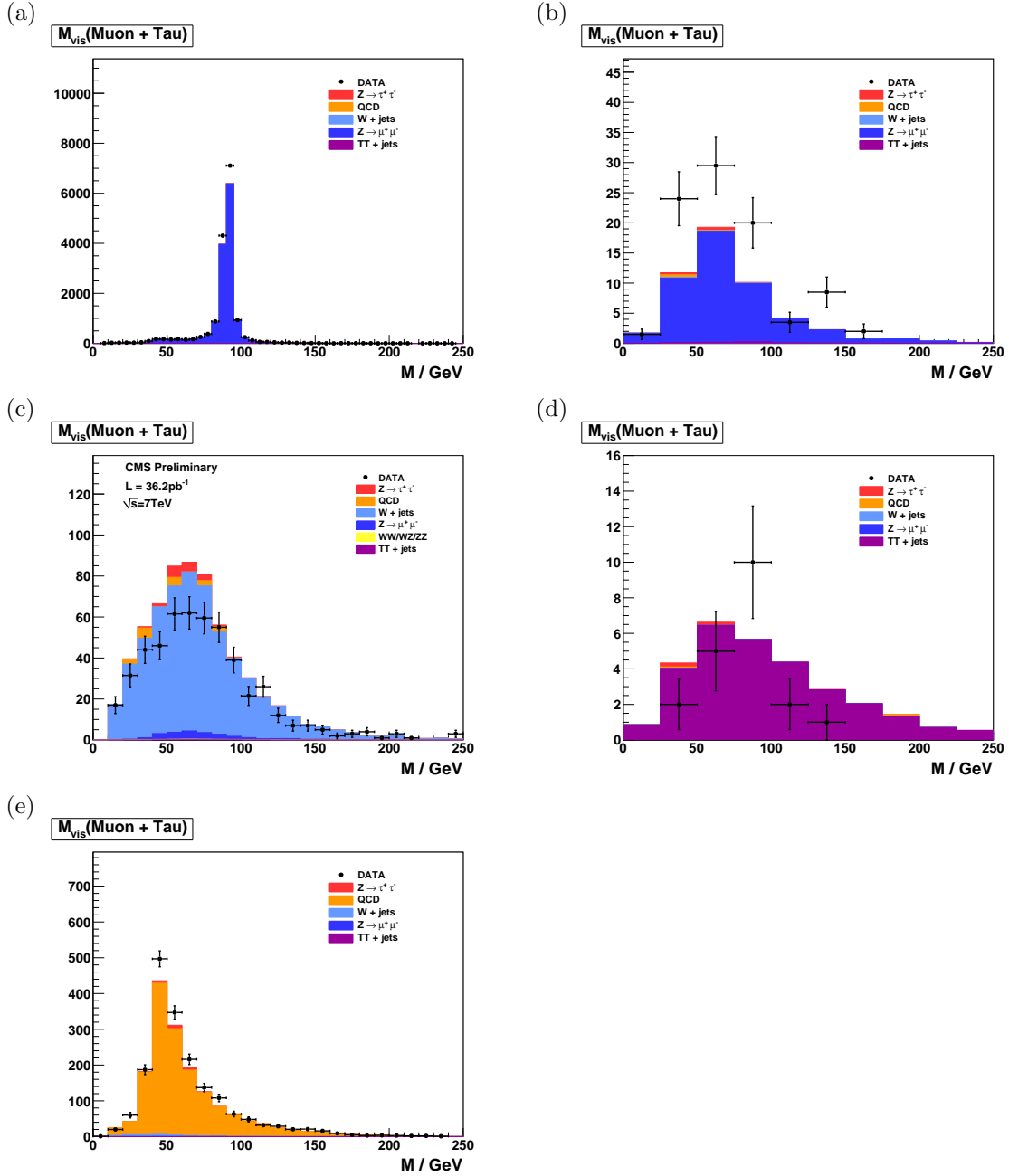


Figure 6.1: Distribution of visible mass of muon plus the tau-jet candidate reconstructed in the background enriched control samples for $Z \rightarrow \mu^+ \mu^-$ (a) and (b), $W + \text{jets}$ (c), $t\bar{t} + \text{jets}$ (d) and QCD multi-jet (e) backgrounds. In (a) reconstructed tau-jet candidates are expected to be dominantly due to misidentified muons, while in (b) they are expected to be mostly due to misidentified misidentified quark or gluon jets.

MuTauBgControlRegions)

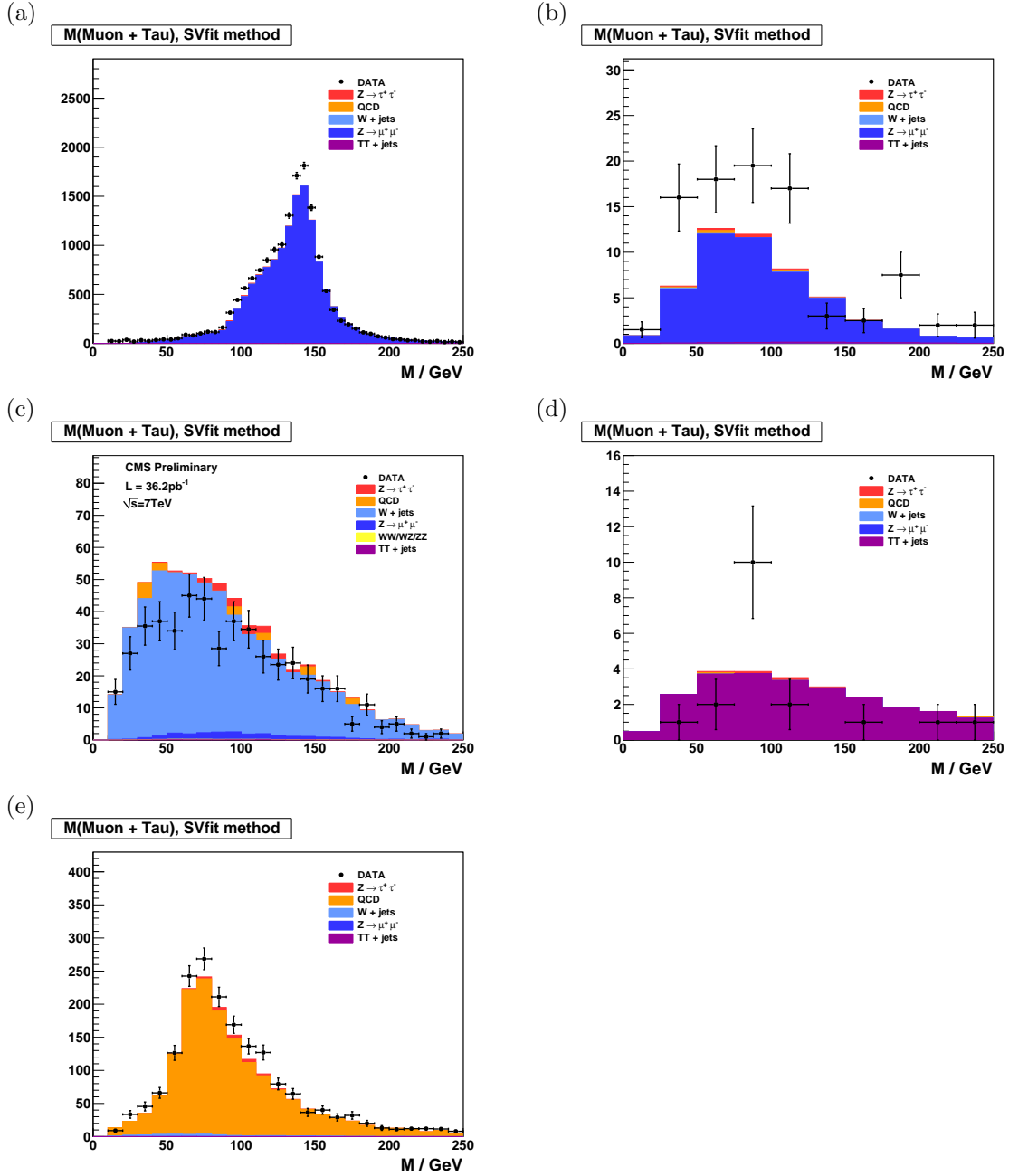


Figure 6.2: Distribution of “full” invariant mass reconstructed by the SVfit algorithm in the background enriched control samples for $Z \rightarrow \mu^+ \mu^-$ (a) and (b), $W + \text{jets}$ (c), $t\bar{t} + \text{jets}$ (d) and QCD multi-jet (e) backgrounds. In (a) reconstructed tau-jet candidates are expected to be dominantly due to misidentified muons, while in (b) they are expected to be mostly due to misidentified misidentified quark or gluon jets.

MuTauBgControlRegions)

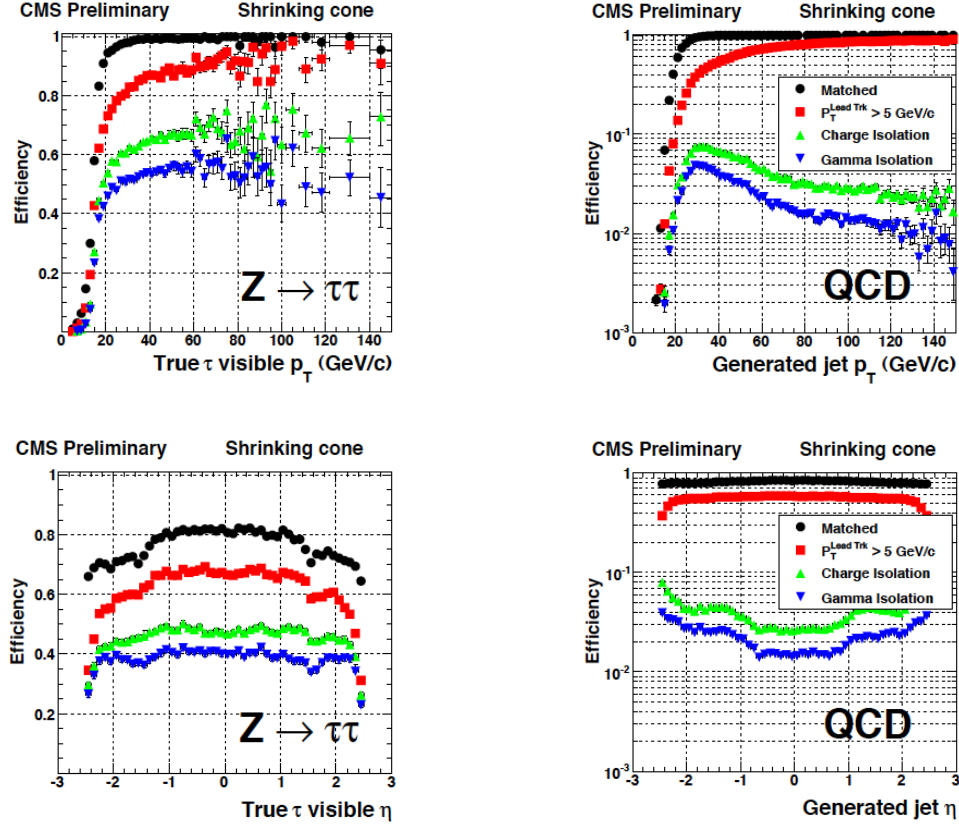


Figure 6.3: Cumulative efficiencies (left) and fake-rates (right) of successively applied tau identification cuts of the “shrinking signal cone” particle-flow based tau identification algorithm described in [26] as function of p_T^{jet} (top) and η^{jet} (bottom) of tau-jet candidates. The efficiencies/fake-rates for the complete set of tau identification criteria are represented by the blue (downwards facing) triangles.

EfficienciesAndFakeRates)

fake-rate technique can be used to estimate the contributions of QCD, $W + \text{jets}$, $t\bar{t} + \text{jets}$ and $Z \rightarrow \mu^+\mu^-$ backgrounds. The analysis selections used in the closure test are almost identical to the selections used in this analysis. Exact details of the selections can be found in reference analysis [43]. The method is then extended to use fake-rates measured in data, a multivariate method of computing the fake-rates, and the HPS + TaNC tau identification algorithm used in this analysis.

§6.2.1 Parameterization of Fake-rates

FakeRateParametrization)

Efficiencies and fake-rates of the tau identification algorithm based on requiring no tracks of $p_T > 1 \text{ GeV}/c$ and ECAL energy deposits of $p_T > 1.5 \text{ GeV}/c$ reconstructed within

1576 an “isolation cone” of size $\Delta R_{iso} = 0.5$ and outside of a “shrinking signal cone” of size
 1577 $\Delta R_{sig} = 5.0/E_T$ as it is used in the $Z \rightarrow \tau^+\tau^- \rightarrow \mu + \tau\text{-jet}$ analysis [43] are displayed
 1578 in Figure 6.3. In order to account for the visible p_T and η dependence, we parametrize
 1579 the fake-rates in bins of transverse momentum and pseudo-rapidity. As we will show in
 1580 section 6.2.3, the parametrization of the fake-rates by p_T and η makes it possible to not
 1581 only estimate the total number of background events contributing to physics analyses, but
 1582 to model the distributions of kinematic observables with a precision that is sufficient to
 1583 extract information on the background shape.

We add a third quantity, the E_T -weighted jet-width R_{jet} , to the parametrization in order to account for differences between the fake-rates of quark and gluon jets, which on average have differing widths and different fake-rates. The jet width quantity R_{jet} is defined as

$$R_{jet} = \sqrt{E(\eta^2) + E(\phi^2)}$$

1584 where $E(\eta^2)$, $E(\phi^2)$ is the second η , ϕ moment of the jet constituents, weighted by con-
 1585 stituent transverse energy. Analyses performed by the CDF collaboration [39, 47, 48] found
 1586 that systematic uncertainties on background estimates obtained from the fake-rate method
 1587 are reduced in case differences between quark and gluon jets are accounted for in this way.

1588 §6.2.2 Measurement of Fake-rates

Efficiencies and fake-rates are obtained by counting the fraction of tau-jet candidates passing all tau identification cuts and discriminators in a given bin² of p_T^{jet} , η_{jet} and R_{jet} :

$$P_{fr} \left(p_T^{jet}, \eta_{jet}, R_{jet} \right) := \frac{N_{jets} \left(p_T^{jet}, \eta_{jet}, R_{jet} | \text{tau ID passed} \right)}{N_{jets} \left(p_T^{jet}, \eta_{jet}, R_{jet} | \text{preselection passed} \right)} \quad (6.1) \quad \boxed{\text{eqBgEstFakeRate}}$$

1589 The pre-selection in the denominator of equation 6.1 in general refers to p_T and η cuts,
 1590 which are applied with thresholds matching those applied on the final analysis level, but
 1591 may include loose tau identification criteria (which may be applied e.g. already during event
 1592 skimming). It is critical that the selection used in the denominator be identical to that of
 1593 the final analysis to ensure the fake-rates are not biased by different selections.

²The example presented in the closure tests bins the fake-rate calculation in bins of the parameterization variables. In Section 6.2.6 we describe a more robust multivariate method to compute the fake-rates.

1594 Different sets of fake-rates are determined for the highest p_T and for the second highest
 1595 p_T jet in QCD di-jet events, for jets in a QCD event sample enriched by the contribution
 1596 of heavy quarks and gluons by requiring the presence of a muon reconstructed in the final
 1597 state, and for jets in “electroweak” events selected by requiring a W boson in the final state.

1598 §6.2.3 Application of Fake-rates

(sec:FakeRateApplication)

1599 Knowledge of the tau identification efficiencies and fake-rates as function of the parameters
 1600 p_T^{jet} , η_{jet} and R_{jet} as defined by equation 6.1 is utilized to obtain an estimate for the contri-
 1601 butions of background processes to physics analyses involving tau lepton hadronic decays
 1602 in the final state. The basic idea is to replace tau identification cuts and discriminators by
 1603 appropriately chosen weights.

1604 Application of the fake-rate technique consists of two stages. The first stage consists of
 1605 loosening the tau identification cuts and discriminators and applying only the preselection
 1606 requirements defined by the denominator of Equation 6.1, in order to obtain an event
 1607 sample dominated by contributions of background processes. After disabling the selections
 1608 on hadronic tau identification, the relative contributions of the backgrounds are expected
 1609 to increase by the inverse of the (average) fake-rate, typically by a factor $\mathcal{O}(100)$. In the
 1610 second stage, weights are applied to all events in the background dominated control sample,
 1611 according to the probabilities $P_{fr}(p_T^{jet}, \eta_{jet}, R_{jet})$ for jets to fake the signature of a hadronic
 1612 tau decay. After application of the weights, an estimate for the total number of background
 1613 events passing the tau identification cuts and discriminators and thus contributing to the
 1614 final analysis sample is obtained.

1615 The fake-rate technique works best if all background contributions to the analysis arise
 1616 from misidentification of quark and gluon jets as hadronic tau decays. Corrections to the
 1617 estimate obtained from the fake-rate technique are needed in case of background processes
 1618 contributing to the final analysis sample which either produce genuine tau leptons in the
 1619 final state (e.g. $t\bar{t} + \text{jets}$) or in which tau-jet candidates are due to misidentified electrons
 1620 or muons (e.g. $Z \rightarrow \mu^+\mu^-$, $Z \rightarrow e^+e^-$), as the latter may fake signatures of hadronic tau
 1621 decays with very different probabilities than quark and gluon jets.

1622 In the “simple” fake-rate method described in detail in the next section, the correc-
 1623 tions are taken from Monte Carlo simulations. Corrections based on Monte Carlo are needed
 1624 also to compensate for signal contributions to the background dominated control sample.
 1625 An alternative to Monte Carlo based corrections is to utilize additional information con-
 1626 tained in the background dominated control sample. The modified version is described in
 1627 section 6.2.5. It has been used to estimate background contributions in searches for Higgs
 1628 boson production with subsequent decays into tau lepton pairs performed by the CDF col-
 1629 laboration in TeVatron Run II data [39, 47, 48]. We will refer to the modified version as
 1630 “CDF-type” method in the following.

1631 §6.2.4 “Simple” weight method

In the “simple” method all tau-jet candidates within the background dominated event sample are weighted by the probabilities of quark and gluon jets to fake the signature of a hadronic tau decay:

$$w_{jet}^{simple} \left(p_T^{jet}, \eta_{jet}, R_{jet} \right) := P_{fr} \left(p_T^{jet}, \eta_{jet}, R_{jet} \right) \quad (6.2) \quad \text{eqBgEstFakeRate}$$

1632 These weights are applied to all jets in the background dominated control sample which
 1633 pass the preselection defined by the denominator of Equation 6.1. Note that the weights
 1634 defined by Equation 6.2 can be used to estimate the contributions of background processes
 1635 to distributions of tau-jet related observables. They cannot be used as event weights.

In order to compare distributions of event level quantities or per-particle quantities for particles of types different from tau leptons decaying hadronically, event weights need to be defined. Neglecting the small fraction of background events in which multiple tau-jet candidates pass the complete set of all tau identification cuts and discriminators, event weights can be computed by summing up the per-jet weights defined by Equation 6.2 over all tau-jet candidates in the event which pass the preselection:

$$W_{event}^{simple} := \sum w_{jet}^{simple} \quad (6.3) \quad \text{eqBgEstFakeRate}$$

A bit of care is needed in case one wants to compare distributions of observables related to “composite particles” the multiplicity of which depends on the multiplicity of tau-jet candidates in the event (e.g. combinations of muon + tau-jet pairs in case of the $Z \rightarrow \tau^+ \tau^- \rightarrow \mu + \tau$ -jet analysis). Per-particle weights need to be computed for such

Background Process	Expectation	Estimate obtained by applying weights of type:				Average fake-rate estimate
		QCD lead jet	QCD second jet	QCD μ -enriched	W + jets	
W +jets	163.0 ± 7.1	157.2 ± 2.8	140.9 ± 2.7	129.9 ± 2.5	177.9 ± 3.2	$151.5^{+26.6}_{-21.8}$
QCD	246.4 ± 31.8	269.2 ± 14.0	246.5 ± 14.3	219.7 ± 11.8	300.8 ± 15.2	$259.1^{+44.9}_{-41.7}$
$t\bar{t}$ +jets	12.2 ± 0.6	14.3 ± 0.3	12.6 ± 0.3	11.6 ± 0.3	16.5 ± 0.3	$13.8^{+2.7}_{-2.2}$
$Z \rightarrow \mu^+\mu^-$	68.6 ± 2.9	58.2 ± 1.3	51.2 ± 1.2	48.5 ± 1.1	65.8 ± 1.4	$55.9^{+10.0}_{-7.5}$
Σ Background	490.4 ± 32.7	499.9 ± 14.4	451.2 ± 14.6	409.7 ± 12.1	561.1 ± 15.6	$480.2^{+82.7}_{-71.9}$
$Z \rightarrow \tau^+\tau^-$	—	284.3 ± 3.7	269.0 ± 3.9	256.5 ± 3.3	325.3 ± 4.2	$283.3^{+42.2}_{-27.1}$

Table 6.3: Number of events from W +jets, QCD, $t\bar{t}$ +jets and $Z \rightarrow \mu^+\mu^-$ background processes expected to pass all selection criteria of the $Z \rightarrow \tau^+\tau^- \rightarrow \mu + \tau$ -jet cross-section analysis compared to the estimates obtained by weighting events in the background dominated control sample with the “simple” fake-rate weights defined by Equation 6.3.

FakeRate'frSimpleResults)

“composite particles”, depending on p_T^{jet} , η_{jet} , R_{jet} of its tau-jet candidate constituent, according to:

$$w_{comp-part}^{simple} \left(p_T^{jet}, \eta_{jet}, R_{jet} \right) := w_{jet}^{simple} \left(p_T^{jet}, \eta_{jet}, R_{jet} \right) \quad (6.4) \quad \boxed{\text{eqBgEstFakeRate}}$$

1636 Different estimates are obtained for the fake-rate probabilities determined for the high-
1637 est and second highest p_T jet in QCD di-jet events, jets in a muon enriched QCD sample
1638 and jets in W + jets events. The arithmetic average of the four estimates of the closure test
1639 together with the difference between the computed average and the minimum/maximum
1640 value is given in Table 6.3.

1641 We take the average value as “best” estimate of the background contribution and
1642 the difference between the average and the minimum/maximum estimate as its systematic
1643 uncertainty. We obtain a value of $\mathcal{O}(15\%)$ for the systematic uncertainty and find that
1644 the true sum of QCD, W + jets, $t\bar{t}$ + jets and $Z \rightarrow \mu^+\mu^-$ background contributions agrees
1645 well with the “best” estimate obtained by the fake-rate method within the systematic
1646 uncertainty.

1647 Note that the estimate for the sum of background contributions which one obtains

in case one applies the “simple” fake-rate weights defined by Equation 6.3 to a background dominated control sample selected in data is likely to overestimate the true value of background contributions by a significant amount. The reason is that contributions of $Z \rightarrow \tau^+\tau^-$ events with true taus are non-negligible. In fact, genuine tau contributions to the background dominated control sample are expected to be 14.9% and since the per-jet weights computed by Equation 6.2 are larger on average in signal than in background events, the signal contribution increases by the weighting and amounts to 37.1% of the sum of event weights computed by Equation 6.3 and given in Table 6.3.

The contribution of the $Z \rightarrow \tau^+\tau^-$ signal needs to be determined by Monte Carlo simulation and subtracted from the estimate obtained by applying the “simple” fake-rate method to data, in order to get an unbiased estimate of the true background contributions.

§6.2.5 “CDF-type” weights

Instead of subtracting from the estimate obtained for the sum of background contributions a correction determined by Monte Carlo simulation, the genuine tau contribution to the background dominated event sample selected in data can be corrected for by adjusting the weights, based solely on information contained in the analyzed data sample, avoiding the need to rely on Monte Carlo based corrections.

In the “CDF-type” method, additional information, namely whether or not tau-jet candidates pass or fail the tau identification cuts and discriminators, is drawn from the data. The desired cancellation of signal contributions is achieved by assigning negative weights to those tau-jet candidates which pass all tau identification cuts and discriminators, i.e. to a fair fraction of genuine hadronic tau decays, but to a small fraction of quark and gluon jets only. The small reduction of the background estimate by negative weights assigned to quark and gluon jets is accounted for by a small increase of the positive weights assigned to those tau-jet candidates for which at least one of the tau identification cuts or discriminators fails. In this way, an unbiased estimate of the background contribution is maintained.

To be specific, the “CDF-type” weights assigned to tau-jet candidates are computed

as:

$$w_{jet}^{CDF} \left(p_T^{jet}, \eta_{jet}, R_{jet} \right) := \begin{cases} \frac{P_{fr}(p_T^{jet}, \eta_{jet}, R_{jet}) \cdot \varepsilon(p_T^{jet}, \eta_{jet}, R_{jet})}{\varepsilon(p_T^{jet}, \eta_{jet}, R_{jet}) - P_{fr}(p_T^{jet}, \eta_{jet}, R_{jet})} & \text{all tau ID passed} \\ \frac{P_{fr}(p_T^{jet}, \eta_{jet}, R_{jet}) \cdot (1 - \varepsilon(p_T^{jet}, \eta_{jet}, R_{jet}))}{\varepsilon(p_T^{jet}, \eta_{jet}, R_{jet}) - P_{fr}(p_T^{jet}, \eta_{jet}, R_{jet})} & \text{otherwise} \end{cases} \quad (6.5) \quad \boxed{\text{eqBgEstFakeRate}}$$

1674 For the derivation of equation 6.5 for the “CDF-type” weights assigned to tau-jet candi-
 1675 dates, we will use the following notation: Let n_τ (n_{QCD}) denote the total number of tau-jets
 1676 (quark and gluon jets) in a certain bin of transverse momentum p_T^{jet} , pseudo-rapidity η_{jet}
 1677 and jet-width R_{jet} and n_τ^{sel} (n_{QCD}^{sel}) denote the number of tau-jets (quark and gluon jets)
 1678 in that bin which pass all tau identification cuts and discriminators. By definition of the
 1679 tau identification efficiency $\varepsilon := \varepsilon(p_T^{jet}, \eta_{jet}, R_{jet})$ and fake-rate $f := f(p_T^{jet}, \eta_{jet}, R_{jet})$:

$$\begin{aligned} n_\tau^{sel} &= \varepsilon \cdot n_\tau \\ n_{QCD}^{sel} &= f \cdot n_{QCD}. \end{aligned} \quad (6.6) \quad \boxed{\text{eqBgEstFakeRate}}$$

Depending on whether or not a given tau-jet candidate passes all tau identification cuts and discriminators or not, we will assign a weight of value w_{passed} or w_{failed} to it. The values of the weights w_{passed} and w_{failed} shall be adjusted such that they provide an unbiased estimate of the background contribution:

$$w_{passed} \cdot f \cdot n_{QCD} + w_{failed} \cdot (1 - f) \cdot n_{QCD} \equiv n_{QCD}^{sel} = f \cdot n_{QCD} \quad (6.7) \quad \boxed{\text{eqBgEstFakeRate}}$$

while averaging to zero for genuine hadronic tau decays:

$$w_{passed} \cdot \varepsilon \cdot n_\tau + w_{failed} \cdot (1 - \varepsilon) \cdot n_\tau \equiv 0.$$

The latter equation yields the relation:

$$w_{passed} = -\frac{1 - \varepsilon}{\varepsilon} \cdot w_{failed}, \quad (6.8) \quad \boxed{\text{eqBgEstFakeRate}}$$

1680 associating the two types of weights. By inserting relation 6.8 into equation 6.7 we obtain:

$$\begin{aligned} & -\frac{1 - \varepsilon}{\varepsilon} \cdot w_{failed} \cdot f \cdot n_{QCD} + w_{failed} \cdot (1 - f) \cdot n_{QCD} = f \cdot n_{QCD} \\ \Rightarrow & \left(\frac{-f + \varepsilon \cdot f + \varepsilon - f \cdot \varepsilon}{\varepsilon} \right) \cdot w_{failed} = f \\ \Rightarrow & w_{failed} = \frac{f \cdot \varepsilon}{\varepsilon - f} \end{aligned}$$

and

$$w_{passed} = -\frac{f \cdot (1 - \varepsilon)}{\varepsilon - f} \quad (6.9) \quad \boxed{\text{eqBgEstFakeRate}}$$

1681 which matches exactly equation 6.5 for the “CDF-type” weights applied to tau-jet candi-
 1682 dates given in section 6.2.5.

1683 Event weights and the weights assigned to “composite particles” are computed in the

Background Process	Expectation	Estimate obtained by applying weights of type:				Average fake-rate estimate
		QCD lead jet	QCD second jet	QCD μ -enriched	$W + \text{jets}$	
$W + \text{jets}$	163.0 ± 7.1	163.2 ± 3.8	140.6 ± 3.4	128.0 ± 3.1	188.3 ± 4.2	$155.0^{+33.6}_{-27.3}$
QCD	246.4 ± 31.8	300.5 ± 19.5	266.1 ± 19.0	236.0 ± 16.4	335.1 ± 20.4	$284.4^{+55.5}_{-52.0}$
$t\bar{t} + \text{jets}$	12.2 ± 0.6	13.1 ± 0.3	11.5 ± 0.3	10.2 ± 0.3	15.4 ± 0.4	$12.6^{+2.8}_{-2.4}$
$Z \rightarrow \mu^+ \mu^-$	68.6 ± 2.9	52.7 ± 1.4	46.7 ± 1.4	41.9 ± 1.2	60.3 ± 1.6	$50.4^{+10.1}_{-8.6}$
Σ Background	490.4 ± 32.7	529.5 ± 19.9	464.9 ± 19.3	416.1 ± 16.8	599.1 ± 20.9	$502.4^{+99.4}_{-88.4}$
$Z \rightarrow \tau^+ \tau^-$	—	0.3 ± 2.4	-10.6 ± 2.5	3.8 ± 2.0	-10.8 ± 2.8	$-4.3^{+8.4}_{-7.2}$

Table 6.4: Number of events from $W + \text{jets}$, QCD, $t\bar{t} + \text{jets}$ and $Z \rightarrow \mu^+ \mu^-$ background processes expected to pass all selection criteria of the closure test compared to the estimates obtained by weighting events in the background dominated control sample with the “CDF-type” fake-rate weights defined by equation 6.10.

1684 same way as for the “simple” weights, based on the weights assigned to the tau-jet candi-
1685 dates:

$$W_{event}^{CDF} := \Sigma w_{jet}^{CDF}$$

$$w_{comp-part}^{CDF} \left(p_T^{jet}, \eta_{jet}, R_{jet} \right) := w_{jet}^{CDF} \left(p_T^{jet}, \eta_{jet}, R_{jet} \right), \quad (6.10) \quad \text{eqBgEstFakeRate}$$

1686 where the sums extend over all jets in the background dominated control sample which pass
1687 the preselection defined by the denominator of equation 6.1.

1688 The effect of the negative weights to compensate the positive weights in case the “CDF-
1689 type” fake-rate method is applied to signal events containing genuine hadronic tau decays is
1690 shown in Table 6.4 and illustrated in Figure 6.4. As expected, positive and negative weights
1691 do indeed cancel in the statistical average.

1692 Figures 6.5, 6.6 and 6.7 demonstrate that an unbiased estimate of the background
1693 contribution by the “CDF-type” weights is maintained. Overall, the estimates obtained
1694 are in good agreement with the contributions expected for different background processes,
1695 indicating that the adjustment of negative and positive weights works as expected for the
1696 background as well.

1697 Results obtained by the “CDF-type” fake-rate method are summarized in table 6.4,

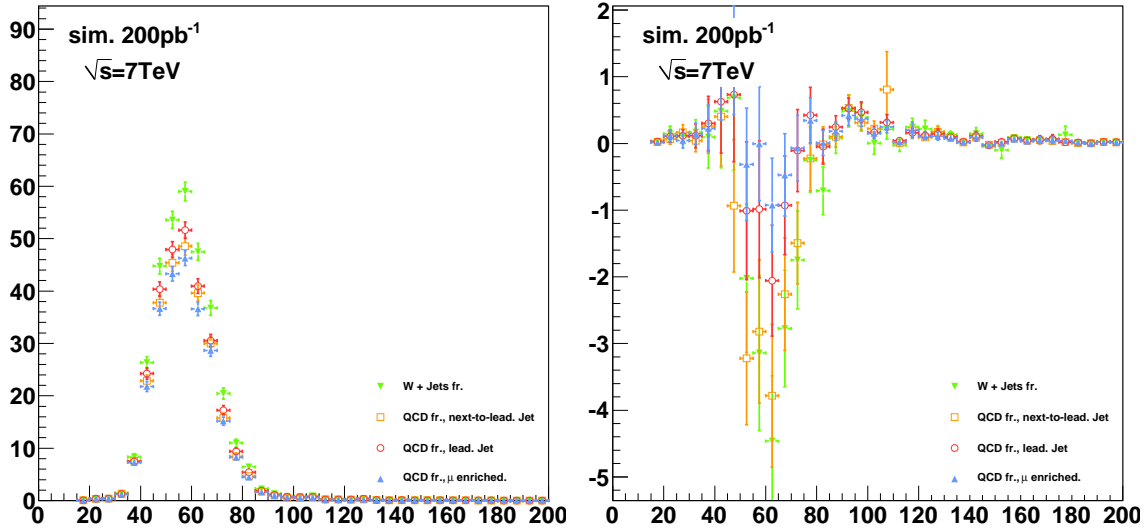


Figure 6.4: Distributions of visible invariant mass of muon plus tau-jet in $Z \rightarrow \tau^+\tau^-$ signal events weighted by “simple” weights computed according to Equation 6.4 (left) and “CDF-type” weights computed according to Equation 6.10 (right). The signal contribution to the background estimate computed by the “simple” method is non-negligible and needs to be corrected for. The “CDF-type” weights achieve a statistical cancellation of positive and negative weights, such that the total signal contribution averages to zero, avoiding the need for Monte Carlo based corrections.

peResults'mVisibleSignal)

1698 in which the total number of background events estimated by Equation 6.10 is compared
 1699 to the true background contributions. The “best” estimate of the background contribution
 1700 obtained from the “CDF-type” method is again taken as the arithmetic average of the
 1701 estimates obtained by applying the fake-rate probabilities for the highest and second highest
 1702 p_T jet in QCD di-jet events, jets in a muon enriched QCD sample and jets in W + jets events.
 1703 Systematic uncertainties are taken from the difference between the computed average value
 1704 and the minimum/maximum estimate. We obtain a value of $\mathcal{O}(15\text{--}20\%)$ for the systematic
 1705 uncertainty of the “CDF-type” method, slightly higher than the systematic uncertainty
 1706 obtained for the “simple” method. The small increase of systematic uncertainties is in
 1707 agreement with our expectation for fluctuations of the jet-weights in case weights of negative
 1708 and positive sign are used.

§6.2.6 k -Nearest Neighbor Fake-rate Calculation

(sec:KNN)

For the fake-rate method to give correct results, care must be taken that the measured fake-rate is well defined in all of the regions of phase space where it will be used. In the closure test described above, the computation of the fake-rate was accomplished by binning the numerator (tau ID passed) and denominator (tau ID passed and failed) distributions in the three dimensions of the parameterizations. This method has the disadvantage that the determination of the optimal binning is extremely difficult to determine, and that any bins with no entries in the denominator distribution caused the fake-rate to be undefined in those regions.

To overcome these problems, the fake-rate parameterization is implemented by adapting a multivariate technique known as a k -Nearest Neighbor classifier (k NN). A k NN classifier is typically used to classify events operates by populating (“training”) an n -dimensional space with signal and background events. The probability for a given point x in the space to be “signal-like” is determined by finding the k nearest neighbors and computing the ratio

$$p_{sig} = \frac{n_{sig}}{n_{sig} + n_{bkg}}, \quad (6.11) \quad \text{eq:KNNEquation}$$

where n_{sig}, n_{bkg} are the observed number of signal and background events, respectively. By construction, $k = n_{sig} + n_{bkg}$. The principle of operation is illustrated in Figure 6.8

The classification feature of a k NN can be trivially adapted to parameterize a fake-rate such that it is defined everywhere. Examining the form of Equation 6.11, it is clear that by replacing n_{sig} with n_{passed} and n_{bkg} with n_{failed} , the equation is equivalent to the tau-fake rate. We thus “train” the k NN with tau-candidates which pass the tau identification as signal events and those which fail as background events. The resulting classifier is a function which returns the expected fake-rate for any point in the space of the parameterization. The choice of k must be optimized. When k is low, the small number of neighbors causes large counting fluctuations in the fake rate. If k is too large, the k NN effectively averages over a large area of the space of the variables³. For the training statistics available in the 2010 data, $k = 20$ is found to be the optimal choice.

³In the limit $k \rightarrow \inf$, the k NN output reduces to a single number. In this extreme case, all information about the dependence of the fake-rate on the variables is lost.

§6.2.7 Results of Background Estimation

An independent estimate of the background contributions to the analysis presented in this thesis is obtained by applying the fake-rate method in a manner analogous to the closure test. Fake-rates in QCD multi-jet events (light quark enriched sample), QCD events containing muons (heavy quark and gluon enriched sample) and W + jets events are measured in data [32, 46] and applied to events which pass all the event selection criteria listed in table 5.2, with the exceptions of

- the “medium” HPS + TaNC discriminator, and
- the requirement that the tau have unit charge.

No assumption is made on the composition of $Z \rightarrow \mu^+\mu^-$, W + jets, $t\bar{t}$ + jets and QCD backgrounds contributing to the event sample selected by the analysis. Differences between fake-rates obtained for QCD multi-jet, QCD muon enriched and W + jets background events are attributed as systematic uncertainties of the fake-rate method. Per jet and per event weights have been computed by the “simple” and “CDF-type” weights as described in the closure test and the results are found to be compatible within statistical and systematic uncertainties. In the following, we present results for “CDF-type” weights. The “CDF-type” weights have the advantage that the background estimate obtained does not change, whether there is MSSM Higgs $\rightarrow \tau^+\tau^-$ signal present in the data or not.

Tau identification efficiencies need to be known when using “CDF-type” weights. Dedicated studies have checked the tau identification efficiencies in data [46]. Statistical and systematic uncertainties of these studies are still sizeable at present, in the order to 20–30%. No indication has been found, however, that the Monte Carlo simulation does not correctly model hadronic tau decays in data. For the purpose of computing fake-rate weights via the “CDF-type” method, tau identification efficiencies are taken from the Monte Carlo simulation of hadronic tau decays in $Z \rightarrow \tau^+\tau^-$ events. Systematic uncertainties on the background estimate obtained by the fake-rate method are determined by varying the tau identification efficiencies by $\pm 30\%$ relative to the value obtained from the Monte Carlo simulation.

Events weighted by:	Estimate
QCD lead jet	$202.1^{+14.9}_{-74.8}$
QCD second jet	$198.0^{+22.8}_{-79.3}$
QCD μ -enriched	$213.3^{+17.7}_{-82.6}$
W + jets	$232.8^{+21.1}_{-95.0}$
N_{bgr} estimate	$236.1^{+24.1}_{-65.9}$

Table 6.5: Estimate for background contributions obtained by weighting events passing all selection criteria listed in Table 5.2 except for the requirement for tau-jet candidates to pass the “medium” tight TaNC discriminator and have unit charge by fake-rates measured in QCD multi-jet, QCD muon enriched and W + jets data samples.

fuTauFakeRateResultsOS)

1758 The results of applying the fake-rate method to the mu + tau channel are summarized
 1759 in Table 6.5. The background prediction has been corrected for the expected⁴ contribution
 1760 of $13.1^{+2.8}_{-0.6}$ events from $Z \rightarrow \mu^+ \mu^-$ background events in which the reconstructed tau-jet is
 1761 due to a misidentified muon. The obtained estimate is in good agreement with the Monte
 1762 Carlo expectation.

1763 As an additional cross-check of the method, a sample of events containing a muon
 1764 plus a tau-jet of like-sign charge is selected in data and compared to the background
 1765 prediction obtained by applying the fake-rate method to the like-sign sample. The like-sign
 1766 sample is expected to be dominated by the contributions of W + jets and QCD background
 1767 processes and allows to verify the fake-rate method in a practically signal free event sample.
 1768 The background estimate obtained by the fake-rate method is compared to the number of
 1769 events observed in the like-sign data sample in Table 6.6. The number of events expected
 1770 in the like-sign control sample from Monte Carlo simulation is indicated in the caption. All
 1771 numbers are in good agreement.

1772 The fake-rate method does not only allow to estimate the total number of background
 1773 events, but allows to model the distributions of background processes as well. The capability
 1774 to model distributions is illustrated in Figure 6.9, which shows good agreement between the
 1775 distributions observed in the like-sign data sample and the predictions obtained by the

⁴The contribution of $Z \rightarrow \mu^+ \mu^-$ is estimated using a simulated sample.

Events weighted by:	Estimate
QCD lead jet	$191.7^{+2.3}_{-17.9}$
QCD second jet	$185.1^{+6.0}_{-21.1}$
QCD μ -enriched	$194.7^{+2.0}_{-20.5}$
W + jets	$208.9^{+0.5}_{-14.4}$
Fake-rate estimate	$201.8^{+14.2}_{-18.9}$
Observed	216

Table 6.6: Number of events observed in like-sign control region compared to estimate obtained by fake-rate method.

fake-rate method for the distributions of muon plus tau-jet visible mass and of the “full” invariant mass reconstructed by the SVfit algorithm.

FixMe: *THIS IS FROM THE HPS NOTE!*

§6.3 Template method

Shape templates for the $\mu + \tau_{had}$ visible mass M_{vis} are obtained from data, using a set of dedicated control regions which are chosen to select a high purity sample of one particular background process each. The number of events selected in each control region and comparisons to the predictions from Monte Carlo simulations are summarized in Table 6.2. The template M_{vis} shapes obtained from data in the background enriched control regions are compared to the signal region shapes obtained by Monte Carlo simulation in figure 6.10. The M_{vis} spectrum observed in the final analysis is fitted to the sum of these templates. Estimates for background yields are obtained from the normalization factor of each template, determined by the fit. Further details of the method can be found in [45] and [49].

The TaNC (Section 3.3, [38]) discriminators used in [49] are replaced by the corresponding discriminators of the HPS + TaNC algorithm (Section 3.5, [31]). The $Z/\gamma^* \rightarrow \tau^+\tau^-$ signal shape is obtained via the $Z/\gamma^* \rightarrow \mu^+\mu^-$ embedding technique [50]. The $\mu + \tau_{had}$ visible mass spectrum observed in the final analysis is compared to the sum of template shapes scaled by the normalization factors determined by the fit in Figure 6.11. The corresponding estimates for background contributions are summarized in Table 6.7.

Process	Estimate
$Z \rightarrow \mu^+ \mu^-$	
Muon fake	5.7 ± 6.0
Jet fake	< 14.5
$W + \text{jets } t\bar{t} + \text{jets}$	7.6 ± 6.9
QCD	141.3 ± 40.4
N_{bgr} estimate	226.5 ± 33.1

Table 6.7: Estimated contributions of individual background processes to the signal region, obtained via the template method. As the shapes are very similar, the normalization factors for QCD and $W + \text{jets}$ background processes are anti-correlated. As a consequence, the sum of background contributions is determined by the fit more precisely than the individual contributions.

ab:BgEstTemplateMethod)

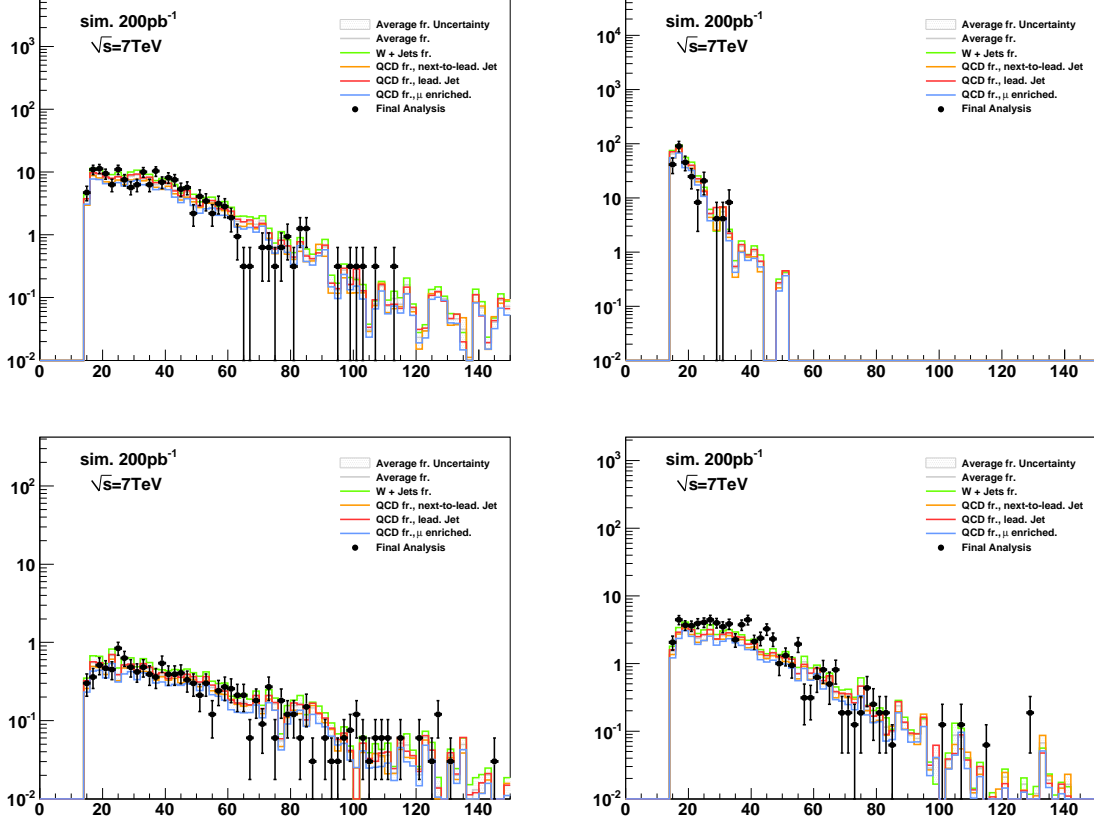


Figure 6.5: Distributions of muon transverse momentum in $W + \text{jets}$ (top left), QCD (top right), $t\bar{t} + \text{jets}$ (bottom left) and $Z \rightarrow \mu^+\mu^-$ (bottom right) background events which pass all selection criteria of the $Z \rightarrow \tau^+\tau^- \rightarrow \mu + \tau\text{-jet}$ cross-section analysis [43] compared to the estimate obtained from the “CDF method” fake-rate technique, computed according to equation 6.10. The expected contribution of background processes is indicated by points. Lines of different colors represent the estimates obtained by applying fake-rate weights determined for different compositions of light quark, heavy quark and gluon jets, as described in section 6.2.1. The maximum (minimum) estimate is interpreted as upper (lower) bound. The difference between the bounds is taken as systematic uncertainty on the estimate obtained from the “CDF-type” fake-rate method and is represented by the gray shaded area.

CDFtypeResults'muonPt)

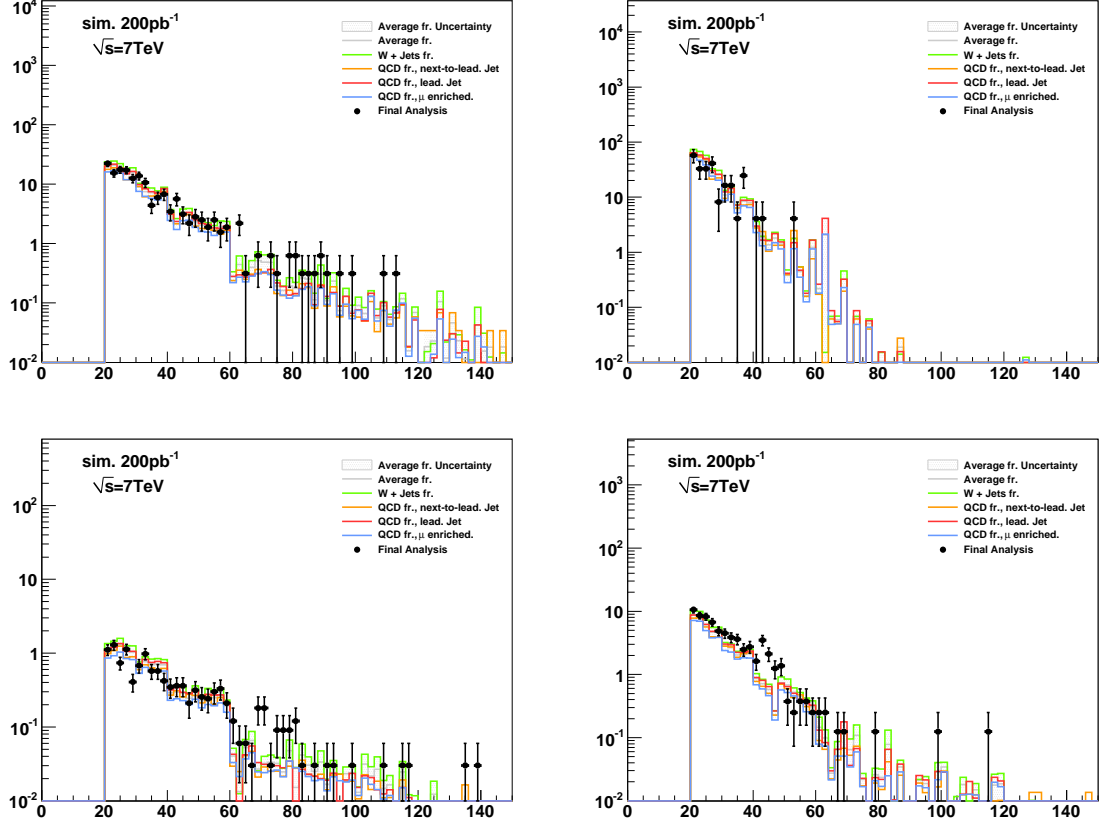


Figure 6.6: Distributions of transverse momenta of the tau-jet candidates in $W + \text{jets}$ (top left), QCD (top right), $t\bar{t} + \text{jets}$ (bottom left) and $Z \rightarrow \mu^+\mu^-$ (bottom right) background events which pass all selection criteria of the $Z \rightarrow \tau^+\tau^- \rightarrow \mu + \tau$ -jet cross-section analysis compared to the estimate obtained from the fake-rate technique, computed according to equation 6.5. The expected contribution of background processes is indicated by points. Lines of different colors represent the estimates obtained by applying fake-rate weights determined for different compositions of light quark, heavy quark and gluon jets, as described in section 6.2.1. The maximum (minimum) estimate is interpreted as upper (lower) bound. The difference between the bounds is taken as systematic uncertainty on the estimate obtained from the “CDF-type” fake-rate method and is represented by the gray shaded area.

CDFtypeResults'tauJetPt)

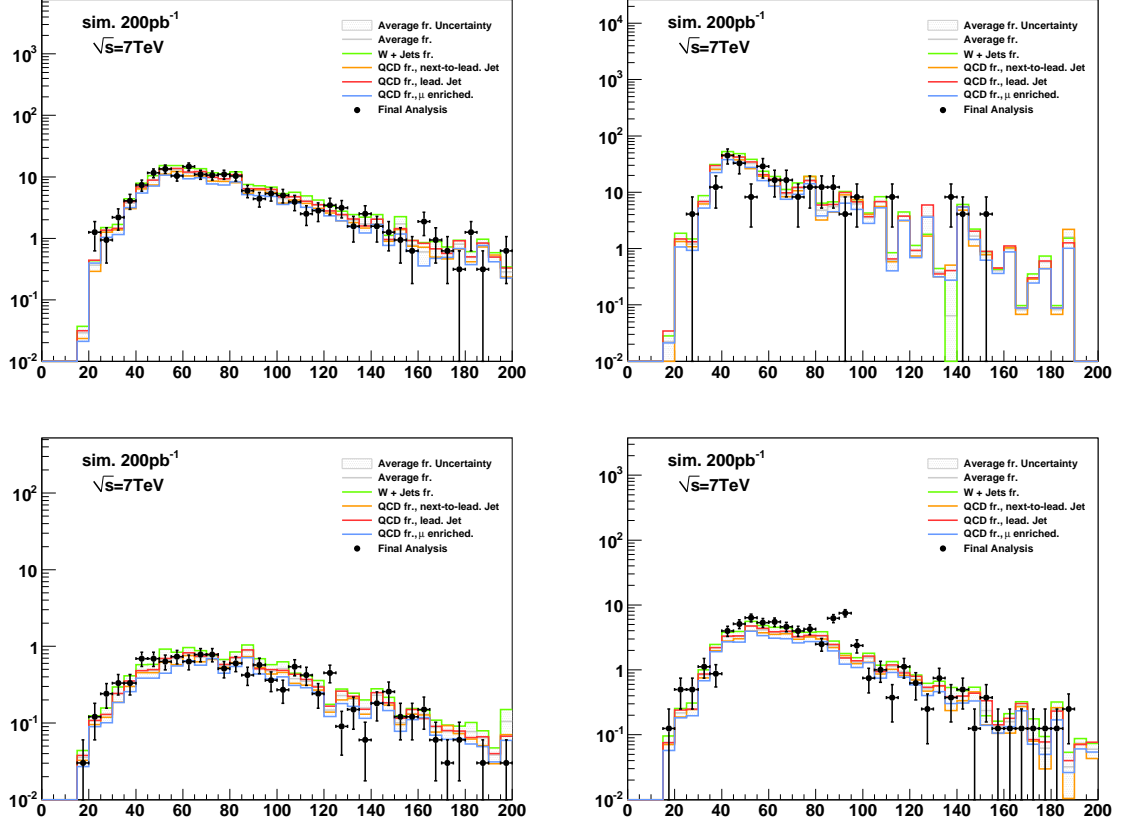


Figure 6.7: Distributions of the visible invariant mass of muon plus tau-jet in $W + \text{jets}$ (top left), QCD (top right), $t\bar{t} + \text{jets}$ (bottom left) and $Z \rightarrow \mu^+\mu^-$ (bottom right) background events which pass all selection criteria of the closure test analysis compared to the estimate obtained from the fake-rate technique, computed according to Equation 6.10.

The expected contribution of background processes is indicated by points. Lines of different colors represent the estimates obtained by applying fake-rate weights determined for different compositions of light quark, heavy quark and gluon jets, as described in Section 6.2.1. The maximum (minimum) estimate is interpreted as upper (lower) bound. The difference between the bounds is taken as systematic uncertainty on the estimate obtained from the “CDF-type” fake-rate method and is represented by the gray shaded area.

CDFtypeResults'mVisible)

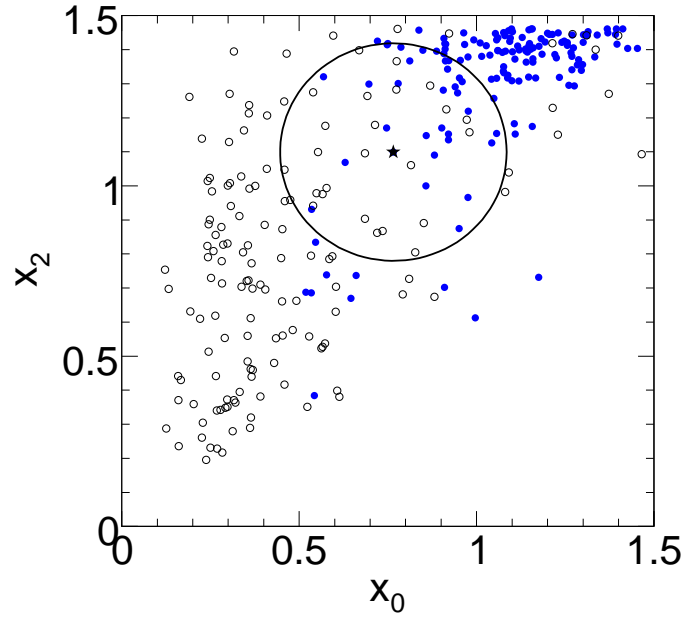


Figure 6.8: Example of the operation of a k NN classifier. The closest $k = 50$ neighbors (those inside the circle) to a test point (indicated by the star marker) are selected. The probability that the star marker is a signal event is given the number of signal neighbors (blue markers) in the circle divided by k . Image credit: [28]

(fig:KNN)

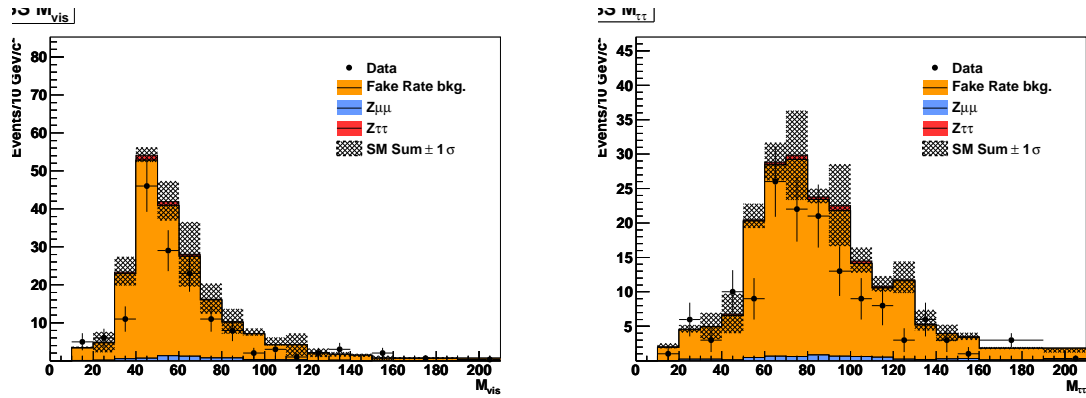


Figure 6.9: Distribution of visible mass (left) and “full” invariant mass reconstructed by the SVfit algorithm (right) observed in the like-sign charge control region compared to the background estimate obtained by the fake-rate method.

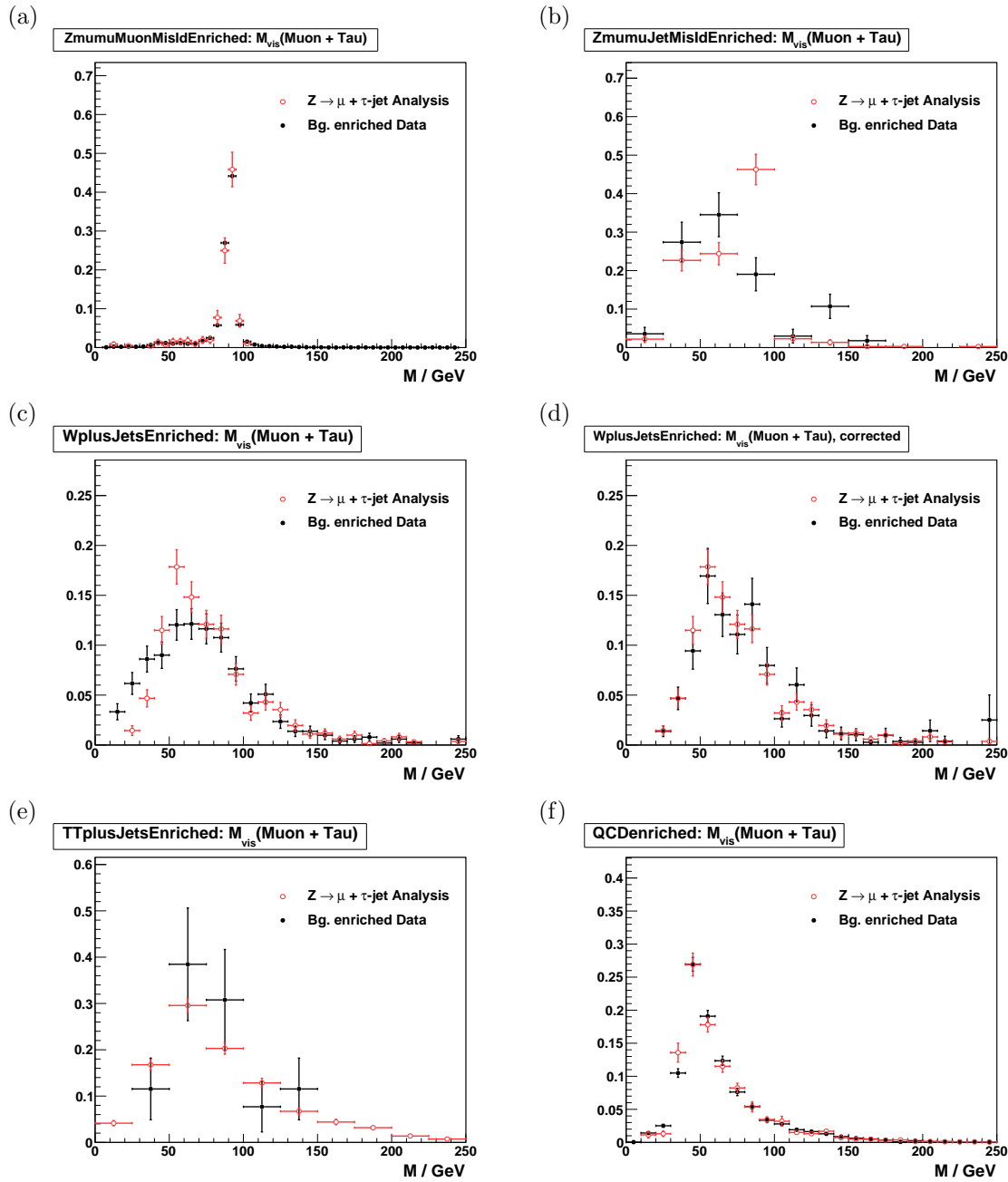


Figure 6.10: $\mu + \tau_{had}$ shape templates obtained from $Z \rightarrow \mu^+\mu^-$ (a) and (b), $W + \text{jets}$ before (c) and after (d) the bias correction explained in Section 6.3, $t\bar{t} + \text{jets}$ (e) and QCD multi-jet (f) backgrounds enriched control regions compared to the expected distribution of the enriched background process to the signal region, predicted by Monte Carlo simulations. In (a) reconstructed tau-jet candidates are expected to be dominantly due to misidentified muons, while in (b) they are expected to be mostly due to misidentified quark or gluon jets.

(fig:VisMassTemplates)

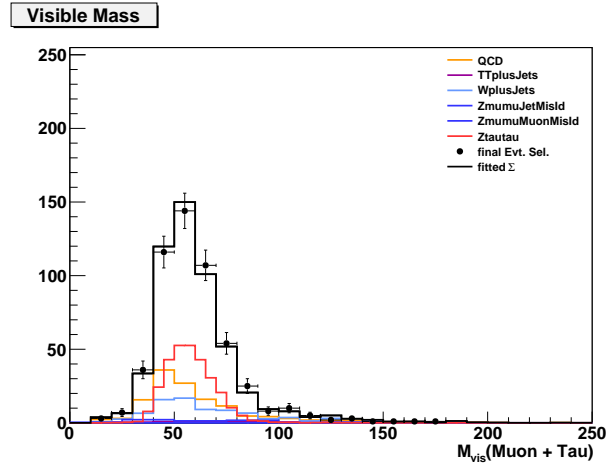


Figure 6.11: M_{vis} distribution of events selected by the $Z/\gamma^* \rightarrow \tau^+\tau^- \rightarrow \mu + \tau_{had}$ cross-section analysis compared to the sum of shape templates for signal and background processes scaled by the normalization factors determined by the fit.

g:TemplateFitControlPlot}

Chapter 7

Monte Carlo Corrections

One of the most important goals of the analysis is to minimize the effect of potentially incorrect simulation effects on the final result. While the simulated CMS events have been observed to match the 2010 data with surprising results, it is nonetheless critical to measure in real data phenomenon which can have significant effects on the analysis whenever possible. In practice, these measurements are used to apply a correction factor to the corresponding measurement obtained from Monte Carlo. This measured correction factor has an associated uncertainty, and is taken into account as a systematic uncertainty. The application of systematic uncertainties is described in the next chapter.

The corrections measured and used in this analysis can be divided into two categories, efficiency corrections and scale corrections. Identification efficiency corrections scale the expected yield (due to a given identification selection) up or down. Scale corrections systematically scale the energy of a particle (or E_T^{miss}) up or down. In this analysis we apply efficiency corrections for the High Level Trigger muon requirement, all stages of muon identification, and the hadronic tau identification. We apply a momentum scale correction to the muon and tau legs, and to the resolution of the E_T^{miss} . Finally, events are simulated with overlapping “pile-up”¹ events. The simulated events are weighted such that the number of pile-up events in the simulation matches that observed in the data.

§7.1 Muon Identification Efficiency

The identification efficiencies associated with the muon are measured in $Z \rightarrow \mu^+ \mu^-$ events using the “tag and probe” technique [43]. $Z \rightarrow \mu^+ \mu^-$ events are selected from the Muon

¹A pile-up event occurs when there are multiple interactions in one bunch proton bunch crossing. Pile-up increases with the instantaneous luminosity provided by the collider.

7 TeV CMS 2010 datasets² by requiring that the events pass the “loose” Vector Boson Task Force (VBTF) event selections [43]. In the selected events, we define the “tag” muons as those that have transverse momentum greater than 15 GeV/ c and pass the VBTF muon selection. The tag muons are further required to pass the “combined relative isolation” described in the VBTF paper. We finally require that the tag muon be matched to an HLT object corresponding to the run-dependent requirements listed in table 5.3. The trigger match requirement ensures that the event would be recorded independently of the probe muon. After the tag and probe muon pairs have been collected, we compare the muon identification performance in the probe collection in events selected in data to the performance in simulated $Z \rightarrow \mu^+\mu^-$ events. The selection of events and tag muon in the simulated sample is the same as the data sample, with the notable exception that the only HLT requirement applied in MC is that the tag muon is matched to an HLT_Mu9 object. Any difference in efficiency between the HLT_Mu9 path and the paths used to select the data (in the tag-probe measurement and in the analysis) will be considered implicitly in the correction faction.

The efficiencies for the muon selections applied in this analysis are measured using the “probe” objects. We measure the following marginal efficiencies, each relative to the previous requirement:

- Efficiency of global probe muons to satisfy VBTF muon identification selections.
- Efficiency of global probe muons passing the VBTF muon identification selection to satisfy the isolation criteria described in Section 5.1.1.
- Efficiency of probe muons passing the offline analysis selection defined in Chapter 5 to pass the HLT selection.

In each case, the invariant mass spectrum of the tag-probe pair is fitted with a Crystal Ball function for the signal ($Z \rightarrow \mu^+\mu^-$) events and an exponential for the background. The fit is done for two cases; where the probe fails the selection and the where it passes. The method is illustrated in Figure 7.1. The signal yield N is extracted from each fit and

²/Mu/Run2010A-Sep17ReReco2/RECO and /Mu/Run2010B-PromptReco-v2/RECO

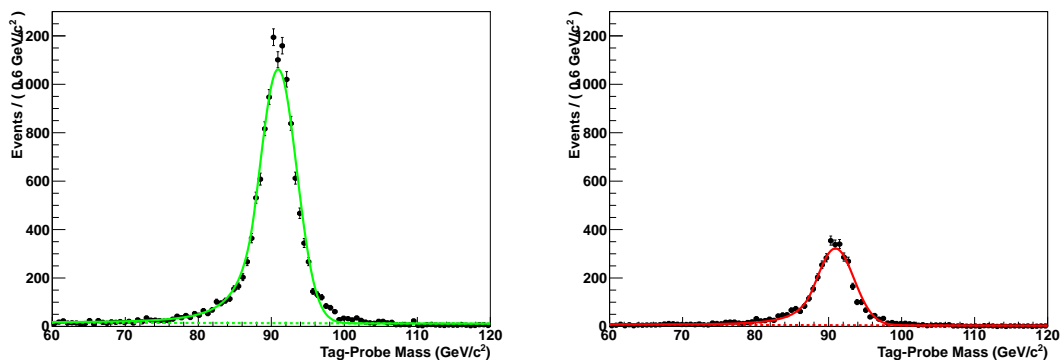


Figure 7.1: The tag-probe dimuon invariant mass spectrum in events in which the probe muon passed (left) and failed (right) the muon isolation requirement. The solid gives the result of the simultaneous fit of the signal (real $Z \rightarrow \mu^+\mu^-$ events) and background. The fitted background contribution is shown as the dotted line. The muon isolation efficiency is then extracted from the number of signal events in the passing and failing bins.

(fig:TagAndProbeFits)

1843 the efficiency is computed as $N_{pass}/(N_{pass} + N_{fail})$. Each efficiency is measured in both the
 1844 data and the simulation. The results of the measurements are shown in table 7.1. In the
 1845 final analysis, the simulated events are weighted by the fractional difference to the measured
 1846 values; the statistical uncertainty on the weight is taken as the sum in quadrature of the
 1847 statistical uncertainties for the data and simulation efficiency measurements. The uncer-
 1848 tainty on this measurement is taken as systematic uncertainty in the final measurement.
 1849

1850 The correction for the trigger efficiency needs to take into account the differences in
 1851 the HLT selections applied during different operating periods (see table 5.3). To determine
 1852 the overall correction factor, we measure the trigger efficiency in data for each of the op-
 1853 erating periods and compare it to the simulated efficiency of the HLT_Mu9 selection. The
 1854 overall efficiency in data is taken as the average of the three periods, weighted by integrated
 1855 luminosity.

1856 The efficiency of the “cross-triggers” used in the run-range period 148822 – 149182
 1857 (period C) cannot be measured in $Z \rightarrow \mu^+\mu^-$ events as they require a reconstructed PFTau
 1858 object at the trigger level. A single muon trigger (HLT_Mu15) is also used in period C.
 1859 The contribution of the cross-triggers is taken as a correction to the single muon trigger
 1860 period C efficiency. The “muon leg” of the cross-triggers have the same requirements as

Muon selection	Efficiency		Ratio	Corection
	Data	Simulation		
VBTF identification	$99.2^{+0.1}_{-0.1}\%$	$99.1^{+0.1}_{-0.1}\%$	$1.001^{+0.001}_{-0.001}$	1.0
Particle Isolation	$76.8^{+0.4}_{-0.4}\%$	$78.3^{+0.3}_{-0.3}\%$	$0.981^{+0.006}_{-0.006}$	0.98
Trigger	$95.0^{+0.5}_{-0.5}\%$	$96.5^{+0.1}_{-0.2}\%$	$0.984^{+0.006}_{-0.006}$	0.98

Table 7.1: Efficiency of the various global muon selections applied in the analysis measured in data and simulated $Z \rightarrow \mu^+\mu^-$ events. The “correction” column gives the event weight correction applied to the simulated events in the final analysis. The efficiency for each selection is the marginal efficiency with respect to the selection in the row above it.

the single muon triggers used in the run-range 147196 – 148058 (period B). The “cross-trigger” contribution is estimated as the difference between the efficiency in period B and the single-muon period C efficiency multiplied by a correction factor of $0.9 \pm 10\%$ to account for the τ leg efficiency. In the case that the measured single-muon period C efficiency is larger than the period B efficiency (due to statistical fluctuations and improvements in the trigger system), the period B efficiency is increased by 2%.

§7.2 Hadronic Tau Identification Efficiency

The hadronic tau identification efficiency has been measured in 2010 7 TeV CMS data. The most straight forward to measure the tau ID efficiency would be to use a resonance which decays to taus and has a known cross section. One could then measure the tau ID efficiency in by comparing the observed yield N_{obs} in data with that expected from the known cross section, according to the cross section equation,

$$\epsilon = \frac{N_{\text{obs}} - N_{\text{bkg}}}{\mathcal{L} \times \mathcal{A} \times \sigma \times \text{BR}_\tau}.$$

The only suitable resonance for this method is $Z \rightarrow \tau^+\tau^-$. This method has been applied³ in CMS $Z \rightarrow \tau^+\tau^-$ cross section analysis ??, and measured a tau identification simulation to data correction factor of 0.960 ± 0.067 .

³Actually, a slightly more complicated method is used. The analysis uses three decay channels, and the $Z \rightarrow \tau^+\tau^-$ cross section and tau identification correction factors are fitted simultaneously. The central value of the $Z \rightarrow \tau^+\tau^-$ cross section is driven by the $Z \rightarrow \tau^+\tau^- \rightarrow e\mu$ channel, which is independent of the hadronic tau identification.

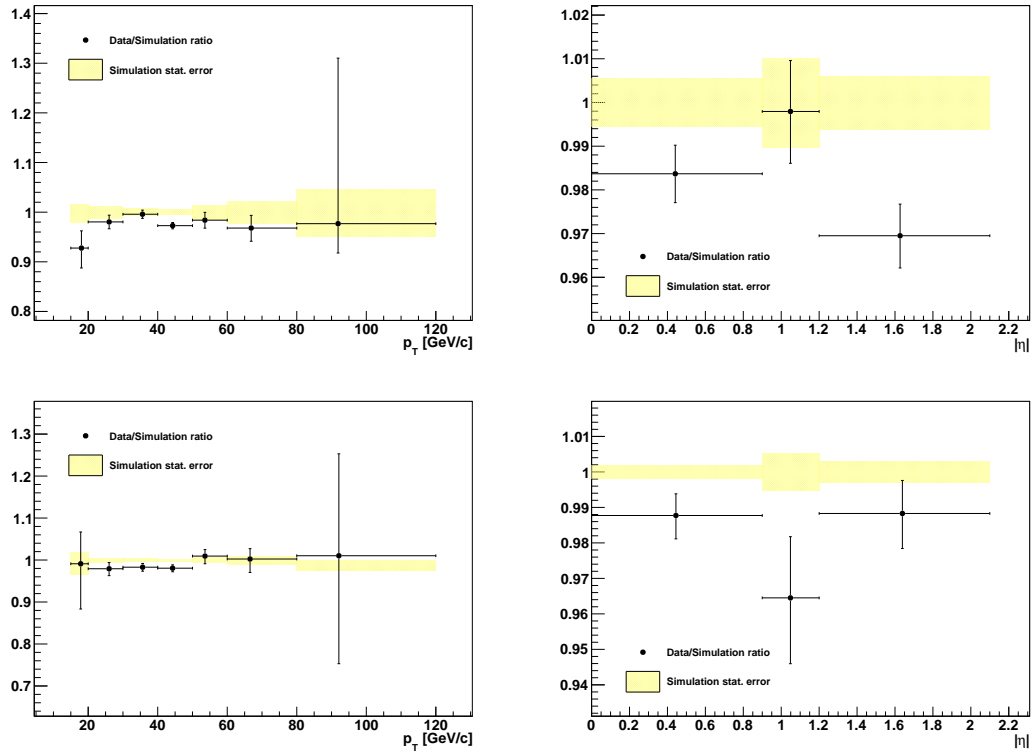


Figure 7.2: Ratio of muon isolation efficiency measured in data compared to simulated $Z \rightarrow \mu^+ \mu^-$ events.

g:MuonIsoCorrVersusPt)?

Unfortunately, this method cannot be used in this analysis. The measurement using the Z resonance operates on the assumption there is no New Physics contribution to the events in the Z bump. In the case that there was a Higgs signal at $m_{A^0} = 90 \text{ GeV}/c^2$, it would be indistinguishable from the Z and would appear as an increase of N_H in the observed yield. The analysis would then be completely insensitive to a Higgs boson on the Z peak, and cause the efficiency to be overestimated by a factor

$$\delta\varepsilon = \frac{N_H}{\mathcal{L} \times \mathcal{A} \times \sigma \times \text{BR}_\tau}.$$

1871 The solution to this problem is to use a “tag and probe” approach analogous to the
 1872 muon efficiency measurement of Section 7.1. The tag and probe method is only sensitive to
 1873 the shapes of the distributions, and will be independent of a Higgs contribution to the Z
 1874 peak. This measurement has been performed by the CMS Tau Physics Object Group [46]. A
 1875 loose hadronic tau preselection is applied to events which pass the selections (excluding the
 1876 hadronic tau identification) of the CMS EWK $Z \rightarrow \tau^+ \tau^-$ cross section measurement [51].

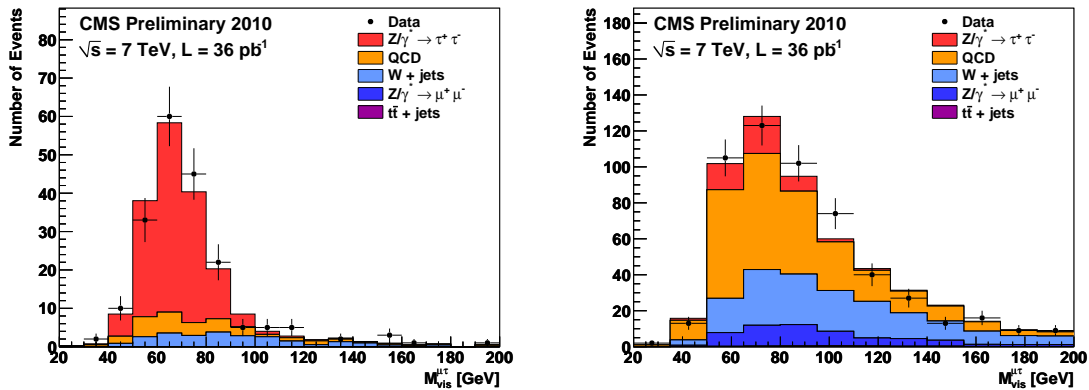


Figure 7.3: Visible mass spectrum of preselected events used to measure the hadronic tau identification efficiency in 2010 CMS 7 TeV data. The figure on the left (right) shows the preselected events that pass (fail) the hadronic tau identification. The different colors indicate the fitted yields of the different signal and background contributions. Reference: [46].

(fig:TauIdEffFits)

1877 The preselected sample is then split into to categories, those that pass the hadronic tau
 1878 identification and those that fail. The signal and background yields in the each category
 1879 are fitted using the Template Method described in Section 6.3. An illustrative example of
 1880 the fits for the yields is shown in Figure 7.3. The hadronic tau identification efficiency can
 1881 then be computed using the relative size of the true tau yields in the passing and failing
 1882 categories. The efficiency is measured [46] for the loose HPS + TaNC tau identification in
 1883 the 2010 CMS dataset and is found to be 1.06 ± 0.30 .

1884 §7.3 Muon and Tau Momentum Scale

(MuonTauMomentumScale)

1885 Muons are one of the best measured objects at CMS. The momentum scale of CMS muons
 1886 has been measured [52] using the J/ψ , $\psi(2S)$ and Υ di-muon resonant decays. The muon
 1887 momentum resolution is found to be 3% or better for muons with $p_T < 100$ GeV/c. We
 1888 apply the muon momentum correction using the “MusCleFit” algorithm described in [52].
 1889 The muon momentum correction and correction and uncertainty varies as a function of
 1890 muon p_T and η . The effect of the muon momentum correction uncertainty is a small effect
 1891 in this analysis compared to the τ and E_T^{miss} scale uncertainties.

1892 The uncertainty on the jet energy scale is determined from an analysis of the p_T bal-
 1893 ance between photons and jets in $\gamma + \text{jets}$ events [53]. The jet energy scale uncertainties

determined by the JetMET group are applied to tau-jets as well as other jets in the event. The tau energy scale correction factor is currently taken to be 1.0 with an uncertainty of 3%. The QCD jet energy scale has been measured to within 3% uncertainty. In the future, the energy scale of the tau is expected to be determined to a much better precision, as the neutral hadronic activity of a hadronic tau decay is expected to be zero. The jet energy scale of 3% can be confidently considered [46]⁴ an upper limit, and is used in this analysis as the tau energy scale uncertainty.

§7.4 Missing Transverse Energy Correction

(sec:ZRecoilCorr) In practice, the resolution of the reconstructed missing transverse energy is poor as it is sensitive to the mis-measurement of any object in the event. Furthermore, a fraction of the particles produced in the hard collision can be produced in the very forward region, outside of the fiducial region of the calorimeters. The resolution of the E_T^{miss} reconstruction can be measured in $Z \rightarrow \mu^+\mu^-$ events. The true E_T^{miss} in such events is expected to be zero. The E_T^{miss} resolution in simulated $Z \rightarrow \mu^+\mu^-$ events is found to be smaller (better) than in the data.

The E_T^{miss} resolution depends on the “recoil” of the Z boson. The reason for this effect is that for events where the Z is produced nearly at rest, the associated recoil products have very small transverse momentum and are produced at very high pseudorapidity. The E_T^{miss} is corrected using a procedure called a “Z-recoil” correction, as described in [54]. The resolution of the E_T^{miss} is measured in $Z \rightarrow \mu^+\mu^-$ events in simulation and data. The difference in the reconstructed E_T^{miss} resolution in both samples is parameterized by the magnitude of the transverse momenta of the particles recoiling against the Z .⁵ The reconstructed E_T^{miss} in the simulated $Z \rightarrow \tau^+\tau^-$, $Z \rightarrow \mu^+\mu^-$, and $W + \text{jets}$ samples is “smeared” by a random amount in each event such that the final resolution matches the observed resolution in the data.

⁴The tau energy scale was roughly measured using the invariant mass of the hadronic decay products and shown to be compatible with 1.0, within 3%.

⁵The “recoil” particles are defined as all those not identified as Z decay products. This definition is equivalent to the total decay product transverse momentum q_T added reconstructed E_T^{miss} .

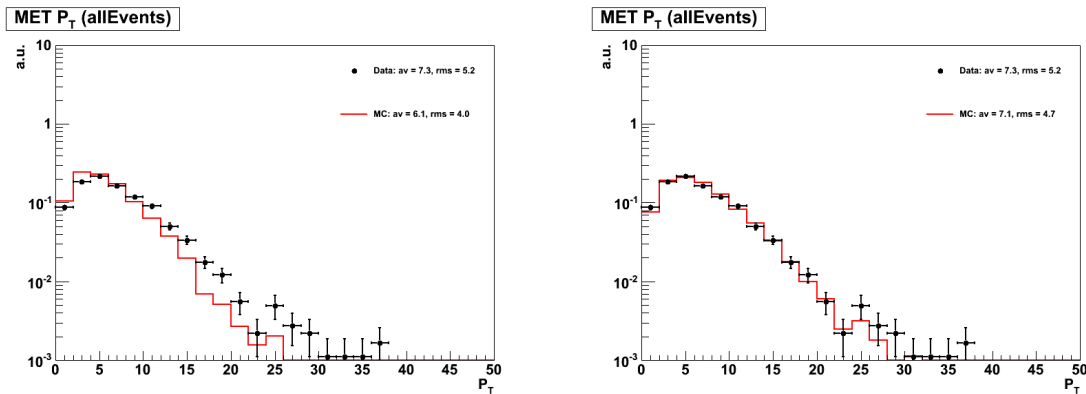


Figure 7.4: Missing transverse energy reconstructed in $Z \rightarrow \mu^+\mu^-$ events selected in data compared to $Z \rightarrow \mu^+\mu^-$ events in Monte Carlo simulation before (left) and after (right) the Z -recoil corrections to the E_T^{miss} resolution are applied.

(fig:ZrecoilCorrection)

Z -recoil corrections are determined as described in [54] and applied to simulated $Z \rightarrow \tau^+\tau^-$, $Z \rightarrow \mu^+\mu^-$ and $W + \text{jets}$ events, in order to correct for residual differences in E_T^{miss} response and resolution between data and Monte Carlo simulation [55]. The corrections are obtained by an unbinned maximum likelihood fit (in data and simulation) of the transverse recoil vector $\vec{u}_T = -(\vec{q}_T + E_T^{\text{miss}})$ as function of the transverse momentum \vec{q}_T of the Z -boson in directions parallel and perpendicular to the Z -boson transverse momentum vector. The effect of the Z -recoil correction is illustrated in Figure 7.4. The uncertainty on the Z -recoil correction factor from the maximum likelihood fit is treated as a systematic uncertainty in the final result.

§7.5 Pile-up Event Weighting

The average number of pile-up interactions in the event can effect almost all aspects of the analysis. In general, increasing pile-up lowers particle identification efficiencies and lowers E_T^{miss} resolution. It is therefore important that the distribution of pile-up events in the simulation matches the distribution found in the data. Differences in the number of pile-up interactions between the data (averaged over the analyzed run-range) and pile-up Monte Carlo samples produced for “BX156⁶” pile-up conditions are corrected for by reweighting Monte Carlo simulated events according to the number of reconstructed event

⁶The BX156 name comes from the fact that the pile-up scenario used in this simulation corresponds to an LHC configuration with 156 bunches.

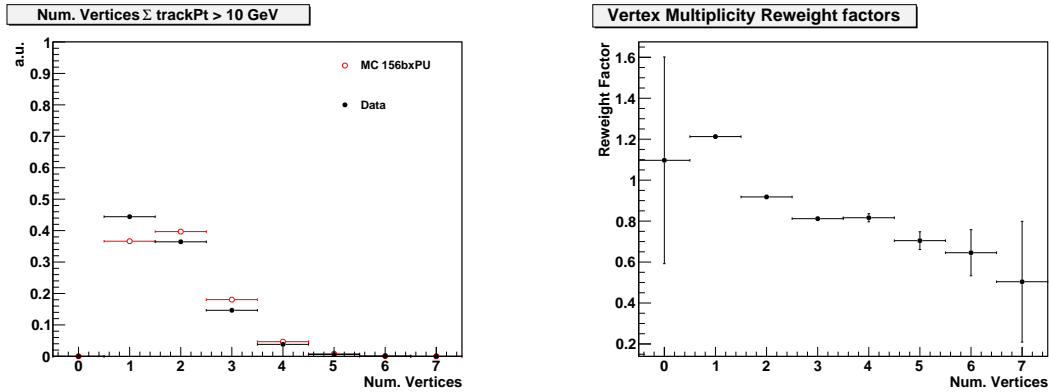


Figure 7.5: Vertex multiplicity distribution measured in the analyzed data-taking period compared to Monte Carlo simulation with “BX156” pile-up conditions (left) and resulting Monte Carlo reweighting factors (right).

(fig:pileUpReweighting)

1936 vertices, in order to match the distribution measured in a $W \rightarrow \mu\nu$ dataset triggered by
 1937 the HLT_Mu15 High Level Trigger path. Vertices considered for this purpose are required
 1938 to pass $-24 < z_{vtx} < +24$ cm, $|\rho| < 2$ cm, $n\text{DoF} > 4$. In addition, the total transverse
 1939 momenta of all tracks fitted to the vertex is required to exceed 10 GeV/c, assuming that
 1940 “softer” vertices have little or no effect on the “hard” event to pass event selection criteria.
 1941 The average vertex multiplicity distribution measured in data is compared to Monte Carlo
 1942 simulation with “BX156” pile-up conditions in Figure 7.5. Both distributions are similar,
 1943 resulting in Monte Carlo reweighting factors close to unity.

Chapter 8

Systematics and Limit Extraction

(ch:systematics)

In this chapter we discuss the systematic uncertainties affecting the search for the Higgs boson and the statistical techniques used to establish an upper limit on the Higgs $\rightarrow \tau^+\tau^-$ branching ratio times cross section ($\sigma \times \text{BR}_\tau$). The limit can be interpreted as the largest¹ signal presence that could exist in the data and still be consistent with the null hypothesis. The limit on $\sigma \times \text{BR}_\tau$ is roughly independent of the theoretical model². In the conclusion, we will interpret the $\sigma \times \text{BR}_\tau$ limit result in the context of the MSSM theory.

Proper determination of systematic uncertainties is one of the most challenging and important components in performing the measurement correctly. A systematic uncertainty is the effect of the uncertainty of some ancillary measurement (or assumption) that is used in the computation of the final result. An instructive example of how a systematic uncertainty can affect the final result is a counting experiment measuring the cross section of some signal particle in the presence of background. The formula for the cross section times the branching fraction is

$$\sigma \times BR = \frac{N_{sig}}{\mathcal{L} \cdot \mathcal{A} \cdot \epsilon} = \frac{N_{obs} - N_{bkg}}{\mathcal{L} \cdot \mathcal{A} \cdot \epsilon}, \quad (8.1) \quad \text{eq:CrossSectionE}$$

where N_{obs} is the number of events observed in data, N_{bkg} is the estimated number of background events in the observed data sample, \mathcal{L} is the integrated luminosity, and $\mathcal{A} \cdot \epsilon$ is the acceptance times efficiency of the signal. All of the quantities in Equation 8.1 (with the exception of the observed count N_{obs}) have some uncertainty which will effect the final measurement. Consider a situation where the expected number of background events is determined by fitting some sideband spectrum, and the fitted result has some error δN_{bkg} .

¹At some stated level of statistical confidence; the convention for limits in experimental high energy physics is 95%.

²Provided that the width of the Higgs bosons in the given model is smaller than the resolution of the SVfit mass resolution.

The total relative effect of this error can be obtained by error propagation

$$\frac{\delta(\sigma \times BR)}{\sigma \times BR} = \frac{\partial(\sigma \times BR)}{\partial N_{bkg}} \frac{1}{\sigma \times BR} \delta N_{bkg} = \frac{-\delta N_{bkg}}{N_{obs} - N_{bkg}}. \quad (8.2) \quad \boxed{\text{eq:CrossSectionE}}$$

1952 It is interesting to examine Equation 8.2 in two scenarios. In the limit that N_{obs} is large
 1953 compared to N_{bkg} , the effect of the error on the background estimate δN_{bkg} does not affect
 1954 the final result. In contrast, in a scenario when the data is dominated by background events,
 1955 the relative error on the signal measurement due to the background estimation approaches
 1956 infinity. The sensitivity of a measurement to a systematic uncertainty on a parameter de-
 1957 pends on the context in which that parameter is used.

1958 Experimental systematic uncertainties relevant for MSSM Higgs $\rightarrow \tau^+\tau^-$ signal extrac-
 1959 tion presented in this thesis are classified in three categories: normalization uncertainties
 1960 on the signal, normalization uncertainties on background contributions, and shape uncer-
 1961 tainties. Normalization uncertainties on the signal are due to lepton reconstruction, iden-
 1962 tification, isolation and trigger efficiencies. These terms are equivalent to the efficiency ϵ
 1963 and acceptance terms \mathcal{A} of Equation 8.2 and affect the expected yield of MSSM Higgs
 1964 $\rightarrow \tau^+\tau^-$ signal and of $Z \rightarrow \tau^+\tau^-$ background events. The uncertainties on these effects
 1965 are obtained by measuring the effect in data and simulation, according to the procedures
 1966 of Chapter 7, and calculating a correction factor. The uncertainty on this correction factor
 1967 is the systematic uncertainty. The normalization uncertainties do not affect the *shapes* of
 1968 visible and “full” invariant mass distributions which are used to extract the MSSM Higgs
 1969 $\rightarrow \tau^+\tau^-$ signal contribution in the analyzed dataset. Uncertainties on the shapes of the dis-
 1970 tributions are described by “morphing” systematics. These are due to uncertainties on
 1971 the momentum/energy scale of identified electrons, muons, tau and other jets in the event.
 1972 As the SVfit mass reconstruction algorithm uses the missing transverse energy, the shape
 1973 of the SVfit distribution is sensitive to systematic uncertainties on the overall scale E_T^{miss}
 1974 measurement. The “morphing” systematics affect the shapes of signal as well as background
 1975 contributions. Normalization uncertainties on background contributions are estimated from
 1976 the level of agreement between data and Monte Carlo simulation in background dominated
 1977 control regions.

§8.1 Signal normalization uncertainties

The signal normalization uncertainties are due to imperfect knowledge of how improperly modeled effects in the detector affect our “acceptance” model, or the probability that a given signal event will pass one of the selections (detailed in Chapter 5). The general procedure to quantify these uncertainties is to measure the effect in some control region in both the data and Monte Carlo. The ratio of data to Monte Carlo then gives a correction factor which is applied to the simulation. An uncertainty on the measurement of the effect in control region (in data, simulation, or both) is then taken as the systematic uncertainties. The signal normalization uncertainties affecting this analysis on muon trigger, reconstruction, identification and isolation efficiencies are taken from the tag and probe analysis of $Z \rightarrow \mu^+\mu^-$ events presented in Section 7.1. The uncertainty on the tau reconstruction and identification efficiency is taken to be 23%. The tau identification uncertainty measurement is discussed briefly in 7.2. The dependency of the Higgs signal extraction on the tau identification efficiency has been studied, the result being that uncertainties on the tau identification efficiency affect the limit on cross-section times branching ratio for MSSM Higgs $\rightarrow \tau^+\tau^-$ production by a few percent only. An uncertainty of 11% is attributed to the luminosity measurement.

§8.2 Background normalization uncertainties

Uncertainties on the normalization of background processes are obtained from the study of background enriched control regions presented in Chapter 6. The main non- $Z \rightarrow \tau^+\tau^-$ background to the analysis is due to QCD multi-jet and $W + \text{jets}$ events. These backgrounds are produced copiously enough for the backgrounds to be studied in control regions dominated by a single background process with a purity exceeding 90% and an event statistics exceeding the expected contribution of that background to the analysis by more than one order of magnitude. Both backgrounds are found to be well modeled by the Monte Carlo simulation. An uncertainty of 10% is attributed to the contribution of QCD and $W + \text{jet}$ backgrounds to the analysis. The cross-section for $t\bar{t} + \text{jets}$ production makes it difficult to select a high purity sample of $t\bar{t} + \text{jet}$ events of high event statistics. From the study of the 19

2006 events selected in the $t\bar{t}+jets$ background enriched control sample we assume an uncertainty
 2007 on the $t\bar{t}+jets$ background contribution in the analysis of 30%. The $Z \rightarrow \mu^+\mu^-$ background
 2008 has been studied with large statistical precision in two separate control regions, dominated
 2009 by events in which the reconstructed tau-jet candidate is either due to a misidentified quark
 2010 or gluon jet or due to a misidentified muon. Good agreement between data and Monte Carlo
 2011 simulation is found in both cases. Sizeable uncertainties on the $Z \rightarrow \mu^+\mu^-$ background con-
 2012 tribution arise due to the extrapolation from the background enriched control regions to the
 2013 data sample considered in the analysis, however: the contribution of $Z \rightarrow \mu^+\mu^-$ background
 2014 events to the analysis is due to events in which one of the two muons produced in the Z
 2015 decay either escapes detection or fakes the signature of a hadronic tau decay. Both cases
 2016 may be difficult to model precisely in the Monte Carlo simulation. The non-observation of
 2017 a Z mass peak in the mu + tau visible mass distribution studied with the fake-rate method
 2018 on the other hand sets a limit on possible contributions from $Z \rightarrow \mu^+\mu^-$ background events.
 2019 Conservatively, we assume an uncertainty of 100% on both types of $Z \rightarrow \mu^+\mu^-$ background
 2020 contributions.

2021 §8.3 Shape uncertainties

2022 Shape uncertainties on the distributions of visible and “full” invariant mass reconstructed by
 2023 the SVfit algorithm are estimated by varying the electron energy and muon momentum scale,
 2024 the energy scale of tau-jets and other jets in the event and varying the missing transverse
 2025 energy in Monte Carlo simulated events. After each variation the complete event is re-
 2026 reconstructed and passed through the event selection. Shifted visible and “full” invariant
 2027 mass shapes are obtained for each variation from the events passing all event selection
 2028 criteria. The difference between shifted shapes and the “nominal” shapes obtained from
 2029 Monte Carlo simulated events with no variation of energy or momentum scale or of the
 2030 missing transverse energy applied is then taken as shape uncertainty.

2031 The systematic uncertainties on the muon and tau energy scales have been provided
 2032 by the muon and tau Physics Object Groups and are described in Section 7.3. The mod-
 2033 elling of missing transverse energy in different types of background events has been studied
 2034 in the background enriched control regions described in Chapter 6. No significant devia-

tions between data and Monte Carlo simulation have been found (*cf.* control plots in the appendix). Uncertainties due to missing transverse energy are estimated by varying parameters of Z -recoil corrections within the uncertainties obtained when fitting (see Section 7.4) the Z -recoil correction parameters in simulated $Z \rightarrow \mu^+\mu^-$ events versus $Z \rightarrow \mu^+\mu^-$ events selected in data.

§8.4 Theory uncertainties

The signal and background normalization as well as the shape uncertainties are all experimental uncertainties in nature. Additional theoretical uncertainties arise from imprecise knowledge of parton-distribution functions (PDFs) and of the exact dependency of signal cross-sections and branching ratios on $\tan\beta$ and m_A .

The uncertainties on the signal acceptance due to PDF uncertainties are estimated using tools developed by the EWK group [56]. The acceptance is computed with respect to MSSM Higgs $\rightarrow \tau^+\tau^-$ decays that have electrons of $P_T^e > 15$ GeV and $|\eta_e| < 2.1$, muons of $P_T^\mu > 15$ GeV and $|\eta_\mu| < 2.1$, jets produced in hadronic tau decays with visible $P_T^{vis} > 20$ GeV and $|\eta_{vis}| < 2.3$ on generator level, depending on the analysis channel considered. Acceptance values are computed for the central value and 44 eigenvectors of the CTEQ66 PDF set [57]. The systematic uncertainty on the signal acceptance is computed following the PDF4LHC recommendations [58, 59].

The effect of Monte Carlo normalization, shape and theory uncertainties on the signal efficiency times acceptance is summarized in table 8.1.

§8.5 Limit Extraction Method

Given the observed distribution of $m_{\tau\tau}$ we wish to test for the presence of a Higgs boson signal, taking into account all background predictions and systematic uncertainties. To do this we use a binned Poisson likelihood, in which we represent all sources of systematic uncertainty by nuisance parameters. The core of the likelihood is simply the product of the Poisson probabilities of observing n_i events in bin i :

$$\mathcal{L} = \prod_{i=1}^{N_{bin}} \frac{\mu_i^{n_i} e^{-\mu_i}}{n_i!} \quad (8.3) \quad \{?\}$$

Source	Effect
Normalization uncertainties	
Trigger	0.981 ± 0.006
Muon identification	1.001 ± 0.001
Muon isolation	0.984 ± 0.006
Tau-jet identification	1.00 ± 0.30
Shape uncertainties	
Muon momentum scale	$\ll 1\%$
Tau-jet energy scale	$1 - 4\%^1$
Jet energy scale (JES)	$< 1\%^2$
E_T^{miss} (Z -recoil correction)	1%
Theory uncertainties	
PDF	$2\%^3$

¹ decreasing with m_A

² number quoted for $gg \rightarrow A/H$ and $b\bar{b} \rightarrow A/H$ sample as a whole;
in the subsample of events with b-tagged jets the effect of the JES uncertainty is 4%

³ with small dependence on m_A

Table 8.1: Effect of normalization uncertainties on the $gg \rightarrow A/H$ and $b\bar{b} \rightarrow A/H$ signal efficiency times acceptance.

<tab:ExpUncertainties>

2061 where the expected number of events in the bin is the sum of the number of events from all
2062 sources

$$\mu_i = \sum_{j=1}^{N_{\text{source}}} \mu_{ji}. \quad (8.4) \{?\}$$

2063 number of expected events in a source, in turn, can be written

$$\mu_{ji} = L\sigma_j\epsilon_{ji} \quad (8.5) \{?\}$$

2064 where L is the integrated luminosity, σ_j is the cross section for source j , and ϵ_{ji} is the
2065 efficiency for source j in bin i .

2066 To test for the presence of the signal, we examine the likelihood is a function of our
2067 signal cross-section. If there is a significant signal, one can simply maximize the likelihood as
2068 a function of the cross-section and use the usual methods to determine confidence intervals.
2069 If there is not a significant signal, we can set upper bounds on the signal cross-section using

2070 one of several methods, as discussed below.

2071 There are two types of systematic errors considered in this analysis, and represented
 2072 in the likelihood by Gaussian constrained nuisance parameters. In the first case, we modify
 2073 our description of the number of events in a given bin from a given source to include a mul-
 2074 tiplicative parameter which represents the uncertainty in the cross-section for that source.
 2075 Nominally, such parameter is unity, but is allowed to float in the likelihood, constrained to
 2076 within its uncertainty. This method allows one to naturally take into account correlations
 2077 between different sources, or the different channels combined together in the analysis. Thus
 2078 one might have

$$\mu_i = \beta_1 L \sigma_1 \epsilon_{1i} + \beta_1 \beta_2 L \sigma_1 \epsilon_{2i} \quad (8.6) \{?\}$$

2079 where we have introduced two nuisance parameters, β_1 and β_2 , where β_1 affects both sources
 2080 but β_2 only affects the second source.

2081 The second type of nuisance parameter is used to represent systematic errors which
 2082 affect the shape (and possibly also the normalization) of the mass distribution. We refer to
 2083 these as “morphing parameters” and we use that technique known as “vertical morphing”
 2084 in which we create templates (histograms of the efficiencies) after having shifted the value
 2085 of some parameters such as an energy scale by an amount corresponding to a believe is
 2086 one standard deviation of uncertainty in that scale. This technique allows one to calculate
 2087 the new shape of the mass distribution as a continuous function of the morphing param-
 2088 eter, which is Gaussian constrained to zero within its uncertainty. We generate templates
 2089 corresponding to a -1 standard deviation shift, the nominal template, and a +1 standard
 2090 deviation shift. To get the number of predicted events in a bin, we interpolate quadratically
 2091 between these three points, and extrapolate linearly beyond them.

2092 The overall likelihood then, including nuisance parameters, can be written

$$\mathcal{L}(\sigma_{Higgs}) = \prod_{i=1}^{N_{bin}} \frac{\mu_i^{n_i} e^{-\mu_i}}{n_i!} \times \prod_{m=1}^{N_\beta} \mathcal{G}(\beta_m). \quad (8.7) \{?\}$$

2093 where here we have made it explicit that the likelihood is a function of the signal cross-
 2094 section. To eliminate the nuisance parameters, we use MINUIT to maximize this likelihood
 2095 with respect to them. This is known as a profile likelihood technique.

2096 In the absence of the signal, for even in the presence of one, we can determine a upper

Higgs State	Included when		
	$m_{A^0} < 130 \text{ GeV}/c^2$	$m_{A^0} = 130 \text{ GeV}/c^2$	$m_{A^0} > 130 \text{ GeV}/c^2$
A^0	yes	yes	yes
H^0	yes	yes	no
h^0	no	yes	yes

Table 8.2: Logic for determining the MSSM Higgs cross section for a given mass of the CP-odd A^0 Higgs. In some regions of parameter space, the contributions of one of the CP-even Higgs particles is ignored.

2097 95% CL bound on the cross-section of the signal using the profile likelihood. In one method
 2098 we simply use Bayes' Theorem to convert the likelihood to a posterior density in the signal
 2099 cross-section, and integrate to find the point below which 95% of the probability lies. Though
 2100 this is not strictly Bayesian, we have shown that in complicated fits like this one the results
 2101 of the profile likelihood are identical to marginalizing the nuisance parameters.

2102 In the other method, we find that point where the logarithm of the profile likelihood is
 2103 1.92 units below the value of the likelihood at zero signal cross-section. This gives similar
 2104 limits to the previous method, which tend to be more stringent when there is a negative
 2105 fluctuation or no fluctuation in the apparent signal, but less stringent than the Bayesian
 2106 limits when there is an upward fluctuation giving an apparent signal. The complete exami-
 2107 nation of the coverage properties of these two methods is beyond the scope of this note. We
 2108 report the results of both prescriptions below.

2109 In order to combine the ggA and qqA production modes, what we call our signal cross-
 2110 section is the sum of the cross-section times branching ratio for both modes, assuming
 2111 $\tan\beta = 30$. Additionally, as discussed in Section 1.2.3, the MSSM Higgs sector consists of
 2112 two Higgs doublets, yielding five physical Higgs bosons. This search is sensitive to the three
 2113 neutral Higgs particles the h^0 , H^0 , and A^0 . The relative contributions of the three Higgs
 2114 types depends on the mass m_{A^0} of the CP-odd Higgs. For $m_{A^0} \leq 130 \text{ GeV}/c^2$, the A^0 and
 2115 h^0 are approximately degenerate in mass and width. In this region the H^0 has a very small
 2116 relative cross section and a constant mass of $m_{H^0} \approx 130 \text{ GeV}/c^2$. For $m_{A^0} \geq 130 \text{ GeV}/c^2$, the
 2117 h_0 reaches a limiting mass of $\approx 130 \text{ GeV}/c^2$, and the H^0 and A^0 become mass degenerate.

Source	Method	Magnitude
Tau ID/trigger	Multiplicative	20%
Z cross section	Multiplicative	5%
Jet to τ fake rate	Multiplicative	20%
$\mu \rightarrow \tau$ fake rate	Multiplicative	100%
W +jets cross section	Multiplicative	10%
$t\bar{t}$ cross section	Multiplicative	40%
integrated luminosity	Multiplicative	10%
Tau energy scale	Morphing	2%
Missing E_T scale	Morphing	XX%
Muon p_T scale	-	neg.
EM energy scale	-	neg.

Table 8.3: Summary of systematic uncertainties represented by nuisance parameters in the likelihood, their representation method and magnitudes.

<tab-sys>

2118 In the results presented below we use nuisance parameters corresponding to the sys-
2119 tematic errors summarized in table 8.3.

2120

Chapter 9

2121

Results

⟨ch:results⟩

FiXme:

Get cite

Process	Events without b -tag	Events with b -tag
$t\bar{t}$ + jets	0.6	2.26
W + jets	62.9	0.51
$Z \rightarrow \mu^+\mu^-$	3.8	0.04
QCD	124.0	5.07
$(qq)Z \rightarrow \tau^+\tau^-$	234.2	3.46
Standard Model sum	425.5	11.34
Data	398	15

Table 9.1: Number of Higgs $\rightarrow \tau^+\tau^- \rightarrow \mu + \tau_{had}$ candidate events passing the selection criteria described in Chapter 5.

resultsLooseAHtoMuTau)?

Process	Events without b -tag	Events with b -tag
Gluon fusion production		
A90	37.21	0.86
A100	27.40	0.40
A120	14.39	0.14
A130	11.81	0.18
A160	4.46	0.09
A200	1.51	0.03
A250	0.47	0.01
A300	0.15	0.0
A350	0.06	0.44
Associated b -quark production		
bbA90	33.07	5.50
bbA100	30.18	4.77
bbA120	21.91	4.02
bbA130	18.34	3.35
bbA160	10.35	2.10
bbA200	4.85	1.29
bbA250	2.11	0.55
bbA300	0.97	0.26
bbA350	0.41	0.13

Table 9.2: Number of Higgs signal event expected to pass the selection criteria described in Section 5. The expected signal yield is given for MSSM parameter $\tan \beta = 30$, using the cross sections provided by the LHC Higgs Cross Section working group.

resultsLooseAHtoMuTau)?

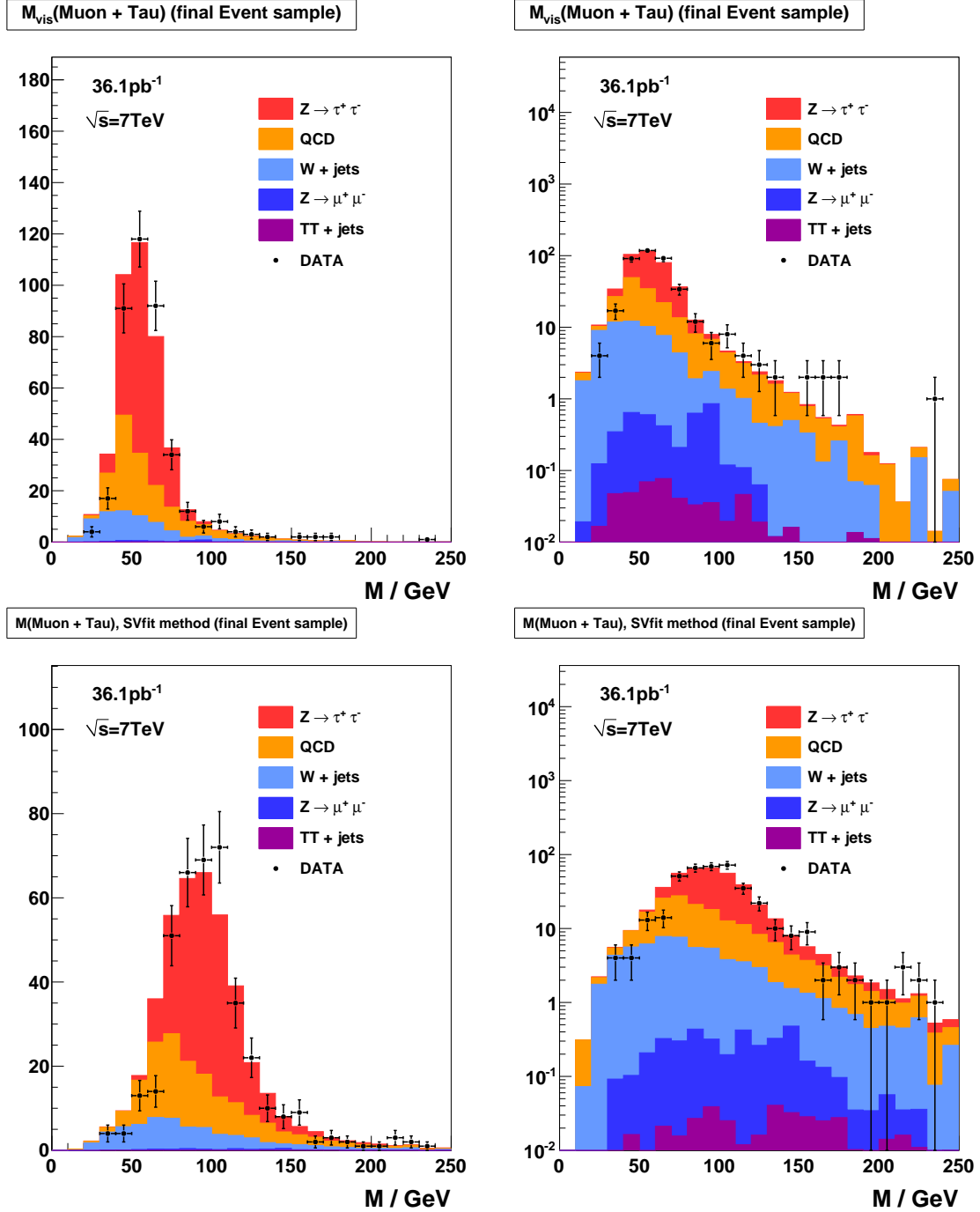


Figure 9.1: Distribution of visible (top) and "full" $\tau^+\tau^-$ invariant mass reconstructed by the SVfit algorithm (bottom) in Higgs $\rightarrow \tau^+\tau^- \rightarrow \mu + \tau_{had}$ candidate events passing the selection criteria described in Chapter 5. The distributions are shown in linear (logarithmic) scale on the left (right).

:AHtoMuTauPlotsLoose)?

2122

Chapter 10

2123

Conclusions

?<ch:conclusions>?

Bibliography

- [1] J. Goldstone, “Field Theories with Superconductor Solutions”, *Nuovo Cim.* **19** (1961) 154–164. doi:10.1007/BF02812722.
- [2] J. Goldstone, A. Salam, and S. Weinberg, “Broken Symmetries”, *Phys. Rev.* **127** (Aug, 1962) 965–970. doi:10.1103/PhysRev.127.965.
- [3] F. Englert and R. Brout, “Broken Symmetry and the Mass of Gauge Vector Mesons”, *Phys. Rev. Lett.* **13** (Aug, 1964) 321–323. doi:10.1103/PhysRevLett.13.321.
- [4] P. W. Higgs, “Broken Symmetries and the Masses of Gauge Bosons”, *Phys. Rev. Lett.* **13** (Oct, 1964) 508–509. doi:10.1103/PhysRevLett.13.508.
- [5] G. S. Guralnik, C. R. Hagen, and T. W. B. Kibble, “Global Conservation Laws and Massless Particles”, *Phys. Rev. Lett.* **13** (Nov, 1964) 585–587. doi:10.1103/PhysRevLett.13.585.
- [6] S. Glashow, “Partial Symmetries of Weak Interactions”, *Nucl.Phys.* **22** (1961) 579–588. doi:10.1016/0029-5582(61)90469-2.
- [7] S. Weinberg, “A Model of Leptons”, *Phys.Rev.Lett.* **19** (1967) 1264–1266. doi:10.1103/PhysRevLett.19.1264.
- [8] A. Salam, “Weak and Electromagnetic Interactions”,. Originally printed in *Svartholm: Elementary Particle Theory, Proceedings Of The Nobel Symposium Held 1968 At Lerum, Sweden*, Stockholm 1968, 367-377.
- [9] D. Griffiths, “Introduction to Elementary Particles”. Wiley-VCH, 2004.
- [10] S. M. T. Morii, C.S. Lim, “The Physics of the Standard Model and Beyond”. World Scientific, 2004.
- [11] UA1 Collaboration, “Experimental observation of isolated large transverse energy electrons with associated missing energy at $\sqrt{s} = 540 \text{ GeV}$ ”, *Phys. Lett.* **B122** (1983) 103–116.
- [12] UA2 Collaboration, “Observation of single isolated electrons of high transverse momentum in events with missing transverse energy at the CERN $\bar{p}p$ collider”, *Phys. Lett.* **B122** (1983) 476–485. doi:10.1016/0370-2693(83)91605-2.
- [13] UA1 Collaboration, “Experimental observation of lepton pairs of invariant mass around $95 \text{ GeV}/c^2$ at the CERN SPS collider”, *Phys. Lett.* **B126** (1983) 398–410. doi:10.1016/0370-2693(83)90188-0.

- [14] UA2ZDiscovery [2157] UA2 Collaboration, “Evidence for $Z^0 \rightarrow e^+e^-$ at the CERN $\bar{p}p$ collider”, *Phys. Lett. B* **129** (1983) 130–140. doi:10.1016/0370-2693(83)90744-X.
- [15] Martin:1997am [2159, 2160, 2161, 2162] S. P. Martin, “A Supersymmetry Primer”, *arXiv hep-ph* (sep, 1997). 128 pages. Version 5 (December 2008) contains a change in convention that flips the signs of sigma and sigmabar matrices. It also contains a total of about 2 pages of updates, mostly on supersymmetry breaking issues. Errata and a version with larger type (12 pt, 142 pages) can be found at <http://zippy.physics.niu.edu/primer.html>.
- [16] FeynmanDiagrams [2163] CERN Computing Newsletter.
- [17] Rainwater:1998kj [2165, 2166] D. L. Rainwater, D. Zeppenfeld, and K. Hagiwara, “Searching for $H \rightarrow \tau^+\tau^-$ in weak boson fusion at the LHC”, *Phys. Rev. D* **59** (1999) 014037, arXiv:hep-ph/9808468. doi:10.1103/PhysRevD.59.014037.
- [18] PDG [2168] Particle Data Group Collaboration, “Review of particle physics”, *J. Phys. G* **37** (2010) 075021. doi:10.1088/0954-3899/37/7A/075021.
- [19] MSTWXSectionPlots [2169]
- [20] LHCiggsXSecGroup [2171] LHC Higgs Cross Section Working Group Collaboration, “Handbook of LHC Higgs Cross Sections: 1. Inclusive Observables”, arXiv:1101.0593.
- [21] MHMaxBenchmark [2173, 2174, 2175] M. Carena, S. Heinemeyer, C. Wagner et al., “MSSM Higgs boson searches at the Tevatron and the LHC: Impact of different benchmark scenarios”, *The European Physical Journal C - Particles and Fields* **45** (2006) 797–814. 10.1140/epjc/s2005-02470-y.
- [22] CMSEExperiment [2177] CMS Collaboration, “The CMS experiment at the CERN LHC”, *JINST* **3** (2008) S08004.
- [23] CMS-PAS-TRK-10-004 [2179, 2180] CMS Collaboration, “Measurement of Momentum Scale and Resolution using Low-mass Resonances and Cosmic-Ray Muons”, *CMS PAS CMS-PAS-TRK-10-004* (2010).
- [24] CMS-PAS-TRK-10-005 [2182] CMS Collaboration, “Tracking and Primary Vertex Results in First 7 TeV Collisions”, *CMS PAS CMS-PAS-TRK-10-005* (2010).
- [25] CMS-PTDR [2184] G. L. Bayatian et al., “CMS Physics Technical Design Report Volume I: Detector Performance and Software”. Technical Design Report CMS. CERN, Geneva, 2006.
- [26] CMS-PAS-PFT-08-001 [2186] CMS Collaboration, “CMS Strategies for tau reconstruction and identification using particle-flow techniques”, *CMS PAS CMS-PAS-PFT-08-001* (2008).
- [27] CMS-PAS-PFT-09-001 [2188] CMS Collaboration, “Particle-Flow Event Reconstruction in CMS and Performance for Jets, Taus, and MET”, *CMS PAS CMS-PAS-PFT-09-001* (2009).
- [28] TMVA [2190, 2191, 2192] A. Hoecker, P. Speckmayer, J. Stelzer et al., “TMVA - Toolkit for Multivariate Data Analysis”, *arXiv physics.data-an* (mar, 2007). Published in: PoSACAT:040,2007 TMVA-v4 Users Guide: 135 pages, 19 figures, numerous code examples and references.

- [29] A. Kolmogorov, “On the representation of continuous functions of several variables by superposition of continuous functions of one variable and addition”, *Doklady Akademiia Nauk SSSR* **114** (1957).
2194
2195
- [30] J. C. *et al.*, “Size of signal cones and isolation rings in the CMS tau identification algorithm”, *CMS Note* **2008/026** (2008).
2197
- [31] M. Bachtis, S. Dasu, and A. Savin, “Prospects for measurement of $\sigma(pp \rightarrow Z) \cdot B(Z \rightarrow \tau^+\tau^-)$ with CMS in pp Collisions at $\sqrt{s} = 7$ TeV”, *CMS Note* **2010/082** (2010).
2199
2200
- [32] CMS Collaboration, “Study of tau reconstruction algorithms using pp collisions data collected at $\sqrt{s} = 7$ TeV”, *CMS PAS* **CMS-PAS-PFT-10-004** (2010).
2202
- [33] G. P. S. M. Cacciari and G. Soyez, “The anti-kt jet clustering algorithm”, *JHEP* **04** (2008) 063, arXiv:0802.1189.
2204
- [34] CMS Collaboration, “Commissioning of the Particle-Flow reconstruction in Minimum-Bias and Jet Events from pp Collisions at 7 TeV”, *CMS PAS* **PFT-10-002** (2010).
2206
2207
- [35] S. M. T. Sjöstrand and P. Skands, “PYTHIA 6.4 Physics and Manual”, 2000.
2208
- [36] S. Jadach, Z. Was, R. Decker et al., “The Tau Decay Library Tauola: Version 2.4”, *Comput. Phys. Commun.* **76** (1993) 361.
2210
- [37] S. Agostinelli, J. Allison, K. Amako et al., “G4—a simulation toolkit”, *Nuclear Instruments and Methods in Physics Research Section A: Accelerators, Spectrometers, Detectors and Associated Equipment* **506** (2003), no. 3, 250 – 303. doi:10.1016/S0168-9002(03)01368-8.
2212
2213
2214
- [38] J. Conway, E. Friis, M. Squires et al., “The Tau Neural Classifier algorithm: tau identification and decay mode reconstruction using neural networks”, *CMS Note* **2010/099** (2010).
2216
2217
- [39] CDF Collaboration, “Search for MSSM Higgs decaying to τ pairs in $p\bar{p}$ collision at $\sqrt{s} = 1.96$ TeV at CDF”, *Phys. Rev. Lett.* **96** (2006).
2219
- [40] CMS Collaboration, “CMS technical design report, volume II: Physics performance”, *J. Phys.* **G34** (2007) 995–1579. doi:10.1088/0954-3899/34/6/S01.
2221
- [41] L. Bianchini, “Improved Collinear Approximation for VBF $H \rightarrow \tau\tau \rightarrow 3\nu + \ell + \tau_{had}$ ”, *CMS Note* **2010/226** (2010).
2223
- [42] B. K. Bullock, K. Hagiwara, and A. D. Martin, “Tau Polarization And Its Correlations As A Probe Of New Physics”, *Nucl. Phys.* **B 395** (1993) 499.
2225
- [43] CMS Collaboration, “Measurements of Inclusive W and Z Cross Sections in pp Collisions at $\sqrt{s} = 7$ TeV”, *CMS PAS* **EWK-10-002** (2010).
2227
- [44] CMS Collaboration, “MET Performance in Events Containing Electroweak Bosons from pp Collisions at $\sqrt{s} = 7$ TeV”, *CMS PAS* **JME-10-005** (2010).
2229

- [45] L. Lusito and C. Veelken, “Estimation of Background contributions to Tau analyses via Template Fitting”, *CMS Note* **2010/088** (2010).
 2231
- [46] CMS Collaboration, “Performance of tau reconstruction algorithms in 2010 data collected with CMS”, *CMS PAS TAU-11-001* (2011).
 2233
- [47] D. Jang, “Search for MSSM Higgs decaying to τ pairs in $p\bar{p}$ collision at $\sqrt{s} = 1.96$ TeV at CDF”, *Ph.D. Thesis, Rutgers University* (2006).
 2235
- [48] C. C. Almenar, “Search for the neutral MSSM Higgs bosons in the $\tau\tau$ decay channels at CDF Run II”, *Ph.D. Thesis, Universitat de Valencia* (2008).
 2237
- [49] J. Conway, E. Friis, and C. Veelken, “Measurement of the $Z/\gamma^* \rightarrow \tau^+\tau^-$ Production Cross-section in the $\mu + \tau_{had}$ final state using the HPS+TaNC Tau id. algorithm”, *CMS Note* **2011/021** (2011).
 2239
 2240
- [50] T. Früboes and M. Zeise, “The TauAnalysis/MCEmbeddingTools Package”.
<https://twiki.cern.ch/twiki/bin/view/CMS/SWGuideTauAnalysisMCEmbeddingTools>
 2242
- [51] CMS Collaboration, “Measurement of the Inclusive $Z \rightarrow \tau\tau$ Cross Section in pp Collisions at $\sqrt{s} = 7$ TeV”, *to be published* (2011).
 2244
- [52] S. Bolognesi, M. A. Borgia, R. Castello et al., “Calibration of track momentum using dimuon resonances in CMS”, *CMS Note* **2010/059** (2010).
 2246
- [53] CMS Collaboration, “Jet Energy Corrections determination at $\sqrt{s} = 7$ TeV”, *CMS PAS JME-10-010* (2010).
 2248
- [54] G. Bauer et al., “Modeling of $W \rightarrow \ell\nu$ MET with Boson Recoil”, *CMS Note* **2010/332** (2010).
 2250
- [55] G. Cerati et al., “Search for MSSM neutral Higgs $\rightarrow \tau^+\tau^-$ Production using the TaNC Tau id. algorithm”, *CMS Note* **2010/460** (2010).
 2252
- [56] J. Alcaraz. <https://twiki.cern.ch/twiki/bin/view/CMS/SWGuideEWKUtilities>.
 2253
- [57] P. M. Nadolsky et al., “Implications of CTEQ global analysis for collider observables”, *Phys. Rev. D* **78** (2008) 013004, arXiv:0802.0007.
 2255
- [58] PDF4LHC Working Group. <http://www.hep.ucl.ac.uk/pdf4lh/PDF4LHCrecom.pdf>.
 2256
- [59] R. C. G. D. Bourilkov and M. R. Whalley, “LHAPDF: PDF use from the Tevatron to the LHC”, arXiv:0605.0240.
 2258